SHAPE MEMORY TECHNOLOGY: WORKING MECHANISMS, MODELING AND SURFACE PATTERNING APPLICATION

ZHAO YONG

School of Mechanical and Aerospace Engineering

A dissertation submitted to the Nanyang Technological University
in fulfillment of the requirement for the degree of
Doctor of Philosophy

2013

Abstract

A new way to classify shape memory materials (SMMs) was proposed based on the underlying working mechanisms behind the shape memory effect (SME). Three categories, namely dual-state mechanism, dual-component mechanism, and partial-transition mechanism, were discussed in details. Based on this, the concept of advanced shape memory technology was proposed to enable the SME in materials, to design/synthesize new SMMs with tailored features, and to optimize the SME in materials. Previously, SME is considered as a unique behavior in some certain materials. In this study, based on ASMT, SME can be achieved in a range of materials, which are not the traditional SMMs.

A generic 3-D model was developed to simulate the shape memory behavior in polymeric SMMs. This model was verified by a series of experiments. In addition, this model was applied for optimization of the SME. The thermo-/chemo-responsive SME in poly(methyl methacrylate) (PMMA) were systematically studied by experiments and simulation.

Based on above study on the fundamentals, different surface patterning methods were developed to fabricate micro/nano-sized surface features, including well-controllable wrinkled patterns, PMMA microlens arrays, reversible surface patterns and 3-D surface patterns.

Keywords: shape memory materials; shape memory effect; advanced shape memory technology; thermo-/chemo-responsive; 3-D finite element modeling; surface patterning.

Acknowledgements

Foremost I would like to express my warmest and deepest gratitude to my supervisor, Dr. Huang WeiMin, for his guidance, keen insights, encouragements and friendship. His keen insights and wide visions gave me a great help for understanding my project and gaining research skills. Working with him has been an invaluable and honorable experience during my graduate education.

I want to express my very heartfelt gratitude to Dr. Wang Changchun, Dr. Ding Zhen, Mr. Hendra Purnawali, Mr. Tang Cheng, and Mr. Zhang Jiliang for their kind helps and beneficial discussion.

I am also grateful to the technicians in Centre for Mechanics of Micro-Systems and Materials, Materials Laboratory, Strength of Materials Laboratory and Metrology Laboratory for their assistance and kindness in various aspects.

I want to thank my parents, wife and sister for their constant and intense love. Their unconditional support on every enterprise that I have undertaken in my life has given me the confidence to get to where I am today. A life time would not be enough to express my gratitude to them.

Finally, I thank NTU for giving me a chance to study with a research scholarship.

Table of Contents

List of Figures

List of Tables

Chapter 1 Introduction

1.1 Background

Driven by the needs from engineering applications, new materials are kept on being developed for enhanced performance and/or new functions. Among them, there is a group of materials which are able to recover their original shape at the presence of the right stimulus, such as heat (thermo-responsive), light (photo-responsive), chemical (including water, chemo-responsive) [1-7]. Technically speaking, these materials are known as shape memory materials (SMMs). This phenomenon is called the shape memory effect (SME), which provides an alternative approach for many designs that are difficult to achieve using conventional materials/technologies.

In many occasions in the literature, the SME is discussed together with another shape change phenomenon, i.e., shape change effect (SCE). Different from the SME, in which a material is able to virtually keep the quasi-plastic deformation forever, the SCE refers to a kind of elastic or superelastic behavior in response to the right stimulus [7, 8]. For instance, electro-active polymers and polarized piezoelectrical materials (such as lead zirconate titanate) are able to alter their shape spontaneously when an electrical voltage is applied and return to the original shape instantly upon removal of the voltage. Furthermore, the amount of displacement is about in proportional to the magnitude of the applied voltage [9, 10]. Similarly, we may claim that the elastic deformation in materials is essentially a kind of SCE.

Fundamentally from energy point of view, the difference between SCE and SME is due to the magnitude of energy barrier between two states, in which one is under the right stimulus, and the other is not. As shown in Figure 1.1, if the energy barrier between shape *A* and shape *B* is almost zero, upon removal of the applied stimulus, the material is able to return to its original position (the SCE). If the energy barrier is very high (*H*), without additional driving force to overcome the barrier, the material will maintain the deformed shape (the SME). If the barrier is low (*H'*), the material may slowly recover its original position. Viscous-elasticity is a typical example of such. Sometimes, the SME may appear in a gradual manner (typically in responding to light and chemical) due to the nature of time consuming process in accumulating enough driving energy or gradual penetration of the stimulus.

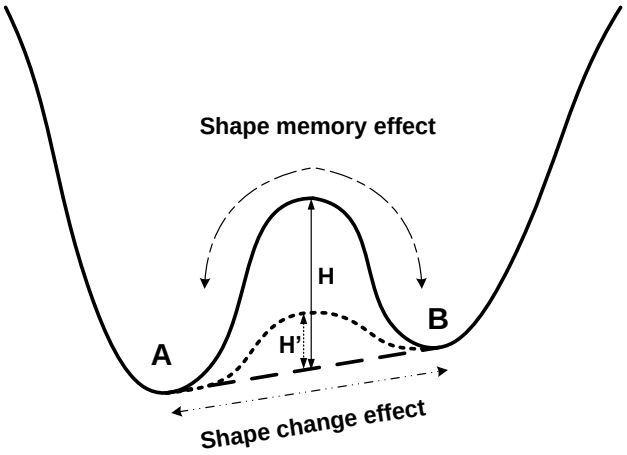

Figure 1.1 Shape memory effect (SME) and shape change effect (SCE).

Depending on the exact situation, a material may have the SME or the SCE. Hence, if we classify the exact type of material according to the composition/molecular structure, a material may belong to both SMM and shape change material (SCM). For example, at low temperatures, a shape memory alloy (SMA) has the SME (and thus, belongs to the family

of SMM); on the other hand, at high temperatures, it behaves superelastically in responding to mechanical loading, and hence is the SCE [11, 12]. Shape memory polymers (SMPs) actually share this similarity as SMAs.

Among SMMs, there is a group of polymeric materials, which have various advantages, such as high degree of recovery strain, light weight, low cost, low density, tunable mechanical property, easy processing, tailored application temperature, potential biodegradability and biocompatibility, etc [8]. In this study, we mainly focus on the SME in polymeric materials.

The expansion of the SMM family is rather rapid [6, 7, 13-21]. In addition to the continuous efforts in developing new SMMs and modifying existing ones, excellent SME has been observed in some conventional polymeric materials [22-24], bio-plastics [25-28] and even metallic materials [29].

Although not so often, here and there in the literature we have seen statement directly or indirectly mentioning that all polymeric materials should have the SME (most likely meant for the thermo-responsive SME, e.g., in a very recent publication by Mendez et al. [30]). Some early experiments conducted on some commonly used engineering polymers (e.g., in [31-44]) have indicated the shape recovery phenomenon after annealing. Nevertheless, the exact working mechanisms behind various shape memory features in response to different stimuli and programming methods (i.e., a procedure to setup the temporary shape) have yet seemingly been well established till now.

In addition to the investigation of conventional shape memory features, some advanced SME phenomena have been reported in the literature, such as triple (or multi)-SME [14,

16, 45-50], temperature memory effect (TME) [46, 49] and reversible plasticity (RP)-SME [23, 24, 44, 51-53]. Engineering applications of SMMs have been reported in a range of areas, such as in bio-medical devices [54-58], space engineering [59, 60], active assembly and disassembly [61, 62], etc.

On the other hand, some numerical models have been developed to reproduce, mainly, the thermo-responsive SME following two common approaches [63-74]. One approach is thermo-visco-elasto-plastic modeling [49, 50, 54, 82, 111], and the other is *phase* transition modeling [51, 52, 114, 115]. Early efforts were limited to one-dimensional (1-D) and small strain, which have limited applicability and are more for qualitative prediction [75]. Recently, some three-dimensional (3-D) and finite-deformation models have been proposed, but not all SME features can be reproduced quantitatively by these models.

As more and more polymeric SMMs and new shape memory phenomena are reported, some fundamental questions naturally emerge:

- What are the working mechanisms behind these SMEs?
- Whether the SME is an intrinsic feature of polymeric materials and even metallic materials?
- How to optimize these shape memory phenomena?

1.2 Objectives

This project aims to answer above mentioned questions, and thus to provide good understanding of the fundamentals behind all types of SMEs, in particular in polymeric SMMs. Based on the working mechanism, a new way to classify all SMMs is to be

proposed. According to this new classification, the concept of advanced shape memory technology (ASMT) can be proposed to address the following points:

- How to enable the SME in a range of materials?
- How to design a SMM with the required feature(s)/function(s)?
- How to optimize the SME in a SMM?

Currently, SMMs are reported in certain materials. However, based on ASMT, SME can be achieved in a range of materials, which are not the traditional SMMs.

Further to the fundamentals of the ASMT, a numerical model needs to be developed to reproduce all kinds of SMEs and in the mean time, provide a useful guide for quantitative simulation.

Utilizing the ASMT, some novel surface patterning methods can be developed.

1.3 Outline of the dissertation

Chapter 1 briefly introduces the background of this project, and presents the objectives of this study and outline of this dissertation.

Chapter 2 is a concise while comprehensive review about recent progress in polymeric SMMs, such as common features of thermo-responsive SMPs, traditional classifications of SME, recent numerical modeling progress in polymeric SMMs, and some novel applications.

In Chapter 3, a new classification method for all of SMMs is proposed based on the working mechanisms. Subsequently, we propose the concept of ASMT, to enable SME in

materials, to design/synthesize new SMMs with tailored features, and to optimize the SME. In addition, the reversible plasticity (RP)-SME and chemo-responsive SME are briefly discussed.

In Chapter 4, a generic 3-D finite element model is developed to study thermo-responsive SME in polymeric SMMs. This model is verified by experimental results. Based on this model, we can design a SMM and optimize the SME.

In Chapter 5, thermo-/chemo-responsive SME in poly(methyl methacrylate) (PMMA) is systematically studied experimentally and simulated by the model developed in Chapter 4.

In Chapter 6, a few novel thermo-/chemo-responsive surface patterning methods are developed to produce well controllable and tunable micro/nano-sized surface features.

Chapter 7 gives a brief summary of this research and future work.

Chapter 2 Literature review

This chapter presents a brief review on the current progress in stimuli-responsive shape memory materials (SMMs), including basic features and mechanisms, numerical modeling and applications. The review is mainly focused on polymeric SMMs.

Unless otherwise stated, the strain and stress in this dissertation are engineering strain and engineering stress.

2.1 Basic features and mechanisms

We take thermo-responsive SMM as a reference to introduce the basic features and mechanisms. For the thermo-responsive SME, transition temperature, T_t, is important. Most likely the exact transition for the thermo-responsive SME in polymeric SMMs is either the glass transition or melting. Corresponding, the glass transition temperature, T_g, and melting temperature, T_m, are possible T_t.

2.1.1 Basic features in thermo-responsive SME

Figure 2.1(a) demonstrates a typical programming and recovery cycle. In the programming process, in which the programming temperature is defined as T_p, shape fixity ratio, R_f, is used to character the ability of a SMM to retain the temporary shape after programming. In the recovery process, stress/strain evolves against temperature. Time might be an important parameter in viscous materials, such as many polymers. Two parameters, namely shape recovery ratio, R_r, in free recovery, and recovery stress, σ_r, in constrained recovery, are used for characterization. R_f and R_r are defined as

$$R_f = \frac{L_2 - L_0}{L_1 - L_0} \times 100\% = \frac{\varepsilon_r}{\varepsilon_m} \times 100\% \quad (2.1)$$

$$R_r = \frac{L_3 - L_2}{L_0 - L_2} \times 100\% = \left(1 - \frac{\varepsilon_f}{\varepsilon_r}\right) \times 100\% \quad (2.2)$$

where L_0, L_1, L_2, and L_3 stand for the dimension of a sample in different stages, as shown in Figure 2.1(a). ε_m is the applied maximum strain during programming. ε_r is the residual strain right after programming. ε_f is the final strain after shape recovery. Different from R_f and R_r, there is no simple expression for σ_r, as it is a function of heating temperature. Normally, the maximum stress, $\sigma_r^{\max}$, is a parameter of our interest. Besides these parameters, shape recovery occurs when a sample is heated to a critical temperature, namely shape recovery temperature, T_r. The start and finish points in shape recovery are defined as T_r^s and T_r^f, respectively.

Let us refer to Figure 2.1(b) and (c) to discuss some other important issues in the thermo-responsive SME (assumed to be T_g based) in a programming and recovery cycle. These basic issues are:

(I) Thermal expansion [63, 65, 76]

Because the coefficient of thermal expansion (CTE) of polymers is generally one or two orders of other materials (such as, metals, and ceramics), the effects of thermal expansion on shape memory behavior may be non-negligible.

(II) Visco-elastic deformation in programming at $T_p > T_g$ (dashed line in Figure 2.1b) [77-82]

This is a traditional programming process to achieve a higher R_f. A visco-elastic constitutive model is applicable to describe the strain vs. stress relationship [79, 80]. Normally cooling is followed before unloading. It is obvious that to avoid long-range chain slippage is necessary for high R_r. As such, T_p, ε_m and strain rate $\dot{\varepsilon}$ in deforming are important parameters in programming for optimized SME [83-85].

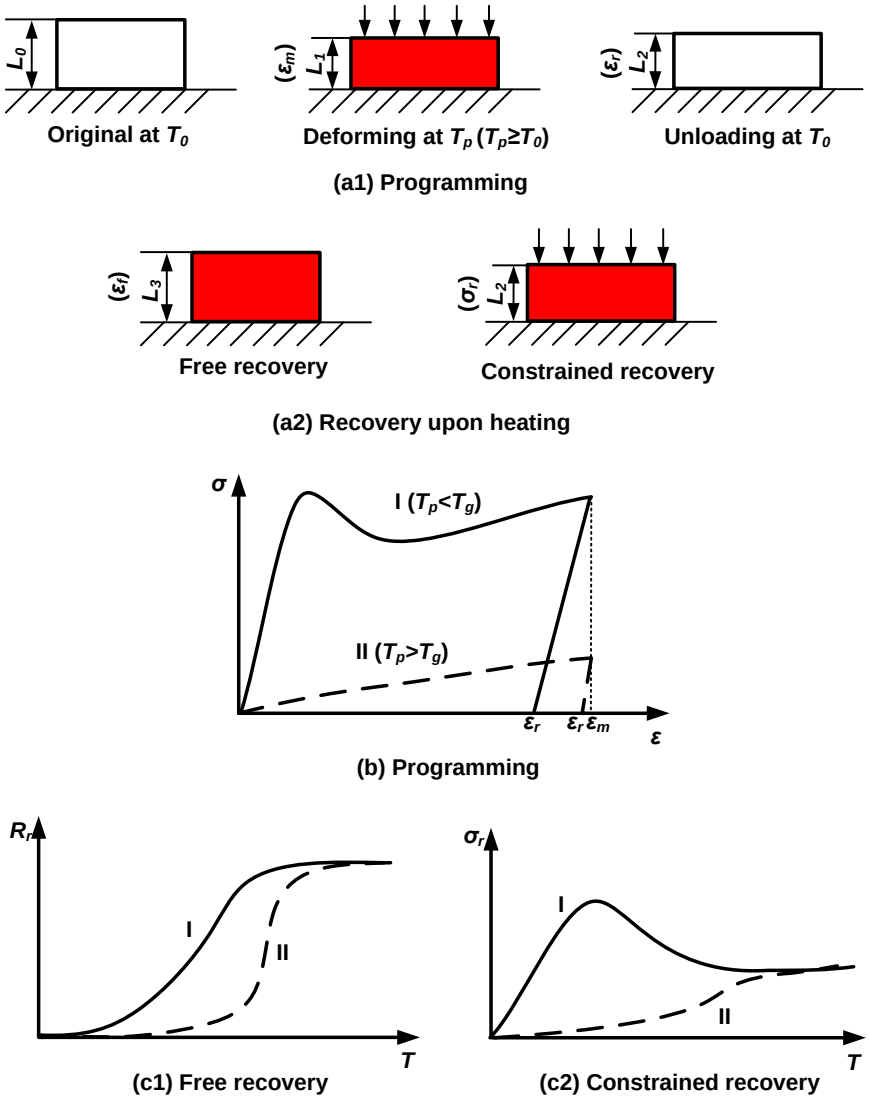

Figure 2.1 Illustration of typical programming and shape recovery procedure in a thermo-responsive SMM.

(III) Visco-elasto-plastic deformation in programming at $T_p < T_g$ (solid line in Figure 2.1b) [77, 78, 83-87]

For some polymers, it is possible to program at low temperatures ($T_p<T_g$), which is given the term of reversible plasticity (RP)-SME recently [46, 88]. The strain vs. stress relationship in polymers at $T_p < T_g$ is visco-elasto-plastic [23, 24, 44, 51-53]. The RP-SME, which requires an higher deformation stress in programming can produce an higher recovery stress [46].

(IV) Stress relaxation during cooling [64, 66, 67, 75, 89]

It has been reported that stress relaxation may remarkably affect the recoverable strain and recovery stress [64, 89]. The time of stress relaxation is related to the cooling rate and is a critical parameter in recovery. Tobushi et al. has systematically studied relationship between the irrecoverable strain and stress relaxation in a polyurethane (PU) based SMP [64]. Subsequently, it was proposed to control the strain recovery, so as to obtain a desired new shape by means of controlling the parameters in the stress relaxation process [89].

(V) Instant recovery upon unloading [46, 63, 65-67]

Upon unloading, instant recovery occurs largely due to elastic recovery. Instant recovery is important which determines the shape fixity in SMMs. To achieve high shape memory performance, a high R_f is normally required.

(VI) Free recovery after being programmed at $T_p > T_g$ (dashed line in Figure 2.1c1) [5, 41, 83, 84]

It has been observed that free recovery becomes the most dramatical at around the previous programming temperature (T_p), provided that T_p is within the transition range [6, 90, 91]. Furthermore, the actual recovery finishing temperature (T_r^f) also depends on T_p [13, 46]. Free recovery may also be evaluated by means of the recovery speed, V_r, which is defined as the temperature derivative of recovery ratio, i.e., $V_r = dR_r / dT$. V_r peak may be observed, and corresponding temperature, T_{sw}, is defined as the shape memory switching temperature [46]. It was reported that T_{sw} is related to T_p and T_g (or T_m) [46]. However, the exact relationship among them is still unclear.

(VII) Recovery in RP-SME after being programmed at $T_p < T_g$ (solid line in Figure 2.1c1) [44, 92, 93]

For amorphous glassy polymers, quasi-plastic strain forms during programming at $T_p < T_g$, and retains in the sample after unloading. Normally, there are two parts in the quasi-plastic strain. Upon heating, the recovery of one part of the quasi-plastic strain starts at lower temperatures and finishes at about T_g-20°C. This is defined as low temperature recovery (LTR) [44, 92, 93], which is proposed as a result of the decrease in the T_g at the interfaces of special shear domains formed by plastic deformation [44, 93]. The recovery of the other part of the quasi-plastic strain starts at high heating temperatures (>T_g-20°C) and usually finishes above T_g, so that it is called high temperature recovery (HTR) [44, 92, 93]. The HTR is associated with reorientation of molecular chains in polymers.

(VIII) Stress evolution in constrained recovery (Figure 2.1c2) [41, 44, 86-89]

It was found that recovery stress depends largely on the T_p [91, 94]. For a sample programmed at T_p>T_g, σ_r increases monotonically upon heating; however, for a sample

programmed at $T_p<T_g$, during heating σ_r reaches a peak value (σ_r^{max}) before decreasing. Moreover, σ_r^{max} is related to T_p [94-97]. Hence, this phenomenon may be called temperature memory effect (TME) [46, 49].

2.1.2 Mechanisms and classifications

As we know, the mechanism behind the SME in polymeric SMMs is different from that of SMAs, which is due to reversible martensitic transition between low temperature martensite and high temperature austenite [98]. In contrast, polymeric SMMs rely on the entropic phenomenon, in which the high entropy state is the stable one. Pre-deformed polymeric materials have the potential to evolve toward the stable state.

Most recent review papers tried to classify the traditional SMPs according to the fixing and triggering mechanisms with respect to, such as molecular structure, stimulus etc.

Liu et al. proposed four major SMP groups according to the molecular structure [1], namely covalently cross-linked glassy polymers (class I), covalently cross-linked semi-crystalline polymers (class II), physically cross-linked glassy polymers (class III) and physically cross-linked semi-crystalline block polymers (class IV) [1]. Xie summarized the two requirements for the SME in traditional SMPs as following: a reversible thermal transition for temporary shape fixing and recovering; a cross-linked network for stable permanent shape [46]. Most (if not all) polymeric materials meet the first requirement, while only some polymers satisfy the second requirement if without any cross-linking process.

Based on the type of stimulus, traditional SMPs are under the following categories, namely thermo-responsive SMP, chemo-responsive SMP, photo-responsive SMP etc [1, 4-7, 93, 99]. For traditional thermo-responsive SMPs, the molecular chain conformation is altered upon loading at higher temperatures ($>T_t$), which results in a lower entropy state and macroscopic shape change (temporary shape). Upon cooling to lower temperatures ($<T_t$), the temporary shape is fixed due to the freezing of motion in molecular chains. Upon reheating, the molecular mobility is activated and macroscopic shape recovery occurs [100, 101].

Direct heating is the main approach to trigger the recovery in thermo-responsive SMMs. Many alternative heating approaches, such as joule heating, irradiative heating and conductive heating, etc have been developed [102-105]. Yang et al. demonstrated water-induced shape recovery in an ether-based PU [101, 106-109]. This is so called chemo-responsive SME. The T_g of this PU is dramatically depressed by water due to the disruption in intramolecular bondings and the plasticization effect. Similar phenomenon has been reported in styrene-based SMP/dimethylformamide (DMF) and poly(vinyl alcohol) (PVA)/DMF systems [110]. Light induced shape fixity and recovery without any heat involved (i.e., photo-responsive SME) has been achieved [111, 112].

According to the number of shapes, polymeric SMMs can be classified as dual-shape (the original shape and temporary shape, which is traditional), triple-shape (one additional stable intermediate shape between temporary shape and original shape), and multi-shape (more than one intermediate shape) [16, 46, 49]. Bellin et al. reported the triple-SME in a cross-linked network with two distinct thermal transitions (i.e., two T_gs) [113, 114]. Two temporary shapes are associated with these two T_gs in a macroscopically homogenous

polymer system [113, 114]. A different approach was proposed by Xie et al. to combine two different dual-shape SMPs as a composite [115]. The multi-SME can actually be obtained based on only one transition [16, 49]. A framework has been proposed to analyze such multi-SME and TME, and to optimize the shape memory performance [49].

Indeed, from engineering application point of view, optimization of SMMs is highly in demand [16, 49]. In addition to optimization in material synthesis, programming optimization is another important practical approach for SMMs, in which numerical simulation may provide great help.

2.2 Modeling of polymeric SMMs

Intensive research on modeling of SMAs in the past years has resulted in many sophisticated constitutive models [116-119]. However, these models are not applicable to polymeric SMMs because of the fundamental difference in the underlying mechanism for the SME.

As for thermo-responsive polymeric SMMs, there are two common approaches for modeling.

One is the thermo-visco-elasto-plastic approach, which requires the relationships of temperature-dependent viscosity and/or modulus parameters [49, 50, 54, 82, 111].

The other is the *phase* transition approach, which considers polymeric SMMs as a mixture of different *phases*. Volume fractions of these individual *phases* might be temperature-dependent [51, 52, 114, 115].

2.2.1 Thermo-visco-elasto-plastic approach

Probably, the first numerical model for polymeric SMMs was proposed by Tobushi et al in 1997, which was developed for the thermo-responsive SME in PU SMP [63]. It is modified from a standard linear visco-elastic model integrated with a slip element and taking thermal expansion into account. The thermo-mechanical function for log(E) against temperature is simplified as a linear relationship, where E is the Young's modulus. This model is for 1-D small deformation study, since plastic deformation is ignored. In 2001, Tobushi et al. modified their model to include plastic deformation term [64], so that a large strain (up to 20%) can be accommodated [100].

In 2005, Morshedian et al. proposed a three-element rheological model to predict heat-shrink behavior in crosslinked low-density polyethylene (LDPE) [73]. This model considers the time-dependent relaxation behavior in polymers by means of introducing a dashpot element. It is able to simulate the stress-strain-time relationship under isothermal condition. However, this model is limited to 1-D and elastic deformation at $T_p > T_m$.

In 2007, Khonakdar et al. modified the three-element model by considering temperature-dependent behavior at a constant heating rate. This model was applied to predict temperature-dependent recovery in [120]. However, this model is still limited to 1-D and elastic deformation.

In 2006, Diani et al. developed a 3-D thermo-visco-elastic model for the thermo-mechanical behavior of SMPs. This model is formulated under a finite strain framework in order to account for large strain deformation [68]. It is based on clear physical meaning in programming in either glassy state or rubbery state. The deformation in a glassy state

polymer is dominated by the internal energy, while the deformation in a rubbery state polymer is dominated by entropy. However, this 3-D model is still only for elastic deformation.

In 2008, Nguyen et al. modified the models proposed by Diani et al. [68] and Qi et al. [66], and took into account the structural and stress relaxation by means of incorporating time-dependent structural relaxation and visco-plastic properties in the glassy state, together with plastic deformation (with a distinct yield point) [67]. Moreover, unlike previous models, which are mainly for basic SME, it can predict the TME in constrained recovery. However, the predicted behavior in free recovery only qualitatively agrees with the experimental results.

In 2010, Nguyen et al. further modified their previous model [75]. This model consists of *N* Voigt elements (in serie) and *N* Maxwell elements (in parallel). It is able to well predict free recovery in SMPs if programmed at high temperatures. Since plastic deformation in SMPs at lower temperatures ($<T_g$) is ignored, this model cannot predict RP-SME.

2.2.2 *Phase* transition approach

In 2006, Liu et al. developed a 3-D small strain constitutive model [65], which might be the first reported piece of SMP modeling work based on the *phase* transition approach. In this model, two extreme phases (namely, hard phase and soft phase) are used for the glassy state and rubbery state, respectively. This model can predict many important features in SMPs, such as temperature-dependent free recovery, temperature-dependent stress recovery, etc. However, it is only applicable to small strain cases (within 10%). Plastic deformation and associated RP-SME are not considered.

Important parameters in a *phase* transition approach are the temperature-dependent volume fractions of individual phases. Liu et al. [65] proposed a phenomenological temperature-dependent function for the volume fraction of glassy state, f_g, as

$$f_g = 1 - \frac{1}{1 + c(T_0 - T)^n} \tag{2.1}$$

where c and n are determined by curve fitting of experimental results, T_0 is a reference temperature (close to T_g), and T is the temperature of SMP.

In 2008, Qi et al. developed a 3-D constitutive model and implemented it in a finite element software, ABAQUS [66]. This model is also based on the concept of phase transitions, in which a hyper-elastic model is used for the rubbery state; and a visco-plastic model is used for the glassy state. This model well predicts the stress vs. strain relationship in programming and the temperature vs. strain relationship in free recovery. But it cannot well simulate constrained recovery.

The distinct advantage in *phase* transition approach is that it can be adapted to a wide variety of polymeric SMMs with different transition mechanisms. Taking chemo-responsive SMMs as an example, if we have the relationship between the volume fraction of soft phase and chemo-stimulus, a 3-D model can be easily developed. Recently, Long et al. developed a model for photo-responsive SMMs based on the concept of phase transition approach [121, 122]. In this model, the material is considered as a mixture of two networks, one is the original network, and the other is the photo-stimulated reformed network.

2.2.3 Comparison of models for thermo-responsive polymeric SMMs

Table 2.1 is a summary of above mentioned models. The capabilities of these models are listed for comparison. Refer to Section 2.1.1 for the features (I to VIII) in a typical shape memory cycle. Approach A and Approach B refers to thermo-visco-elasto-plastic, and *phase* transition approaches, respectively.

Approach A is focused on establishing a complicate constitutive law for the entire material. However, Approach B studies a representative unit via a *phase* transition approach. It is clear that the *phase* transition approach is more flexible for simulation of SMPs.

Table 2.1 Typical models for thermo-responsive polymeric SMMs.

Ref.	Types of model	Simulated features							
		I	II	III	IV	V	VI	VII	VIII
[63, 123]	1-D four-element rheological model (Approach A)	Yes	Yes	No	No	Yes	Yes	No	Yes
[73]	1-D three-element rheological model (Approach A)	No	Yes	No	Yes	No	Yes	No	No
[68]	3-D thermo-visco-elastic model (Approach A)	Yes	Yes	No	Yes	Yes	No	No	Yes
[124]	1-D rheological model (Approach A)	Yes	Yes	No	Yes	Yes	Yes	No	No
[67]	Thermo-visco-elastic model (Approach A)	Yes	Yes	Yes	Yes	Yes	No	No	Yes
[65]	1-D small strain constitutive model (Approach B)	Yes	Yes	No	Yes	Yes	Yes	No	Yes
[66]	3-D constitutive model (Approach B)	Yes	Yes	Yes	No	Yes	Yes	No	No

2.3 Typical applications of polymeric SMMs

Utilizing different shape memory features in various polymeric SMMs, a range of applications have been proposed in different engineering areas [6, 8, 46, 112, 121]. As a matter of fact, the application of polymeric SMMs can be traced back to well before the terminology of SMPs was coined. Early applications of the SME in polymers include heat shrinkable tube, wrap, packaging and self-adjustable utensil [4]. Recently, some new potential applications are proposed, including smart structure/device, smart surface device, smart clothing, biomedical device, and deployable space structure, etc [2, 125, 126].

In this section, only a couple of typical applications, in particular those novel ones developed recently, are presented.

2.3.1 Novel medical devices

In 2007, Dietsch et al. reported that 50% to 70% of patents related to SMPs are for medical applications [2]. Some of them are now available in the market. New Ortho Polymers, MnemoScience, MedShape and All Fit China are some examples among others [2].

Suture is a commonly used device in medical operations. However, in minimally invasive surgery, in general there is only a limited space for tying knots in order to secure suture in place. Even worse, surgeons have to tie knots remotely through small holes. SMP provides a good solution to this problem. Self-tightening SMP suture (even with biodegradable function) has attracted great attention since this concept was proposed [127-129]. Instead of using heat or light, Huang et al. reported a PU SMP suture which is able to self-tighten

upon immersing into room temperature water without any other interference. SMP wires with a diameter of 10s μm, much thinner than human hair, can be easily produced as sutures [8, 130].

Stent is another promising area for SMPs. SMP stents can be made into a solid tube shape to effectively prevent tissue in-growth. Drug eluting is easier to achieve to prevent infection [8, 130]. Figure 2.2 shows that by folding a circular shaped SMP ring into a star shape at high temperatures, it is going to be much easier to pack the stent into a catheter for later on delivery and deployment.

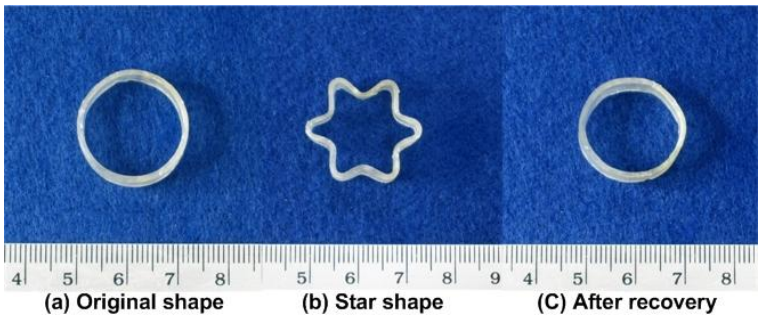

Figure 2.2 SMP stent [8].

Biodegradable polymer stents, based on, for instance, poly(vinyl alcohol) (PVA), polylactide (PLA) and poly(ethylene glycol) (PEG) etc, have been invented in recent years [131]. Many degradable SMPs have also been developed (e.g., [132, 133]). Even so, the ability of instant removal (due to any unforeseen reasons, such as migration and severe infection) in any type of polymer stents is apparently a great advantage. Retraction of SMP stents can be achieved utilizing the moisture-responsive feature or the triple-SME [134]. Note that, the latter, i.e., the triple-SME, has been proven to be an intrinsic feature of all SMPs [49].

Targeted drug release on specified cells at molecular level is an attractive topic in current medical research [135]. On the other hand, toward a miniaturized mechanical surgery [136], we need many tiny tools/machines. SMMs, in particular SMPs, could be the right material for them [137]. Figure 2.3 reveals the delivery of a PU SMP coil into a jellyfish by injection, which demonstrates the feasibility of the concept to deliver a big objective through a small hole.

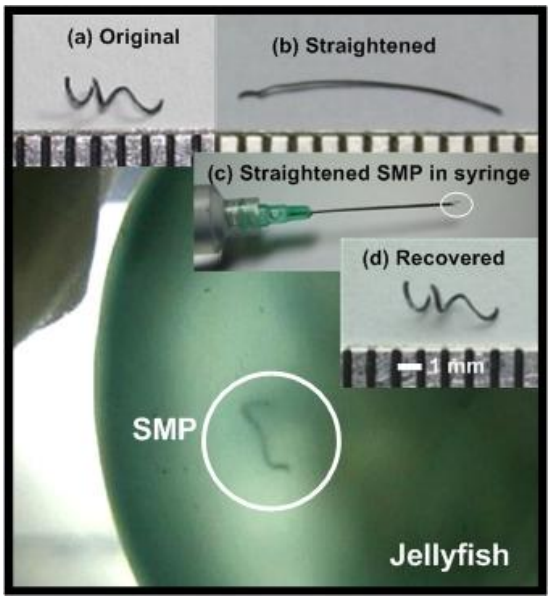

Figure 2.3 Delivery of a SMP coil into a jellyfish by injection. (a) Original coiled shape; (b) after being straightened at high temperatures; (c) ready for injection; (d) recovered shape [100].

2.3.2 Smart structures

(1) Active assembly/disassembly

Liu et al. demonstrated a self-packaging application of polymeric SMM sheet [138]. Firstly, a transparent polystyrene (PS) sheet is pre-strained; then, the pre-strained PS sheet is patterned with black ink; finally, the patterned sheet is illuminated using unfocused light.

Self-folding occurs due to shrinkage of the inked regions. Through design of the inked pattern and ordered light illumination, self-folding of 3-D box can be achieved.

Screw is a commonly used component for assembly. Conventionally, different sized screws are required for respective different sized holes. However, a SMP screw can be used as a one-for-all solution for a range of different sized holes with/without thread, which virtually turns screw drivers to be unnecessary for tightening [8].

While we are enjoying the conveniences brought to us from the development in advanced technologies, obsolete electrical devices have become a big environmental threat. Active disassembly using SMAs and SMPs has been proposed to massively disassemble them for recycling in a cost-effective manner [139-141]. Two basic concepts of active disassembly using SMPs are demonstrated here.

Figure 2.4 shows automatic opening of a hole upon heating. The cover panel is made of SMP with an original size slightly smaller than the hole. It is compressed at high temperatures to fit into the hole and stays there firmly after cooling back to working temperatures. Upon heating to above the T_g, the SMP shrinks and consequently, the hole opens.

Figure 2.4 Automatic hole-opening upon heating [8].

A SMP screw can function as an ordinary plastic screw. However, upon heating, the thread disappears. If an electrical device is assembled using a few this kind of SMP screws but with different shape recovery temperatures, when heated gradually, the device will disassemble into parts in a step-by-step manner. As such, it becomes convenient to sort out different parts at different stages for recycling with high efficiency.

Given the low-cost, electrically nonconductive and large recoverable strain nature, SMPs are more ready for active assembly/disassembly than SMAs. The triple-SME (and multi-SME) may be utilized to integrate active assembly and active disassembly together.

(2) Deployable structures

As an actuation material, SMAs are more powerful than SMPs. The actuation stress in SMAs is at 100s MPa, while that in SMPs is normally a few MPa at the most. However, SMPs have the advantages of low cost, lightweight and large recoverable strain, and can be integrated into mechanical/strcutural design as one part or parts of a structure for load carrying under normal working situation.

Figure 2.5 demonstrates the feasibility to achieve wing morphing using SMP in an airplane model. The whole left wing is made of a piece of electrically conductive SMP. When joule heated, the SMP wing recovers its original shape and becomes flat.

Deployable structures, including wheel, mast, solar sail, solar array and antenna, etc, are expected to be compact when packed inside a launching rocket, and once in position, to change into an expanded configuration after being deployed [60]. SMP foams, which can be compressed by upon to 95%, and are stiff enough at low temperatures to carry out a reasonable amount of load after shape recovery, are ideal for such missions.

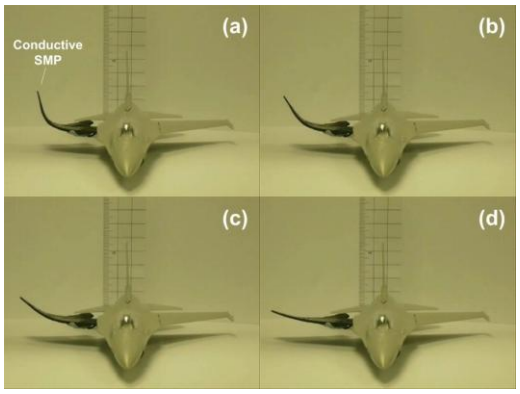

Figure 2.5 Wing morphing (in left wing) by joule heating [142].

2.3.3 Switchable information carrier

Very recently, Pretsch et al. demonstrated a new technique, which enables SMPs as switchable information carrier [143]. Two kinds of SMPs [thermoplastic poly(ester urethane) SMP and thermoset epoxy-based SMP] are colored firstly; next, the colored samples are patterned with quick response (QR) codes by laser ablation; then, the samples with QR codes are programmed to a temporary shape with non-decodable QR code information by stretching or compression; Finally, QR codes can be re-decoded after stimulus-induced recovery.

2.3.4 Smart textile

The transition temperature of shape memory polyurethane can be tailored to around humane body temperature and thus used in textile applications [90,144,145]. For instance, as proposed by Hu et al [145], polyurethane coated cotton fabrics show the wrinkle-free effect; shape memory textiles have the self-adaptability in response to the temperature change in the environment.

Chapter 3 Working mechanisms and concept of advanced shape memory technology

This chapter firstly presents a classification of all SMMs based on different working mechanisms. From these working mechanisms, the concept of advanced shape memory technology (ASMT) is proposed. ASMT includes a series of techniques to enable the SME in materials, to design a new SMM with the required features, and to optimize the SME in a SMM.

Although this dissertation is mainly focused on polymeric SMMs, other traditional SMMs are included in this classification.

3.1 Classification according to working mechanisms

The exact response of a material at the presence of a particular stimulus is dependent on not only the material itself, but also the working conditions. As such, instead of classifying various types of SMMs according to their composition and micro-structure as in many previous studies on SMPs in the literature (e.g., [1, 6, 112]), considering the exact working mechanism provides a clear yet simple approach to systematically sort out all SMMs with minimal effort but high efficiency.

In the course of this study, loading was usually finished within 30 minutes; and unloading was conducted at low temperatures. Therefore, the influence of unsteady behavior (relaxation and creeping) is relatively small. For simplification, all time-dependent parameters are ignored in the discussion followed. We assume all processes and sub-processes are instantly finished when the specified temperature and stress/strain conditions

are reached. Relaxation and creeping, which are commonly observed in viscous materials, particularly in polymers, are not considered.

The SME in SMMs can be classified into different categories according to their basic working mechanisms as illustrated in Figure 3.1. As we can see, the working mechanisms of all SMMs actually fall under three categories, namely dual-state mechanism (DSM) (I), dual-component mechanism (DCM) (II), and partial-transition mechanism (PTM) (III).

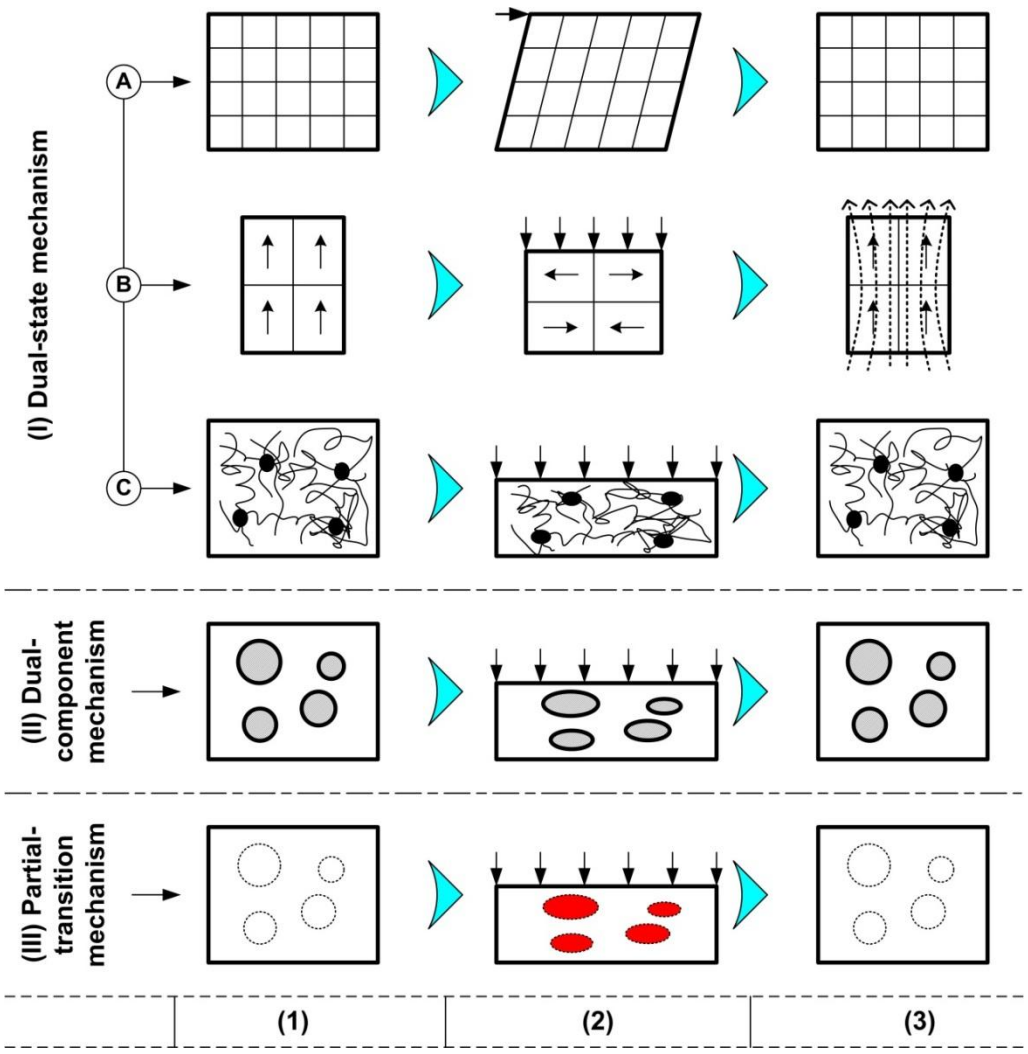

Figure 3.1 Basic working mechanisms for the SME. (I) Dual-state mechanism (DSM); (II) dual-component mechanism (DCM); (III) partial-transition mechanism (PTM). (1) Original shape; (2) after programming; (3) after shape recovery.

3.1.1 DSM based SMMs

It can be seen that there are three subgroups in Figure 3.1(I). In (I-A), a SMM is deformed and then heated up for shape recovery. A typical example of such is the SME in NiTi SMA [98]. There are a high temperature-favored austenitic phase and a low temperature-favored martensitic phase in NiTi SMA. Either stress-induced martensitic transformation or stress-induced martensite reorientation results in detwinned martensite, which is one phase (corresponding to the temporary shape). The recovery shape (original shape) is actually in the high temperature austenite phase (or maybe twinned martensite phase after subsequently cooling). As a special case, the collapse of dislocation loops during annealing, which results in shape recovery in zinc [29], is also under this subgroup.

Figure 3.1 (I-B) refers to a SMM, which changes shape upon stressing. Subsequent recovery can be triggered by applying a particular field, which has a special direction. A typical example of this kind of SMM is shape memory ceramic (SMC), which undergoes ferroelectric (FE) and antiferroelectric (AFE) transformation, or ferromagnetic (FM) and antiferromagnetic (AFM) transformation [146, 147]. There are some different domains. Switching of individual domains can be induced electrically or magnetically.

Figure 3.1 (I-C) illustrates a kind of polymeric SMM, in which there is a dual-state transition (between the glassy state and the rubbery state) triggered by external stimulus. Different from (I-A) and (I-B), the SME in polymeric SMMs is mainly due to the frozen and activation of the hyper-elastic behavior upon cooling and heating to below and above T_g. In addition, the plasticizing effect by means of immersing into the right chemical is another approach for shape recovery. Hence, generally speaking, all polymers naturally

have the thermo-/chemo-responsive SME by means of utilizing the glass transition. We can conclude that by utilizing the glass transition, all elastomers are naturally SMP. As in (I-A) and (I-B), there are also two states. Hence, all of them are DSM.

Among many others, high molecular weight polycarbonate (PC) and poly(methyl methacrylate) (PMMA) are two typical examples belonging to this category. As pointed out by Xie [46], good *cross-linked* crosslinks (including physical cross-linking, e.g., tangling, chemical cross-linking, and non-covalent interaction etc [148-151]) are required to ensure a high shape recovery ratio. We may consider that upon cooling to below T_g, elastic stress in the rubbery state of a distorted polymer is stored in the glassy state of the polymer, which provides the driving force for subsequent thermally induced shape recovery.

Now, we examine the SME in PC, which is an amorphous glassy polymer. PC sheets (Makrolon®) used here were purchased from Bayer Material Science. A DSC Q200 machine from TA Instruments was used to conduct differential scanning calorimeter (DSC) tests between 20°C and 200°C at a heating/cooling rate of 10°C/min. According to Figure 3.2, the T_g of PC is about 145°C.

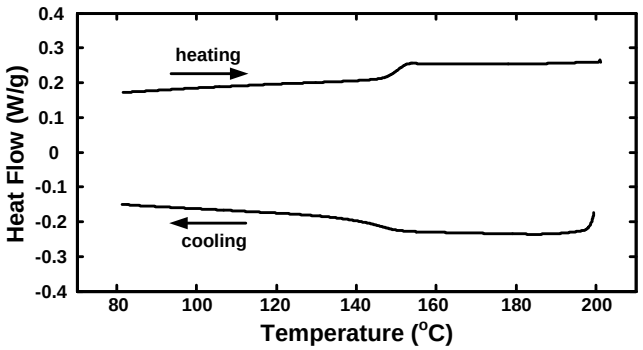

Figure 3.2 DSC result of PC.

Figure 3.3 reveals thermally induced full shape recovery in PC after micro-scale indentation at room temperature (about 22°C). A micro-hardness tester (CSM instruments) with a standard Vickers or spherical was used to make indentations atop PC. The maximum load was 100 mN, which was applied at a speed of 5 mN/s with a 10 s holding period before unloading. After indentation, PC samples were heated at 150°C for 10 mins. Surface morphologies before and after heating were examined using a confocal optical surface imaging profiler (Sensofar® PLμ). Full recovery was observed, which proves the excellent SME in PC.

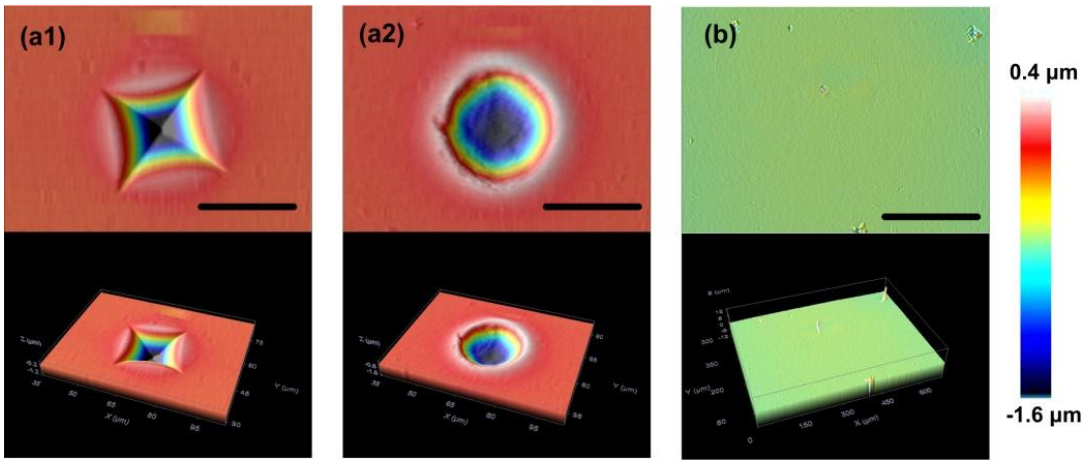

Figure 3.3 Shape recovery of micro-indented PC. (a) After indentation at room temperature; (b) recovery after heating to 150°C. Scale bar: 20 μm.

3.1.2 DCM based SMMs

The SME in ethylene-vinyl acetate (EVA) has been reported many years ago (e.g., in [152]). EVA is a typical copolymer in which one segment is always highly elastic within the whole working temperature range of the interest (elastic segment, which has a relatively higher softening temperature), while the other is able to reversibly change its stiffness from very soft at high temperatures to hard at low temperatures (transition

segment, which has a relatively lower softening temperature). As shown in Figure 3.4, after cooling, a piece of EVA ring, which is expanded during heating to above its transition temperature (the softening temperature of the transition segment), is able to keep the new shape in a larger diameter virtually forever, before being reheated again to fully recover its original size.

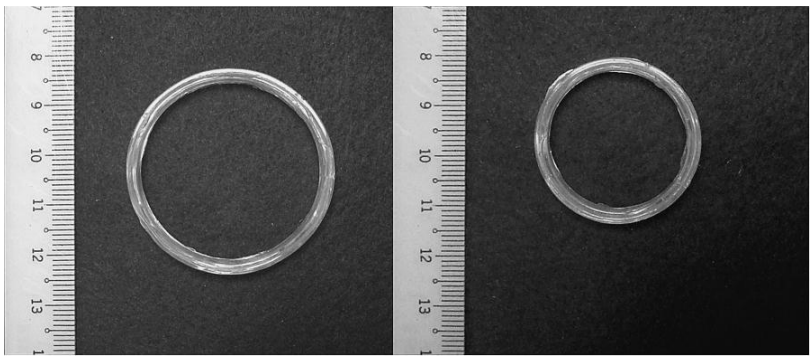

Figure 3.4 Thermo-responsive SME in EVA. (a) After expansion; (b) after heating for (full) shape recovery.

There are many other SMPs which have a similar dual-segment system. Another typical example is PU, which might be the SMP that has been subjected to the most intensive investigation (including modification) so far [134, 153-162]. According to Beloshenko et al. [93], these dual-segment polymers belong to the category of crystallisable polymers, which is the second category in Figure 3.1(II). The detail of the SME in a PU SMP is systematically described in [106]. This kind of dual-segment SMP inspires researchers to design and synthesize new SMMs by formating an elastic (hard segment) phase and transition (soft segment) phase. Materials under Category II are not limited to the ones with a dual-segmented structure, but they include all polymeric materials, which have a dual-component system, i.e., two segments or two domains (illustrated as a matrix/inclusion system in Figure 3.1II).

As an expansion of dual-segment SMMs, a new group of SMMs, known as shape memory hybrid (SMH), emerges recently. In these SMHs, one component functions as the elastic matrix, while the other component functions as transition inclusions [163].

The working mechanism of DCM is as follows. Take a dual-domain polymer as an example. Refer to Figure 3.1(II), in which the matrix is the elastic component and the inclusion is the transition component. Upon heating to above the transition temperature of the transition component, the inclusions soften. A force is applied to deform the material (illustrated by compression in Figure 3.1II). While the matrix deforms elastically upon loading, the inclusions *flow* accordingly to accommodate the distortion. After cooling to below the transition temperature, the inclusions freeze and become hard. Upon removal of the constraint, the distorted inclusions, which are hard now, prevent the matrix from recovering its original shape. A residual strain is observed and elastic energy is stored in the matrix. This is the end of the programming process. Upon subsequent heating to above the transition temperature of the transition component, the inclusions soften again and thus the matrix is able to elastically bounce back and return to its original shape.

3.1.3 PTM based SMMs

Above two types of mechanisms have already been explicitly or implicitly spelled out in the literature in different ways. All previous discussions about SMP classification are actually limited to within these two mechanisms only, although the exact chemical structures are often taken as the reference to determine which category a polymer should belong to. There is one type (III) which seemingly has never been mentioned, despite

some of the reported experiments in the literature have actually implemented this mechanism, at least to a certain sense.

This mechanism (Type III), named PTM in Figure 3.1(III), is applicable to not only polymeric materials but also metallic materials. As shown in Figure 3.1(III), a material is partially heated so that a part of it (inclusions) softens. Upon deforming the material, the matrix (non-transition component, which is still elastic) is able to elastically deform, while the softened inclusions, just like the transition component in DCM, *flow* to accommodate the shape change. After cooling and removal of the applied constraint, the material is not able to return to its original height due to the constraint from the deformed inclusions (which are hard now). When being heated again to the previous heating temperature (precisely following the previous heating procedure), the inclusions soften again and thus, due to the elastic recovery of the matrix, the SME is observed.

Practically, this mechanism may work along or together with other two mechanisms. If working alone and the utilized phase transition is melting, the issue of thermal control becomes critical. Heating temperatures (both in programming and in thermally induced shape recovery) need to be carefully selected according to the precise transition progress vs. temperature relationship, and well-controlled in terms of temperature distribution during thermal cycling to ensure good SME and high repeatability.

The feasibility to realize the SME by implementing PTM is demonstrated in paraffin wax and melting glue by means of indentation test. The utilized transition is melting in both materials. To avoid being confused by melting induced flowing which may virtually cause

some-kind of shape recovery, an indentation-polishing-heating (IPH) approach is adopted to examine the SME in a convincing manner [164-166].

Figure 3.5 reveals the shape memory phenomenon in paraffin wax (C_nH_{2n+2}, usually with n between 20 and 40) bought from Agar Scientific Limited, England.

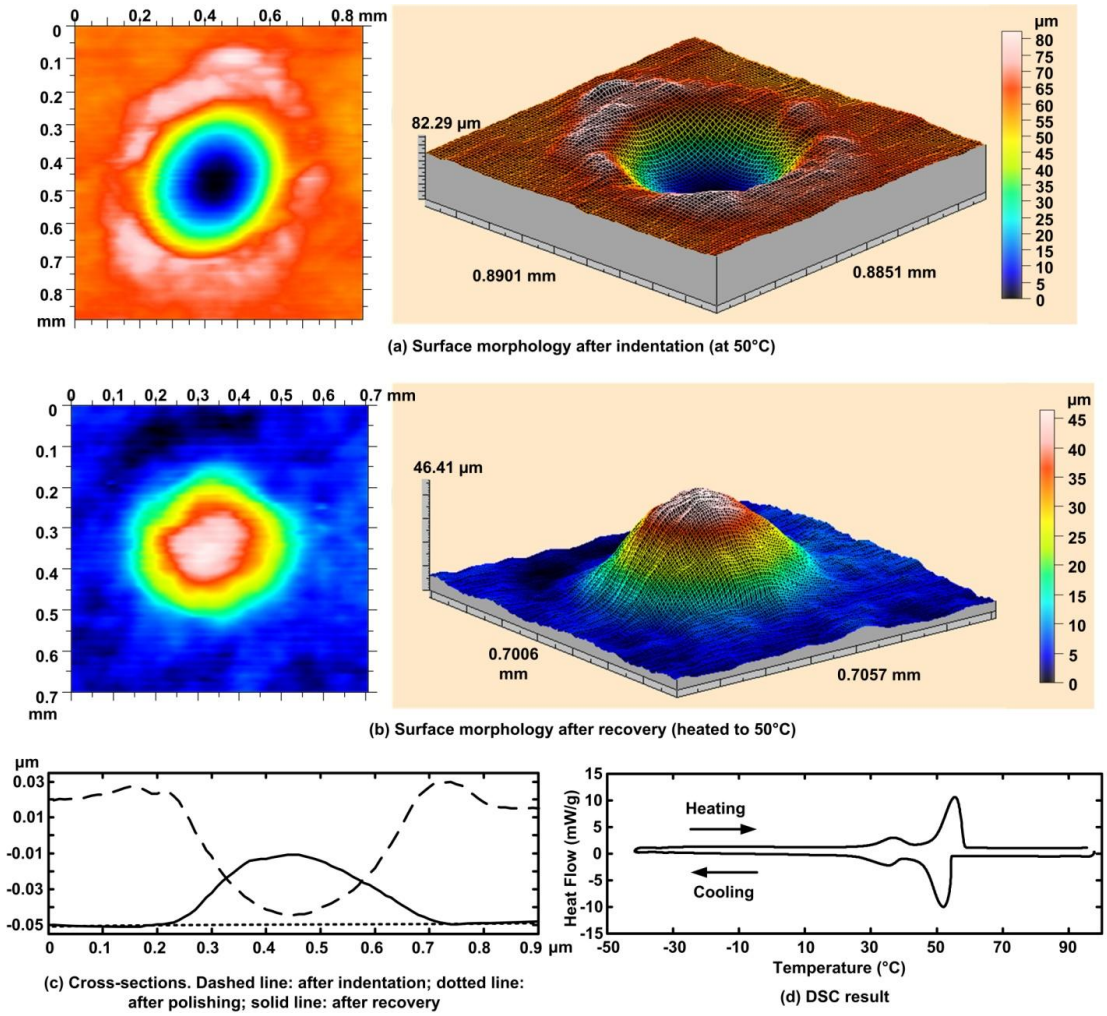

Figure 3.5 Shape recovery in paraffin wax.

According to the DSC result in Figure 3.5(d), this paraffin wax has two melting peaks at 45°C and 56°C, respectively. A spherical indent was made when the wax was heated to 50°C in an oven using a 1 mm diameter steel ball.

After cooling, Taylor Scanner (Taylor Hobson) was used to scan the surface (Figure 3.5a). Subsequently, the indented sample was polished using a sand paper (grid 1200) till the indent just disappeared.

After polishing, the sample was reheated to 50°C for 5 mins. Finally, the sample surface was scanned again by Taylor Scanner (Figure 3.5b). The cross-sections after indentation, polishing and reheating are plotted together in Figure 3.5(c), which clearly reveal the SME as a protrusion was formed after reheating.

Figure 3.6 reveals a similar test conducted on Sellery melting glue. Melting glue stick (5/16"×4" 96-801) bought from Centenary Materials Co., Ltd., Taiwan (under authorization of Sellery Inc. California U.S.A.) contains EVA as its main component. Its nominal density is 0.896 g cm^{-3}.

According to the DSC result in Figure 3.6(e), this melting glue has a melting range from 40°C to 70°C. A spherical indent was made upon heating to 55°C in an oven using the same steel ball. After indentation, Taylor Scanner was used for surface scanning (Figure 3.6a). Subsequently, a thin layer was removed by a sharp knife.

According to the result of surface scanning (Figure 3.6b), the removed layer is about 100 μm. After reheating to 55°C for 5 mins, a protrusion was formed (Figure 3.6c). The cross-sections after indentation, polishing and reheating are plotted together in Figure 3.6(d) for comparison. Clear SME is observed.

In the PTM, in theory, in order to achieve high shape recovery ratio, the deformation should be within the small strain range. However, the exact strain limit also depends on

the elasticity of the exact material, which is made of. It should be pointed out that although the elastic strain limit might be low, the overall deformation in a porous material can be high.

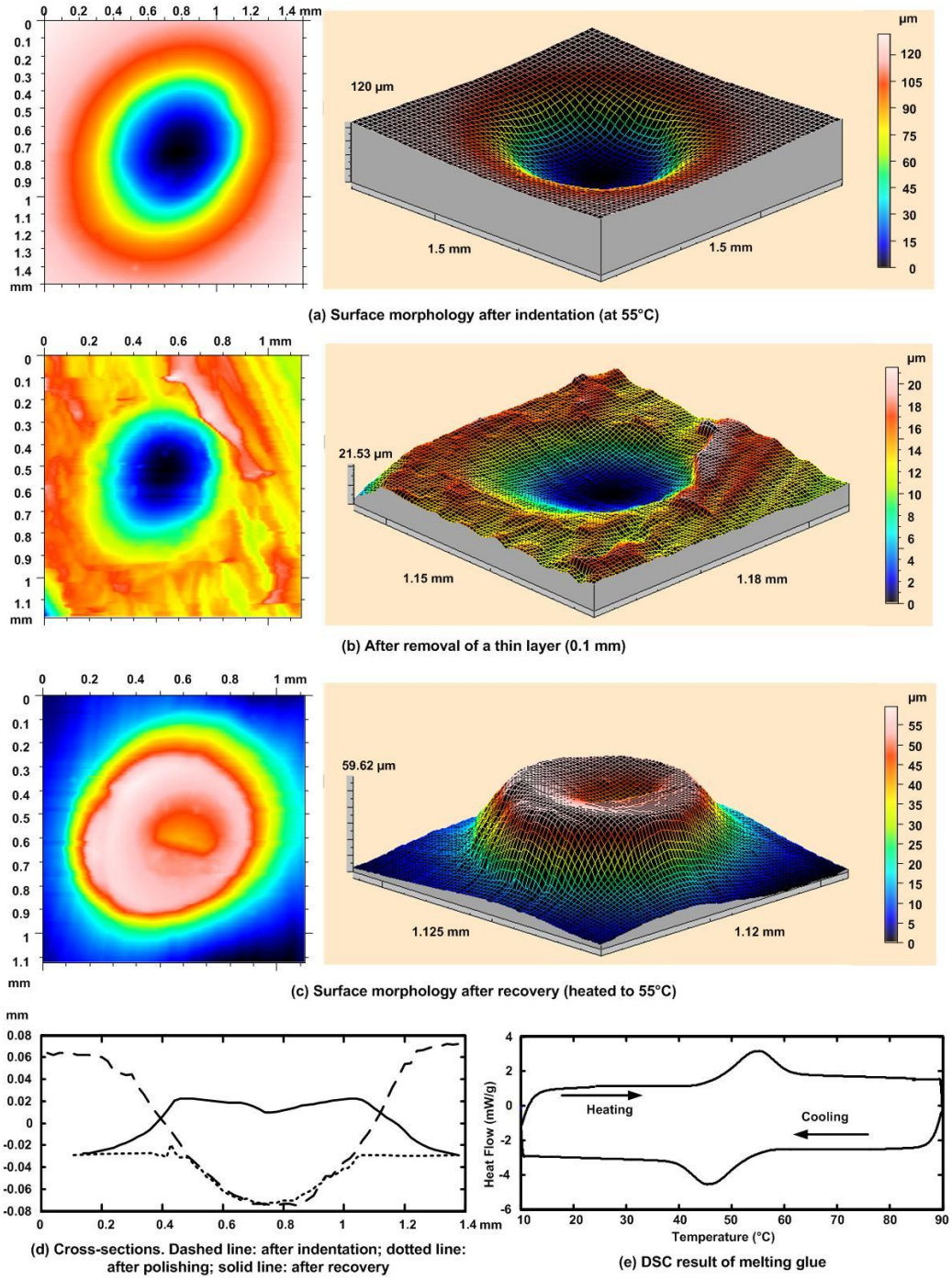

Figure 3.6 Shape recovery in melting glue.

3.2 Advanced shape memory technology

The term of shape memory technology (SMT) has been used in 1990's for SMA related techniques. By utilizing the above three mechanisms either individually or in a combination manner, we may achieve the SME in almost any polymeric materials and even in metallic materials; and design/synthesize new SMMs in a tailored fashion. Moreover, we can optimize the SME based on the fundamentals of these mechanisms. As such, this is advanced SMT, which includes a number of techniques in these above mentioned three areas.

3.2.1 Realization of the SME in materials

When considering a *new* material, in many occasions, we may not have full knowledge of it, and/or the material itself might be very much complicated, e.g., it might be a mixture or a hybrid/blend of many components (supposed to be microscopically uniform, at least, relative to the dimension scale in an application). On the other hand, from real engineering application point of view, the concern is more about achieving the SME to meet the required shape memory performance, without caring much about the exact working mechanism. As such, from engineering application point of view, an approach following PTM can be the starting point to enable the SME in many materials.

Two samples (one is polymeric material and the other is metallic material) were used to demonstrate the implementation procedure for the thermo-responsive SME in real practice. The polymeric material is BIOCOM® DPEF9910 multi-degradable resin (BIOCOM DR), purchased from NAFT Asia Biodegradable Plastic, Singapore. BIOCOM DR used in this

study has a melt flow index of 1.5~2.0 g/10 min. The metallic material is solder (Sn32PbAg) from Multicore, Malaysia.

The first step is to conduct a DSC test to find out the location of the transition temperature range. Glass transition, melting and other transition are possible candidates for consideration. Refer to Figure 3.7 for the DSC results of both materials. For BIOCOM DR, during heating there are two melting temperature ranges. One is from 45°C to 70°C, and the other is from 110°C to 130°C. For Sn32PbAg, its melting temperature range is from 178°C to 187°C during heating.

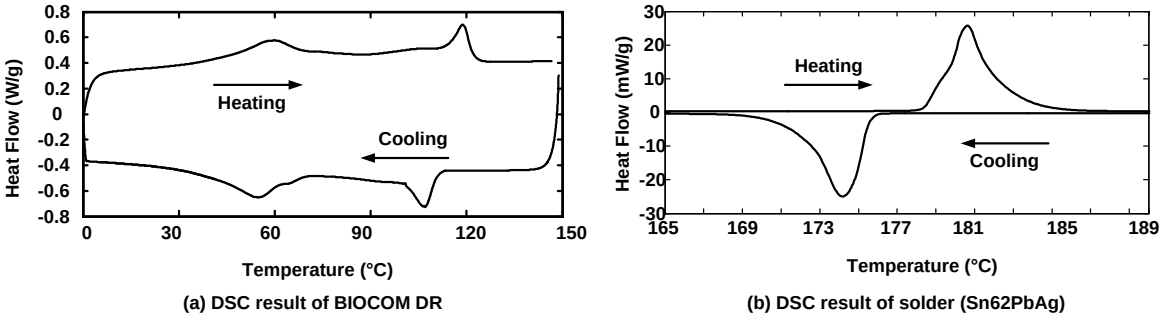

Figure 3.7 DSC results.

The next step is to select the heating temperature (within the transition range) for deformation (programming). To avoid (or at least to minimize) the damage to the elastic network, which reduces the shape recovery ability of a material, it is suggested to select a heating temperature which corresponds to the lower half of the transition range.

Similar to the above mentioned two cases of paraffin wax and melting glue, a 1 mm diameter steel ball was used to make indents atop BIOCOM DR and Sn32PbAg. Two T_ps for BIOCOM DR were 60°C and 120°C, respectively. The T_p for Sn32PbAg was 179°C.

After cooling back to room temperature and removal of the steel ball, indents were formed atop BIOCOM DR and Sn32PbAg.

For BIOCOM DR, the indent became shallower after reheating to the previous heating temperature in indentation (Figure 3.8).

For Sn32PbAg, the indented sample was polished to remove a 110 μm thin layer using a sand paper (grid 1200). After polishing, the sample was reheated to 179°C for 5 mins. Obvious shape recovery was observed in Sn32PbAg (Figure 3.9).

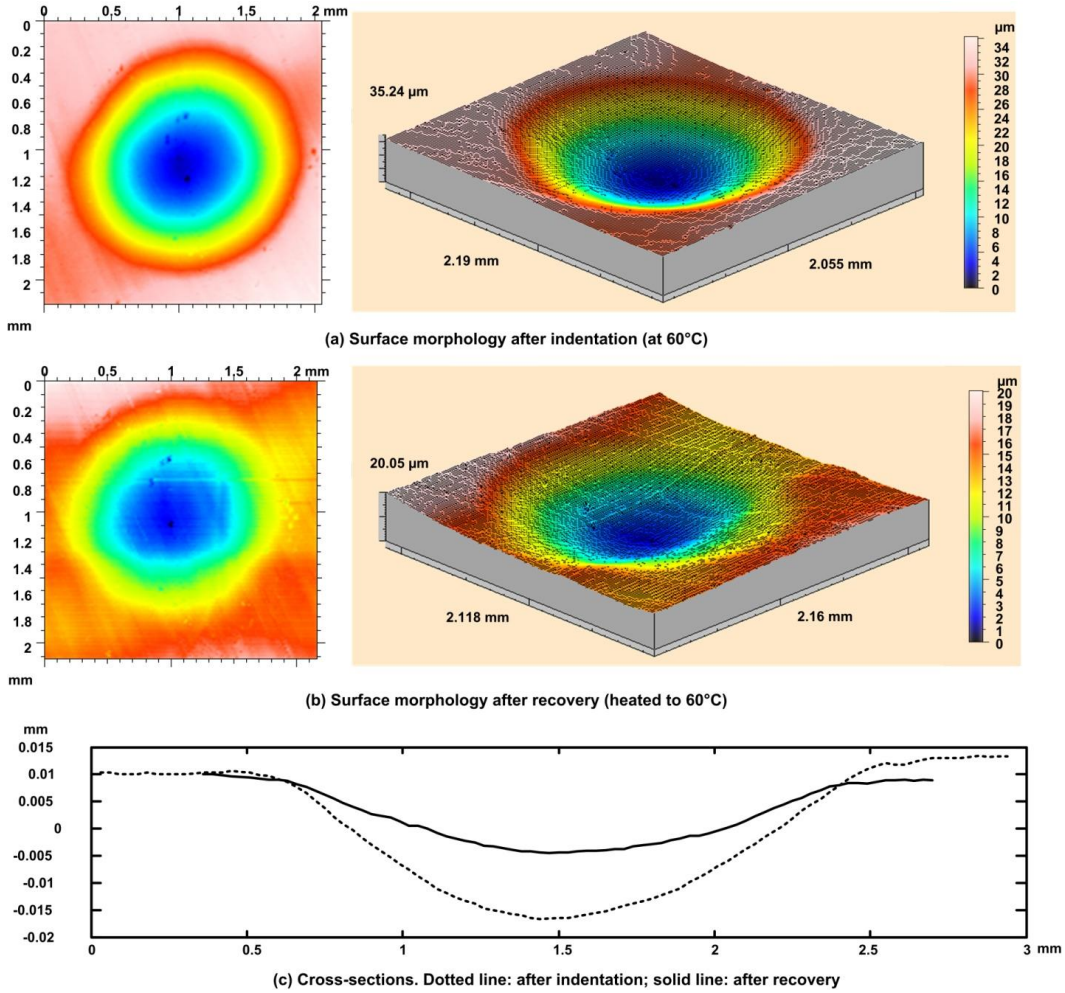

(I) Shape recovery in BIOCOM DR programmed at 60°C.

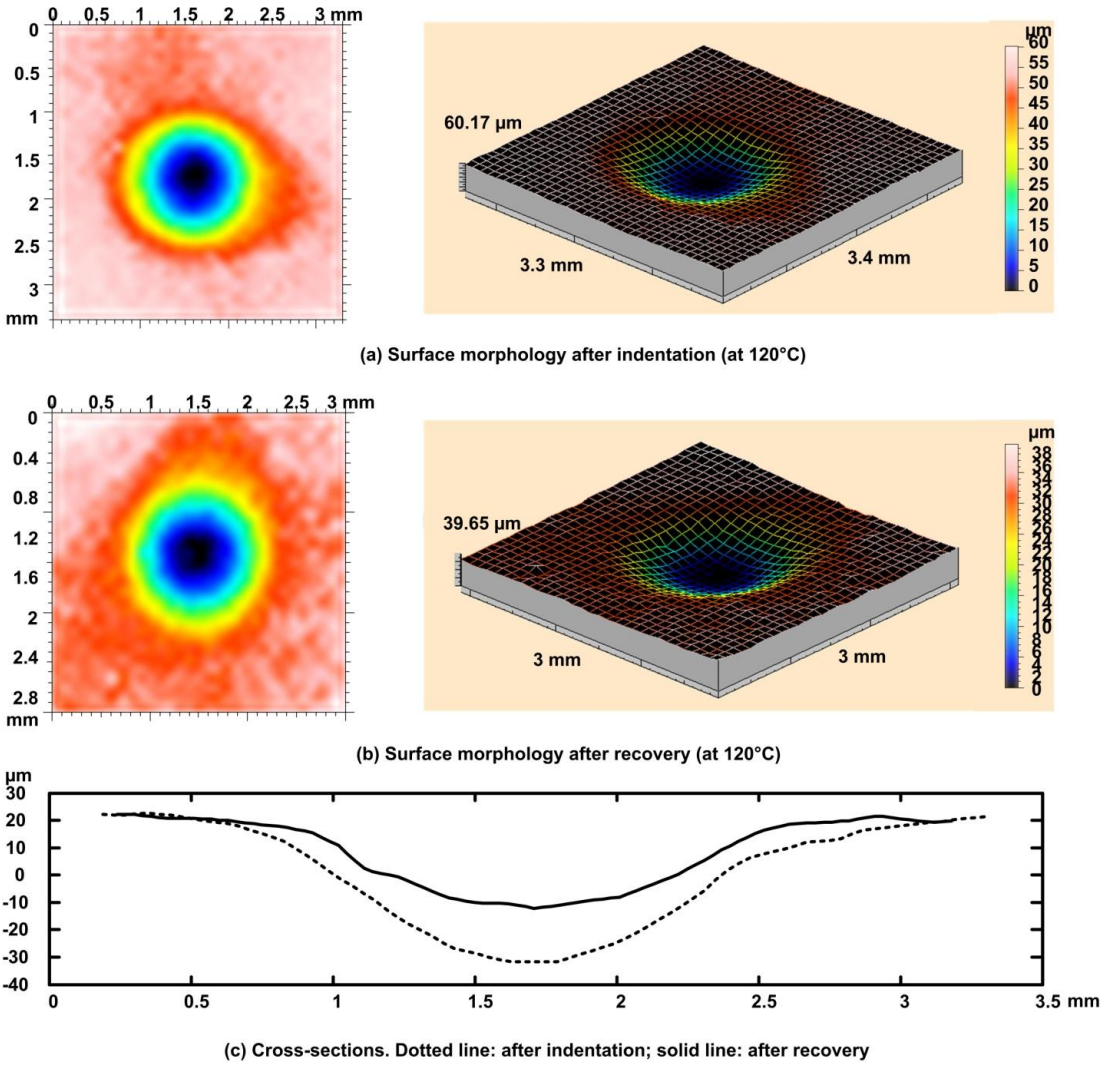

(II) Shape recovery in BIOCOM DR programmed at 120°C.

Figure 3.8 Shape recovery in BIOCOM DR.

Both materials are not reported as SMMs before. However, shape memory behavior is observed in them.

It is obvious that one of the requirements for PTM is a dramatic change in stiffness in a reversible transformation. The exact shape memory performance depends on the applied strain and the temperature in programming.

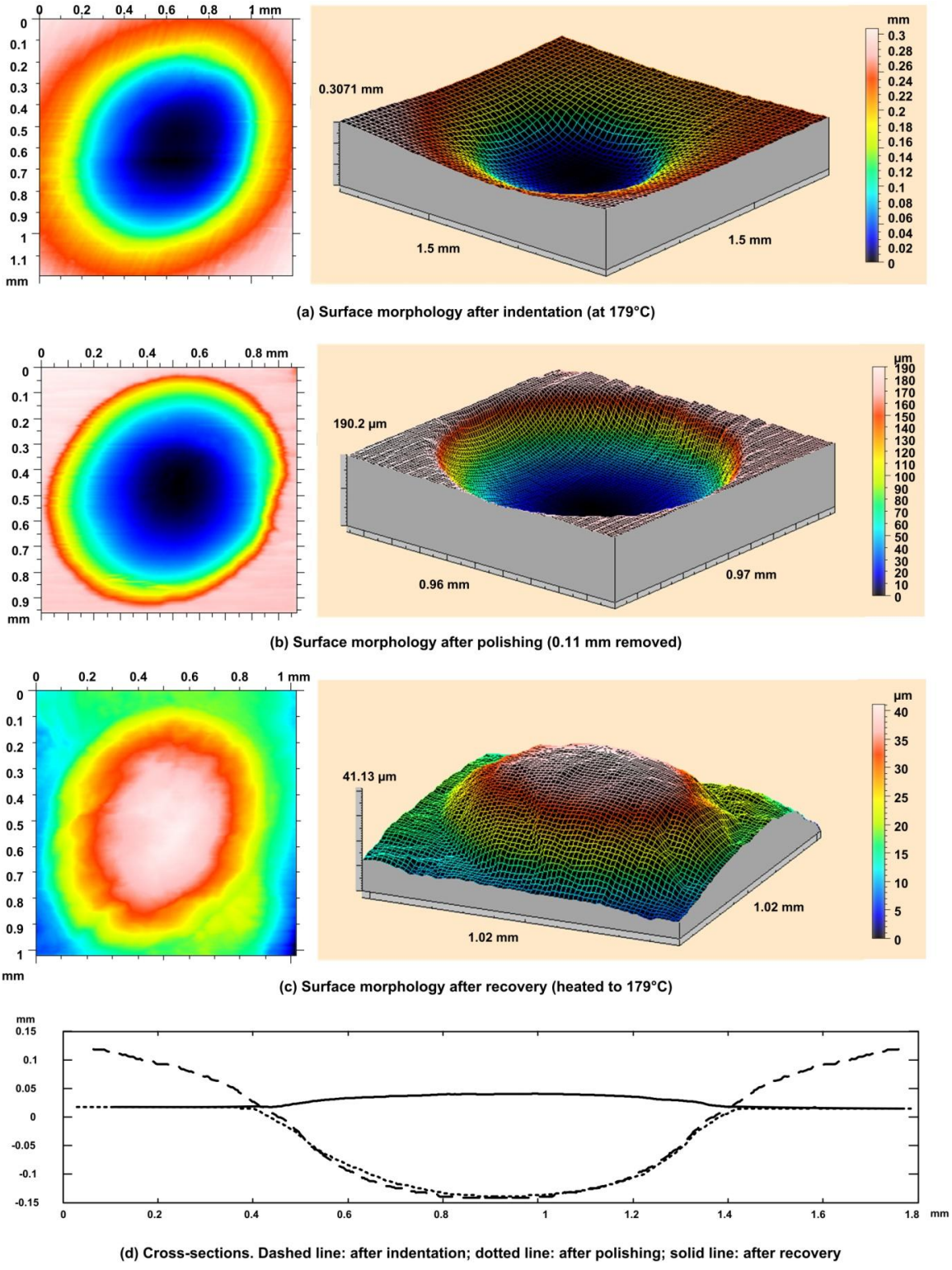

(a) Surface morphology after indentation (at 179°C)

(b) Surface morphology after polishing (0.11 mm removed)

(c) Surface morphology after recovery (heated to 179°C)

(d) Cross-sections. Dashed line: after indentation; dotted line: after polishing; solid line: after recovery

Figure 3.9 Shape recovery in solder (Sn62PbAg).

Refer to Figure 3.1(III) for the mechanism of PTM. During programming, these samples are deformed at a temperature within a transition temperature range. Hence, some parts of the materials are softened, while the rest parts are still solid. The softened parts can be easily deformed, but the solid parts are elastically deformed upon loading within the elastic range. During cooling, the softened parts solidify and thus restrain the elastic shape recovery in the samples. Subsequently, elastic energy is stored during cooling. When reheated, the stored elastic energy drives the samples to recover their original shape.

It should be pointed out that this PTM is applicable to the chemo-responsive SME as well.

3.2.2 Design/synthesize of new SMMs

The DCM concept can be utilized to design and synthesize new SMM. Based on the concept of SMH, the components for selection can be widened to include virtually any materials (including inorganic and metal/alloy, etc), so that tailored features and functions can be easily achieved. For high performance SMHs, the interaction between the elastic component and transition component should be avoided or at least minimized by means of materials selection and processing selection. An extensive study about this topic is reported in [163].

3.2.3 Optimization of the SME

Instead of discussing chemical composition tuning which is very much dependent on the individual type of material, we investigate the generic principles in the optimization of the SME from the aspects of mechanics and mechanism design. In this section, we discuss a

generic method to alter a number of properties of a material, namely R_f, T_r, R_r, and σ_r, simply by means of selecting the T_p to achieve optimized performance.

From the mechanical function point of view, *cross-linked* crosslinks and switch segments in DSM, which were pointed out by Xie [46] as the two structural requirements for the SME, are roughly corresponding to the elastic component and transition component in DCM and PTM, respectively. Consequently, the SME in polymers under all three working mechanisms can be integrated and discussed under one single umbrella, i.e., a material system, which consists of an elastic component (may be simplified as matrix in discussion) and a transition component (may be considered as inclusions).

It is obvious that high elasticity in the elastic component (to avoid permanent distortion, which is supposed to be irrecoverable), and "plastical" distortion in the transition component (so that the residual deformation can be largely maintained) are two apparent conditions. By closely examining the behavior of this matrix/inclusion system, we should be able to work out some generic conclusions, which may serve as the principles to follow in optimization of the performance of a material.

Shape fixity – Figure 3.10(a) presents the maximum compressive stress in programming vs. T_p relationships of BIOCOM DR at two maximum programming strains, namely 5% and 10%. The selected temperatures for programming are around the 1st melting transition in heating (Figure 3.7a). It is confirmed that with an increase in programming temperature, the maximum compressive stress decreases monotonically at both maximum strains. Figure 3.10(b) reveals the shape fixity ratio vs. programming temperature relationship. A quasi-linear relationship is observed between R_f and T_p at both 5% and 10% strains. As

expected, a higher maximum programming strain results in a higher shape fixity ratio. The shape recovery behavior of this polymer will be discussed in Section 4.2.1.

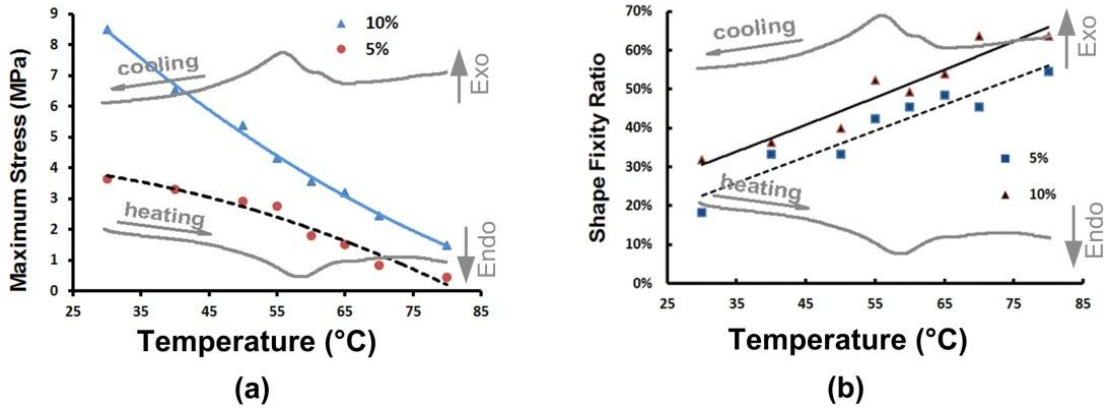

Figure 3.10 Programing BIOCOM DR at different temperatures by uniaxial compression to a maximum strain of 5% or 10%. (a) Maximum compressive stress vs. programming temperature relationship; (b) shape fixity ratio vs. programming temperature relationship. Embedded grey curves are DSC results at a heating/cooling rate of 10°C/min for reference.

Free recovery – In a standard free recovery test, strain variation in a piece of free standing sample is recorded during heating. For different T_ps (all within the transition range), the strain recovery curves are about parallel to each other. T_r^s, T_r^f and T_{sw} (refer to Section 2.1.1) are related to T_p. All of them increase with the increase of T_p. In the literature, this phenomenon is called strain based TME [46].

Figure 3.11 demonstrates this phenomenon in PMMA. PMMA cylindrical samples with a diameter of 10 mm and a height of 3 mm were uniaxially compressed to a maximum strain of 50% at a rate of $0.01s^{-1}$ at different T_ps (within the glass transition range) by Instron 5569. These samples were unloaded after cooling back to 20°C. Subsequently, dynamic mechanical analysis (DMA) tests were conducted with a small constant compressive force

of 1 mN applied. They were heated to 160°C at a heating rate of 10°C/min. The shape recovery upon heating was monitored.

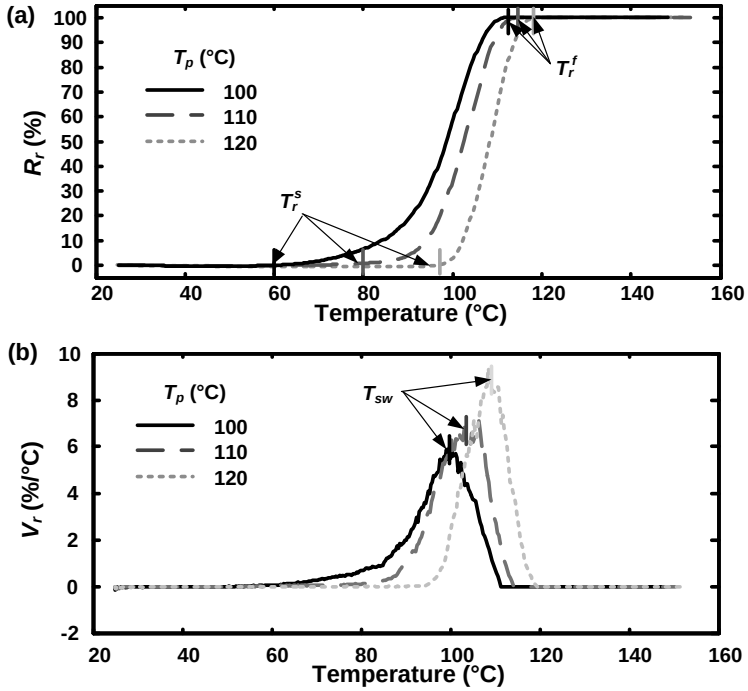

Figure 3.11 Free recovery in pre-compressed PMMA. (a) Evolution of strain recovery; (b) evolution of strain recovery rate.

Constrained recovery – In a standard constrained recovery test, stress variation is recorded when a pre-programmed sample is heated at a constant rate under a constrained condition. We can observe a force/stress peak upon gradually heating.

Figure 3.12 reveals the σ_r vs. T_p curves in pre-stretched PMMA. σ_r continuously increases before reaching a temperature slightly below T_p, and then decreases continuously upon further heating. The temperature corresponding to the maximum σ_r, $\sigma_r^{\max}$, increases as the T_p increases. These two temperatures are normally very close to each other, i.e. the stress based TME.

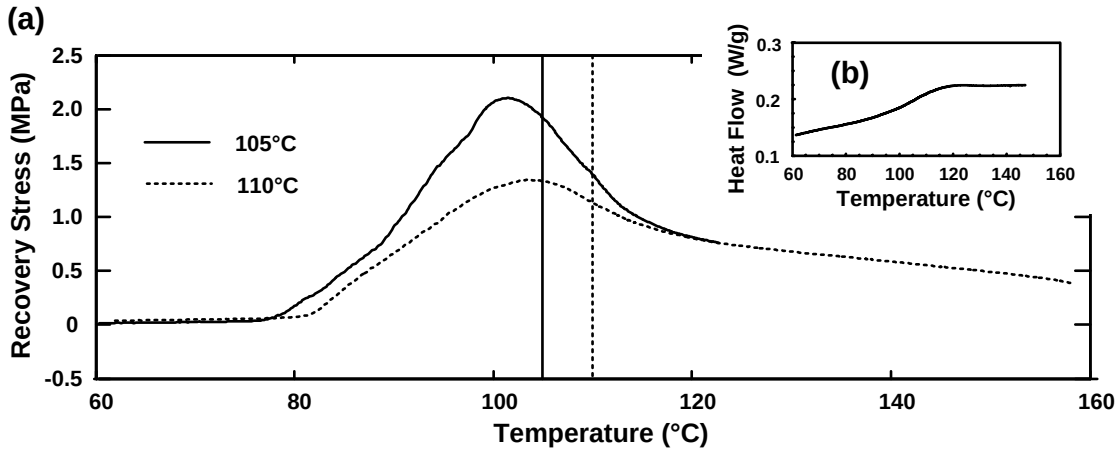

Figure 3.12 TME in PMMA. (a) Recovery stress vs. temperature curve; (b) DSC curve during heating (heating rate: 10°C/min). Samples were pre-stretched to 100% at a strain rate of $0.001s^{-1}$ at 105°C and 110°C, respectively.

Figure 3.13 reveals the TME in a melting glue sample (same as that used in Figure 3.6). As we can see, as in Figure 3.12, again σ_r^{max} increases with the decrease of T_p. But the corresponding temperatures are remarkably higher than the T_ps. A possible reason might be the difference in coefficient of thermal expansion between PMMA and melting glue.

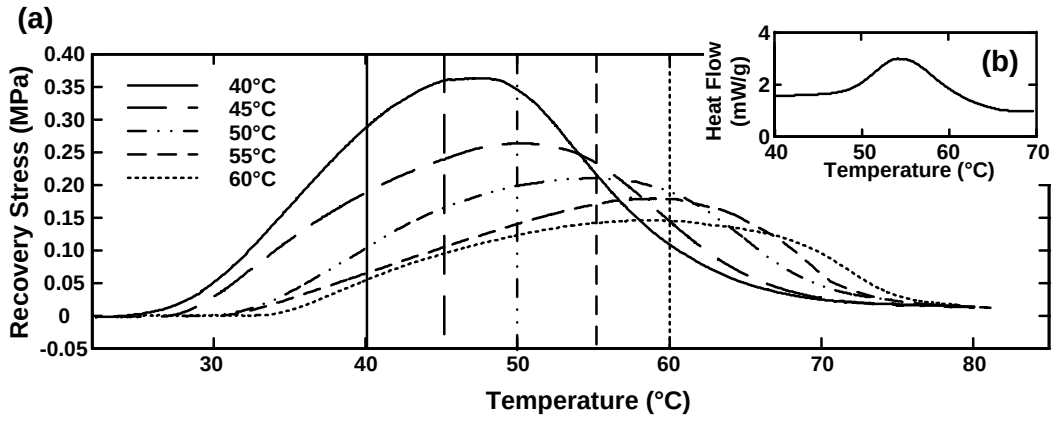

Figure 3.13 TME in melting glue. (a) Recovery stress vs. temperature curves; (b) DSC curve during heating (heating rate: 10°C/min). The applied maximum strain in programming is 30%. Applied strain rate: $0.001s^{-1}$.

3.3 Further discussion

RP-SME – In many traditional shape memory cycles, a piece of polymeric sample is deformed at above T_t (T_g or T_m). Temporary shape is fixed after cooling with a constraint applied. In addition to this high temperature programming process, shape fixing can also be achieved by meaning of programming at low temperatures ($<T_t$), i.e., the RP-SME as revealed in Figure 3.14 for a PMMA.

PMMA cylindrical samples with a diameter of 10 mm and a height of 3 mm were compressed to a maximum strain of 50% at a rate of $0.01s^{-1}$ and different T_ps ($<T_g$) by Instron 5569. These samples were unloaded after cooling back to room temperature (20°C). Subsequently, DMA tests were conducted with a small constant compressive force of 1 mN applied. Samples were heated to 160°C at a heating rate of 10°C/min. The displacement upon heating was monitored.

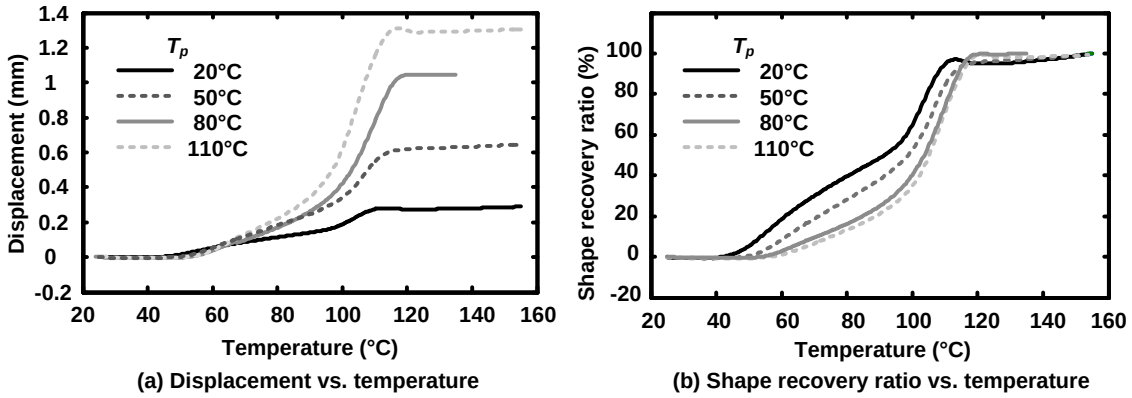

Figure 3.14 RP-SME in PMMA upon heating.

Figure 3.14(a) shows the measured displacement upon heating. Figure 3.14(b) reveals the evolution of corresponding shape recovery ratio, which demonstrates excellent SME in

PMMA. The recovery is seemingly in two-steps, a phenomenon similar to LTR and HTR discussed in Section 2.1.1. A detailed study about RP-SME is presented in Section 5.2.1.

Chemo-responsive SME – In above discussion, shape recovery is triggered by heating (thermo-responsive SME). However, chemo-responsive SME is also achievable in many materials, in particular polymeric materials.

Regardless of the exact type of stimulus, shape recovery is driven by the elastic energy stored during programming. For the thermo-responsive SME, the stored elastic energy can be released by heating to soften the transition component. For the chemo-responsive SME, the stored elastic energy is released by means of softening the transition component by solvent.

For the thermo- and water-responsive SME in PU, readers may refer to [106]. A detailed study of thermo- and ethanol- induced shape recovery in PMMA is presented in Chapter 5.

3.4 Summary

Based on the working mechanisms, we classify all SMMs into three categories. Subsequently, we propose the concept of advanced shape memory technology (ASMT) to enable the SME in materials, to design/synthesize new SMMs with tailored features, and to optimize the SME in materials. In addition, the RP-SME and chemo-responsive SME are briefly discussed.

Chapter 4 Numerical simulation of thermo-responsive SME

In order to reproduce various types of shape memory phenomena, a 3-D finite element model is developed in this chapter for thermo-responsive SME in polymeric materials. With this model, we can design a SMM and optimize its SME.

4.1 Background and constitutive model

The key issues in modeling polymeric SMMs are

- How to determine the driving force for shape recovery?
- How to simulate the macroscopic shape recovery or the evolution of recovery stress at the presence of a right stimulus?

As described in Section 3.1, for the DSM based polymeric SMMs, the driving force for shape recovery is mainly from entropy-dependent quasi-elastic deformation in the elastic network; for the DCM based polymeric SMMs, the driving force is mainly from the elastic deformation in the elastic matrix; for the PTM based polymeric SMMs, it is mainly from the elastic deformation in the solid part.

Therefore, the SME in polymers under all three working mechanisms can be integrated and discussed as a material system, which consists of an elastic matrix and a transition component.

We propose a 3-D finite element model for polymeric SMMs, which consists of several groups of randomly distributed elements standing for different states, components, or parts in polymeric SMM. For simplification, we consider a case of transition inclusions within

an elastic matrix. Individual transition inclusion might be hard or soft depending on, for instance, temperature in a thermo-responsive SMM.

Figure 4.1 illustrates a representative 3-D unit in modeling. We assume the transition inclusions are randomly distributed within the elastic matrix. The individual inclusions might be hard or soft depending on the exact temperature at a particular moment. This representative 3-D unit was used in simulation. Obviously, this 3-D finite element model follows the *phase* transition approach as discussed in Section 2.2.2.

In real situations, the inclusions are more likely to be in a spherical shape in order to minimize the surface energy. However, in current simulation, limited by the available computational resource, the representative cubic is uniformly meshed with tetrahedron elements for simplification.

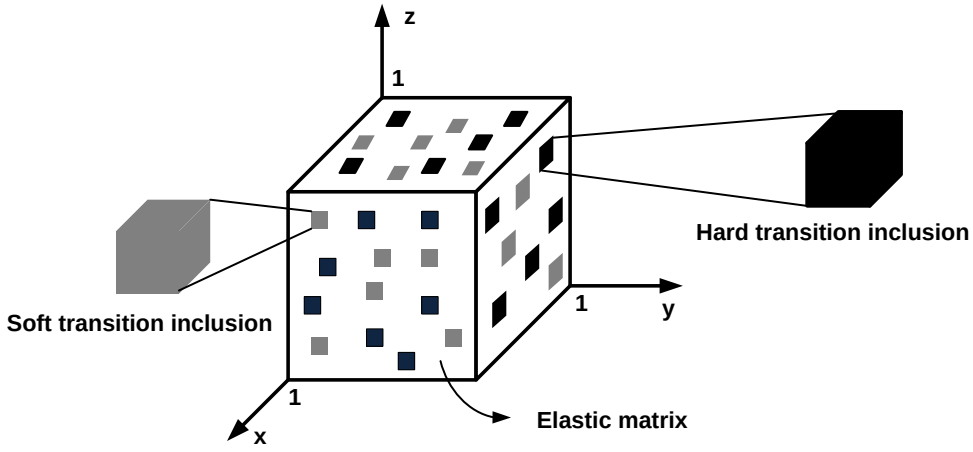

Figure 4.1 Illustration of a representative 3-D unit in modeling.

4.1.1 Determination of volume fractions

The very important parameters in a *phase* transition model are volume fractions of elastic matrix and transition inclusions, i.e., f_e and f_t, respectively.

f_t^h and f_t^s stand for the volume fractions of the total hard and soft inclusions, respectively. Therefore,

$$\begin{cases} f_e + f_t = 1 \\ f_t^h + f_t^s = f_t \end{cases} \tag{4.1}$$

During heating/cooling, a hard/soft inclusion may transfer to its opposite. Therefore, it is necessary to determine the evolution rules. For polymeric materials, there are two types of transitions, namely glassy-rubbery transition and crystalline-melting transition. We need to have formulas for the evolution of volume fractions in both transitions.

(1) Glassy-rubbery transition

Based on Qi et al. [66], the evolution of the volume fractions of glassy (hard) inclusions and rubbery (soft) inclusions may be expressed as,

$$f_t^h = f_t - \frac{f_t}{1+\exp[-(T-T_0)/A]} \tag{4.2}$$

$$f_t^s = \frac{f_t}{1+\exp[-(T-T_0)/A]} \tag{4.3}$$

where A is a parameter that characterizes the width of the glass transition zone, T_0 is a reference temperature (close to T_g). These parameters may be estimated from the actual DMA result of a particular polymer.

(2) Crystalline-melting transition

Similarly, the evolution of the volume fractions of solid and melted inclusions may be calculated by,

$$f_t^h = f_t[1-\frac{S(T)}{S_{total}}] \tag{4.4}$$

$$f_t^s = f_t \frac{S(T)}{S_{total}} \tag{4.5}$$

where $S(T)$ and S_{total} are the areas in partial and full melting transitions in a DSC curve, as illustrated in Figure 4.2.

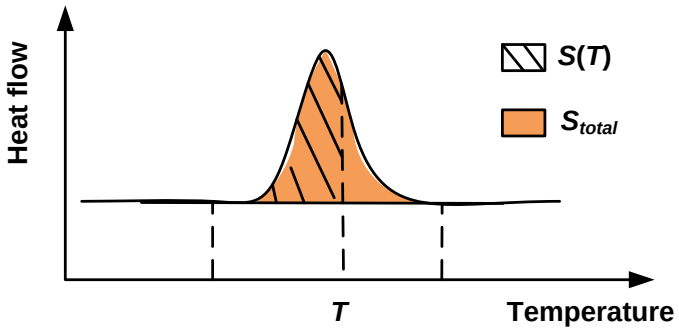

Figure 4.2 Illustration of typical DSC curve in melting.

Take note that Eqn. (4.1) follows the simple mixing rule for composites. Sophisticate interaction among individuals at small scales is not considered. Hence, we can focus more on various SMEs. Different actual transition temperatures need to be pre-assigned to individual inclusions according to f_t^h and f_t^s.

4.1.2 Material model and constitutive laws

Depending on the exact mechanical properties, different constitutive laws should be selected for different materials.

In this project, simulation is conducted using a commercial software (ANSYS), which already has a library of classical constitutive laws for almost a full range of material

models. At least four kinds of material models can be used for elastic matrix, and hard/soft transition inclusion in simulation.

4.1.2.1 Ideal elastic model

For elastic matrix, an ideal elastic model may be used to represent its deformation behavior. The constitutive law for an ideal elastic model can be expressed by Hooke's law. For an isotropic material,

$$\boldsymbol{\varepsilon} = \frac{1}{E}\boldsymbol{\sigma} - \frac{v}{E}\left[\mathrm{tr}(\boldsymbol{\sigma})\mathbf{I} - \boldsymbol{\sigma}\right] \tag{4.6}$$

where $\boldsymbol{\sigma}$ is stress tensor, $\boldsymbol{\varepsilon}$ is strain tensor, E is the Young's modulus, and v is the Poisson's ratio.

The exact material properties can be determined by uniaxial tension or compression test.

4.1.2.2 Elasto-plasitc model

An elasto-plastic model may be used for the elasto-plastic behavior of a material. The yield criterion follows the von Mises yield criterion [167]. A material starts to yield when the von Mises stress reaches the yield strength, σ_y. Before yielding, the constitutive law is same as Eqn. (4.6). After yielding, an isotropic hardening rule may apply,

$$\sigma = \sigma_y + E_h(\varepsilon - \varepsilon_y) \tag{4.7}$$

where E_h is the tangent modulus for hardening, and ε_y is the strain corresponding to σ_y. The exact material properties can be experimentally determined by uniaxial tension or compression test.

4.1.2.3 Hyper-elastic model

Arruda-Boyce eight-chain model is applicable to describe the response of polymers in rubbery state, which is essentially hyper-elastic behavior [79, 84, 86, 87, 168, 169]. The Cauchy stress tensor (**T**) may be expressed as [141, 142],

$$\mathbf{T} = \frac{\mu}{3J}\frac{\lambda_L}{\lambda_{chain}}\mathbf{L}^{-1}\left(\frac{\lambda_{chain}}{\lambda_L}\right)\bar{\mathbf{B}}' + k[J-1-3\alpha(T-T_0)]\mathbf{I} \tag{4.8}$$

where μ is the initial shear modulus, λ_L is limiting chain stretch, k is bulk modulus, α is the coefficient of thermal expansion, and T_0 is the initial temperature in an analysis. If **F** is the overall deformation gradient, the volumetric strain is $\bar{\mathbf{F}} = (1/J^{1/3})\mathbf{F}$, where J=det[**F**]. $\bar{\mathbf{B}}$ is the isochoric left Cauchy-Green tensor, $\bar{\mathbf{B}} = \bar{\mathbf{F}}\bar{\mathbf{F}}^{\mathrm{T}}$, and $\bar{\mathbf{B}}' = \bar{\mathbf{B}} - 1/3\,\mathrm{tr}(\bar{\mathbf{B}})\mathbf{I}$ is the deviatoric part of $\bar{\mathbf{B}}$. $\lambda_{chain} = \sqrt{\bar{I}_1/3}$ is the stretch in each chain in the eight-chain network, and $\bar{I}_1 = \mathrm{tr}(\bar{\mathbf{B}})$ is the first invariant of $\bar{\mathbf{B}}$. **L** is the Langevin function.

The exact materials properties can be experimentally determined by uniaxial tension or compression test.

4.1.2.4 Visco-plastic model

For a glassy state polymer, its visco-plastic behavior can be characterized by rate-dependent yielding, rate-dependent strain softening and hardening. Peirce model [170] is applicable for rate-dependent yielding,

$$\sigma_y = \sigma_{y0}\left(1+\frac{\dot{\varepsilon}^{pl}}{\gamma}\right)^m \tag{4.9}$$

where $\dot{\varepsilon}^{pl}$ is equivalent plastic strain rate, γ is a viscosity parameter, m is strain rate hardening parameter, and σ_{y0} is static yield stress of a material.

Before yielding, the constitutive law is same as Eqn. (4.6). After yielding, a combination of strain softening/hardening curves determines the exact response,

$$\varepsilon^{pl} = \sum_{i=1}^{n} \varepsilon_i^{pl}, \quad \sigma^{pl} = \sum_{i=1}^{n} K_i \varepsilon_i^{pl} \tag{4.10}$$

where n and K_i are parameters to determine the exact function of the strain softening and hardening curve, ε^{pl} and σ^{pl} are equivalent plastic strain and stress after yielding, subscript i represent subsection in the strain softening/hardening curve. In order to overcome computational difficulties due to zero and negative K_i, a very small positive K_i may be used.

The effective material properties are determined by the properties of individual components. Following the simple Voigt mixing rule for composites, the overall stress tensor, $\boldsymbol{\sigma}$, may be expressed by the volume fractions and stresses of individual parts as

$$\boldsymbol{\sigma} = f_e \boldsymbol{\sigma}_{\mathbf{e}} + f_t^h \boldsymbol{\sigma}_{\mathbf{t}}^{\mathbf{h}} + f_t^s \boldsymbol{\sigma}_{\mathbf{t}}^{\mathbf{s}}, \tag{4.11}$$

where $\boldsymbol{\sigma}_{\mathbf{e}}$ is stress tensor of elastic matrix, $\boldsymbol{\sigma}_{\mathbf{t}}^{\mathbf{h}}$ is stress tensor of the hard transition inclusions, and $\boldsymbol{\sigma}_{\mathbf{t}}^{\mathbf{s}}$ is stress tensor of the soft transition inclusions.

Generally speaking, thermo-mechanical behavior of polymeric SMMs can be very complicate. We need to be careful in selecting material models.

Table 4.1 summarizes the material parameters in above mentioned models, which were used in our simulation. These material parameters can be estimated experimentally or selected from a material manual.

Table 4.1 Material properties.

Material model	Parameters
Elastic	E, v
Elasto-plastic	E, v, σ_y, E_h
Hyper-elastic	μ, λ_L, k
Visco-plastic	E, v, σ_{y0}, m, γ, n, K_i

4.1.3 Simulation procedure

ANSYS was used for conducting numerical simulation. In considering simulation time, memory usage and convergence, an iterative solver (PowerSolver, PCG) was employed. For 3-D simulation of polymeric materials, solid 187 (element type) in ANSYS was selected for simulating thermo-responsive SME.

As aforementioned, volume fractions are very important parameters in this simulation. We choose a uniform meshing method in simulation. All single elements in the model have the same volume. Therefore, the volume fractions of different components can be easily obtained. In all simulation, more than 5000 elements were used in a representative 3-D unit ($1 \times 1 \times 1$), in which the distribution of inclusions was assumed to be random. Given this big number of elements, in most of cases the exact distribution of inclusions should have limited influence on the actual behavior.

Refer to Figure 4.1 for a representative 3-D unit. Since the simulation was limited to uniaxial tension or compression in current study, symmetry conditions on planes (x=0, y=0, and z=0), and displacement condition (u_z=0) on plane (z=0) were applied. In order to maintain uniform deformation, displacement coupling condition is applied, i.e., the same u_x for all nodes on plane (x=1), the same u_y for all nodes on plane (y=1), and the same u_z for all nodes on plane (z=1).

There are two parts in the simulation of a shape memory cycle. One is programming, and the other is recovery. Figure 4.3 shows the flowchart of the procedure.

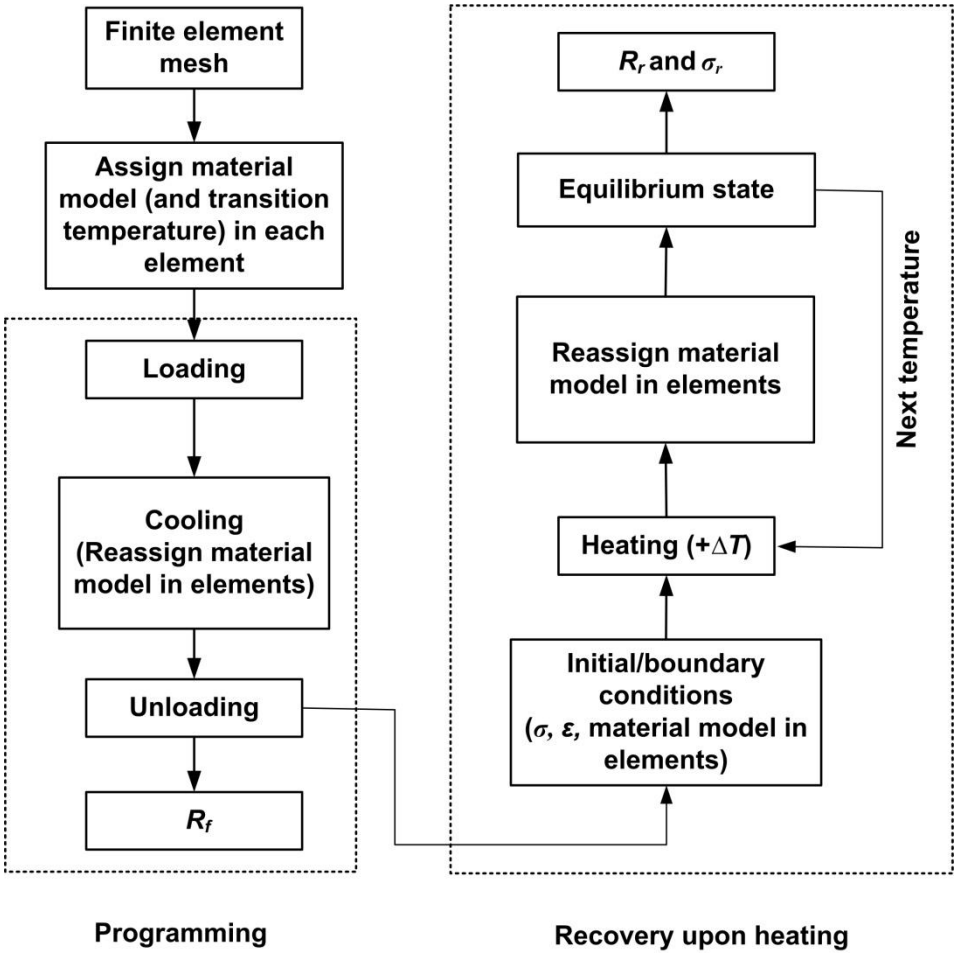

Figure 4.3 Flowchart of simulation procedure.

There might be many sub-steps in each simulation step to avoid computation problem. It is necessary to keep updating stress, strain and material model in each element in every simulation step/sub-step. Thermal expansion is not considered in currently study for simplicity.

(1) Programming

There are three sub-steps in programming, namely loading, cooling, and unloading. Before loading, we need to assign different material models to different elements according to programming temperature (Figure 4.3).

Loading – In the case of uniaxial tension/compression, in z-direction in Figure 4.1, a displacement load (u_z=ε_m) is applied on the top surface (z=1) of the 3-D unit. There might be up to 50 sub-loading steps before the required ε_m is reached.

Cooling – For simplicity, in current simulation, the relaxation of polymer molecular chains is not considered.

Upon cooling, soft transition inclusions gradually become hard ones corresponding to pre-assigned exact transition temperatures. Material models of inclusions are uploaded accordingly in each sub-cooling step until the prescribed cooling temperature is reached. The geometrical boundary condition at the top surface is always held.

Unloading – The initial condition for the unloading process is the stress and strain conditions after loading (and cooling, if applicable). In current study, unloading is only conducted at room temperature, which is well below the glass transition (or melting) temperatures, so that the material is in the glassy state. The constitutive relationship in

unloading is assumed to be linear elastic. During unloading, the top surface is assumed to be free from any constraint. R_f is calculated accordingly.

In this study, most of the programming processes are in uniaxial compression. The reason for this is twofold. One is to avoid brittle fracture or non-uniform deformation in uniaxial tension at low temperatures, and the other is that in the particular application presented in Chapter 6, the required loading for programming is in compression.

(2) Recovery

Upon heating, hard inclusions gradually become soft. The corresponding material model needs to be uploaded. The initial condition for recovery is mainly from the residual stress in the elastic matrix, which needs to be updated at each sub-step during simulation.

Depending on the type of shape recovery, the top surface may be set free from any constraint (free recovery) or the displacement in the top surface may be fixed (constrained recovery).

4.2 Simulation and optimization

Numerical simulation was conducted for PTM and DCM following above mentioned procedure. Optimization of the SME was also carried out.

4.2.1 PTM

The SME in BIOCOM DR, which is assumed to follow PTM, was simulated in the case of uniaxial compression. Since the deformation was small, a bilinear isotropic elasto-plastic model was used for the hard and soft parts.

The volume fractions of hard and soft parts were obtained from Eqns. (4.4) and (4.5) based on the DSC curve in Figure 3.7(a). Figure 4.4(a) plots f_t^s (volume fraction of soft part) as a function of temperature in heating, together with the DSC curve as a reference.

The materials properties as listed in Table 4.2 were estimated from uniaxial compression results. Two BIOCOM DR samples were uniaxially compressed to a strain of 10% at a strain rate of $0.001s^{-1}$ at 30°C and 80°C, respectively. Figure 4.4(b) compares the strain vs. stress curves obtained by the elasto-plastic model and experiments.

Table 4.2 Material properties for BIOCOM DR.

	E (MPa)	ν	σ_y (MPa)	E_h (MPa)
Hard part	70	0.35	5.6	50
Soft part	10	0.45	0.2	2

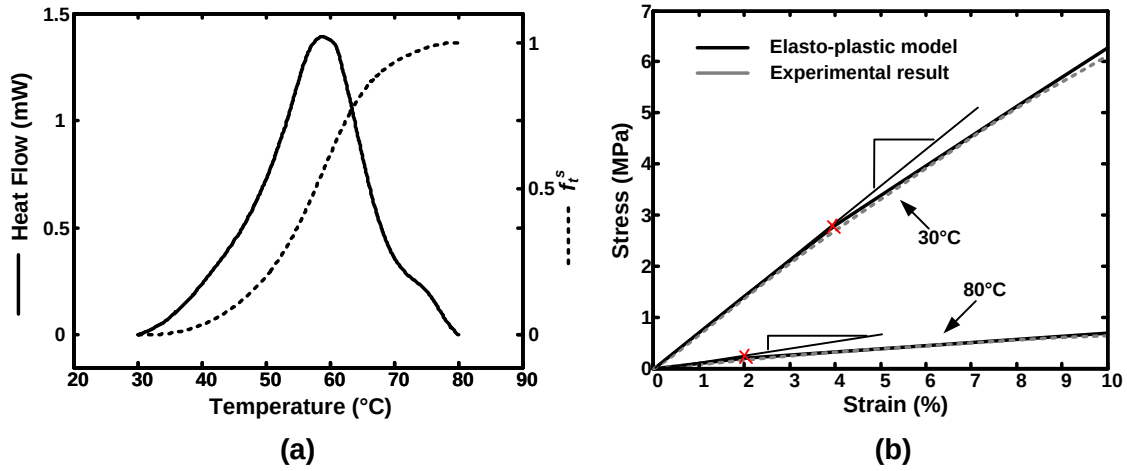

Figure 4.4 (a) DSC result and corresponding volume fraction curve of soft part; (b) Strain vs. stress curves of BIOCOM DR at 30°C and 80°C in uniaxial compression.

Rectangular BIOCOM DR samples (about $20\times20\times3$ mm^3) were compressed along its thickness direction (3 mm) to 10% strain at a rate of $0.001s^{-1}$ and different T_ps (within the

30°C-80°C melting transition range) using Instron 5569. They were unloaded after cooling back to room temperature (20°C). These programmed samples were reheated to their individual programming temperatures for 30 min. R_f and R_r were obtained in each samples.

A 3-D, 10-node tetrahedral element was used in simulation. As shown in Figure 4.5, the representative unit is a $1 \times 1 \times 1$ mm^3 cubic with 6400 elements and 9929 nodes.

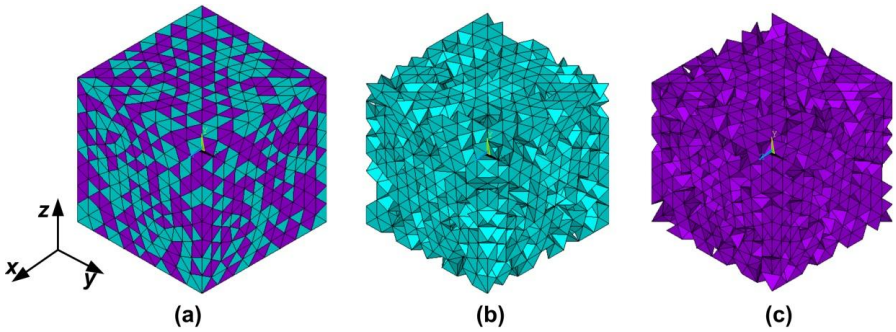

Figure 4.5 Finite element model at a particular temperature of 62°C ($f_t^s = f_t^h = 50\%$). (a) Entire model; (b) hard part; (c) soft part.

The simulation followed the actual experiment according to the procedure discussed in Section 4.1.3. Figure 4.6 shows the geometric change during programming and shape recovery in a particular case (T_p =62°C).

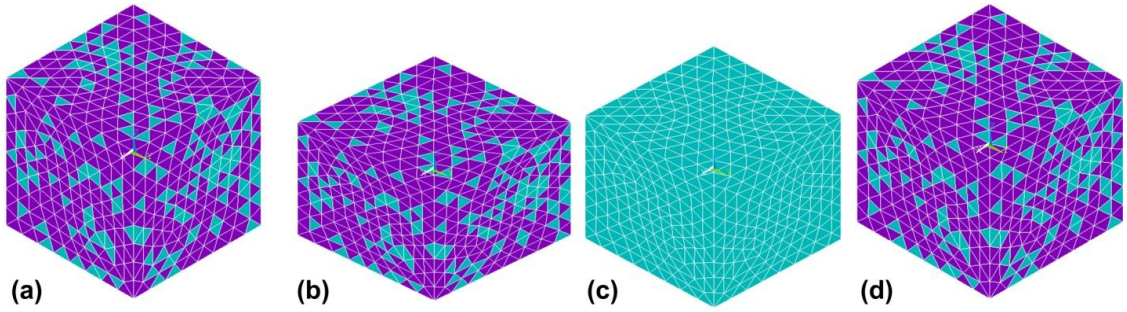

Figure 4.6 Simulated shape change. (a) Original shape at 62°C; (b) after compression at T_p (=62°C); (c) after programming (cooling to 20°C and then unloading); (d) after shape recovery at 62°C.

Figure 4.7(a) compares the R_f vs. T_p relationships obtained from experimental and simulation. Both curves reveal similar trend, i.e., R_f increases with the increase of T_p.

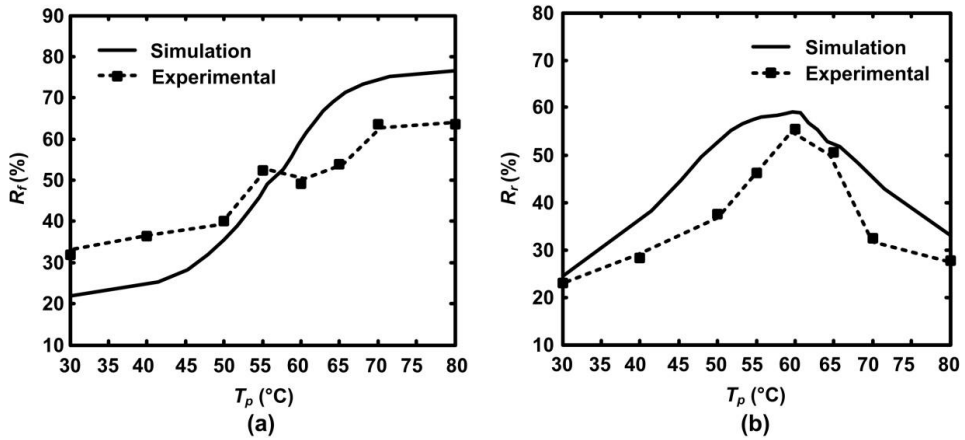

Figure 4.7 R_f and R_r of BIOCOM DR at different T_ps.

Figure 4.7(b) compares the R_r vs. T_p relationships of experiment and simulation. With the increases of T_p, R_r continuously increases before reaching about 60°C and then decreases continuously. Experimental results and simulation agree well, so that we may optimize Rr by means of numerical simulation, instead of conducting a series of actual experiments.

4.2.2 DCM

For DCM based SMMs, volume fractions of the elastic matrix and transition component are very important parameter in design a new SMM.

The SME in a silicone/wax SMH, which follows DCM, was simulated under uniaxial compression. Since silicone has good elasticity and serves as the elastic matrix in this SMH, an ideal elastic model was used for it. Wax serves as T_m-based transition inclusions in this SMH. An elasto-plastic model was used for soft and hard wax.

We investigated the influence of f_t on R_f, R_r and σ_r. The materials properties as listed in Table 4.3 were estimated from the experimental results of uniaxial compression on silicone and wax. Wax samples were compressed to 50% strain at a strain rate of $0.001s^{-1}$ and 22°C and 70°C, respectively, which are below and above its T_g. Silicone sample was compressed to 50% strain at a strain rate of $0.001s^{-1}$ and then unloading at the same strain rate. The strain vs. stress curves are plotted in Figure 4.8.

Table 4.3 Material properties for silicone/wax SMH.

		E (MPa)	v	σ_y (MPa)	E_h (MPa)
Silicone		2	0.45		
Wax	Soft	0.2	0.4	0.002	0.2
	Hard	20	0.35	2	0.15

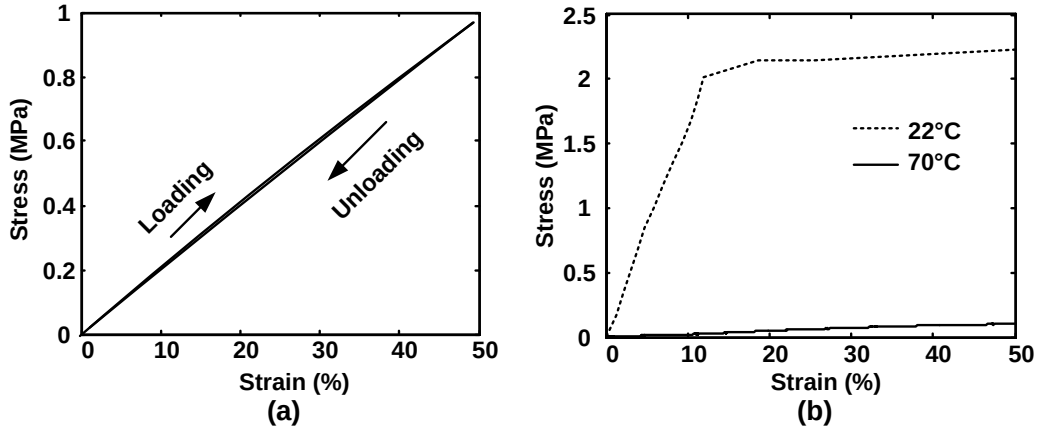

Figure 4.8 Strain vs. stress curves of (a) silicone and (b) wax.

A series silicone/wax SMH samples with different f_ts were prepared following a mixing, bubble removing, molding, and curing process, as described in details in [163]. These samples were uniaxial compressed to 20% strain at a strain rate of $0.001s^{-1}$ and 70°C.

Then, they were cooled back to 20°C and unloaded. Finally, they were reheated to 70°C for free recovery. R_f and R_r were in each sample.

Again a 3-D, 10-node tetrahedral element was used in simulation. As shown in Figure 4.9, the representative unit is a $1\times1\times1$ mm^3 cubic with 6400 elements and 9929 nodes. Simulation followed the procedure described in Section 4.1.3 and the actual experiments. R_f, R_r and σ_r were obtained.

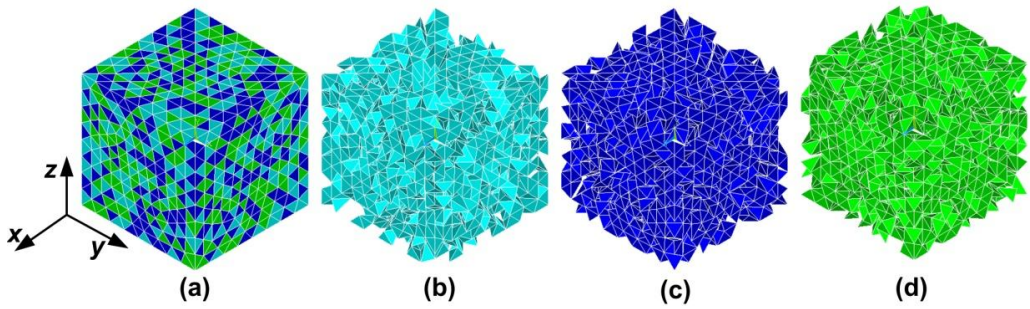

Figure 4.9 Finite element model with 50% silicone matrix, 25% soft wax, and 25% hard wax. (a) Entire model; (b) elastic network; (c) hard wax; (d) soft wax.

Figure 4.10(a) compares the relationships of R_f vs. f_t and R_r vs. f_t from experiment and simulation.

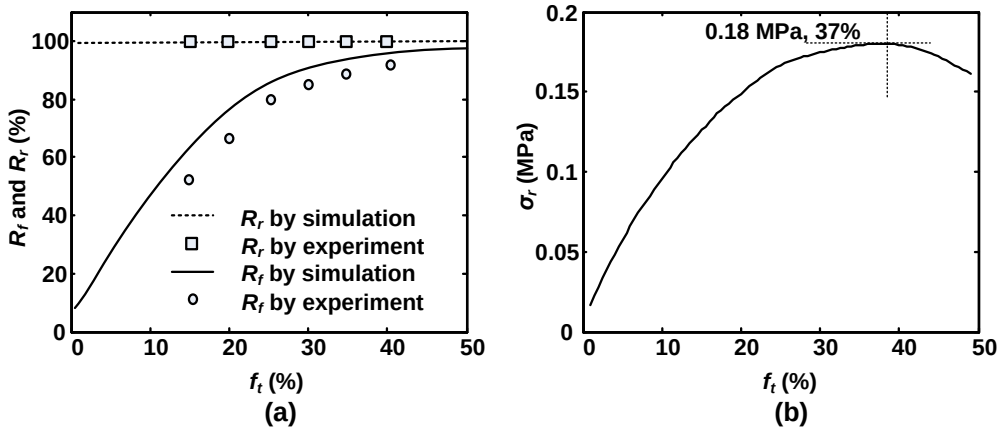

Figure 4.10 SME in silicone/wax SMH. (a) Effect of f_t on R_f and R_r; (b) effect of f_t on σ_r (simulation only).

It can be seen that R_f increases with the increase of f_t. R_r is always 100% in all samples. The simulation is in good agreement with the experimental results. Figure 4.10(b) plots the σ_r vs. f_t relationship by simulation. A peak value for σ_r is observed at f_t=37%.

4.2.3 Optimization of the SME

R_f, R_r and σ_r are important parameters in the characterization of shape memory feature. In general, higher R_f, R_r and σ_r are required. Hence, instead of by experiments, numerical simulation is a cost-effective approach for optimization of the SME.

As shown in Figure 4.7, it can be seen that programming at about 60°C results in high value of R_f and R_r simultaneously in BIOCOM DR. Figure 4.10 reveals that maximum σ_r is reached in a silicone/wax hybrid with about 37% wax (volume fraction).

Consider a T_g based dual-component SMP, (f_e, f_t), (E_e, E_t^s, E_t^h), and (T_p, T_h) are three groups of parameter to manipulate for optimized performance. Here, E_e, E_t^s and E_t^h are the Young's modulus of elastic component, rubbery state and glassy state of transition component, respectively. T_h is the heating temperature in recovery process.

In order to simplify the situations, we assume that $E_e = E_t^h$ in this simulation. For a traditional shape memory cycle, a polymeric SMM is programmed at high temperatures, so that we assume T_p=T_g. We studied the influence of (f_e, f_t), (E_e/E_t^s), and T_h in a T_g based dual-component SMP.

An elastic model was used for the elastic component and rubbery state of the transition component. An elasto-plastic model was used for the glassy state of the transition component. Volume fractions of individual components were determined by Eqn. (4.1).

Evolution of soft/hard inclusions was obtained from Eqns. (4.2) and (4.3) (assumed T_g=90°C, and A=10°C). Table 4.4 lists the materials properties.

Table 4.4 Material properties for a dual-component SMP.

		E (MPa)	ν	σ_y (MPa)	E_h (MPa)
Elastic component		20	0.45		
Transition component	Rubbery state	From 0.02 to 20	0.45		
	Glassy state	20	0.33	2	2

The same element as above in cases was used. The representative unit is a $1\times1\times1$ mm^3 cubic with 6400 elements and 9929 nodes (Figure 4.11). Simulation followed the procedure described in Section 4.1.3.

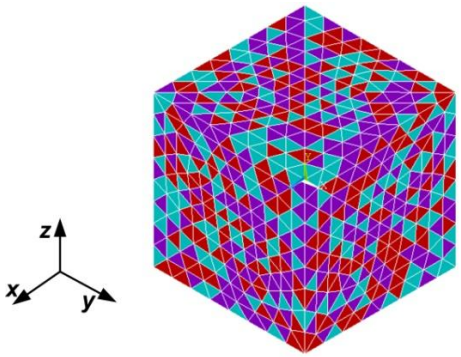

Figure 4.11 Finite element model. Blue area is elastic component; red area is glassy state of transition component; and purple area is rubbery state of transition component.

As higher R_f is required for a polymeric SMM, we therefore simulated the effect of modulus E_e/E_t^s and f_t on R_f. This is useful for design of a DCM based SMM. According to optimized R_f, we can select the fractions of elastic and transition components.

Samples with different f_t were uniaxially compressed to 20% strain at a rate of $0.001s^{-1}$ and T_p (90°C). Subsequently, they were unloaded after cooling back to low temperature (20°C).

Figure 4.12 reveals the R_f as a function of f_t and log (E_e/E_t^s) by simulation. It can be seen that given a fixed E_e/E_t^s, R_f increases as f_t increases; given a fixed f_t, R_f increases as E_e/E_t^s increases. In general, the modulus of a polymer in the glassy state is about 1000 times of that in the rubbery state.

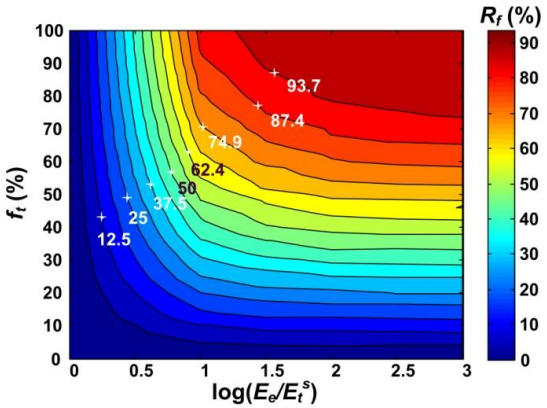

Figure 4.12 Contour of R_f as a function of f_t and log (E_e/E_t^s).

It also can be seen that a higher shape fixity ratio is difficult to achieve, if log(E_e/E_t^s) is below 1, as the difference in modulus is small. The pre-strain produced at high programming temperatures cannot be effectively stored in the system after programming. The modulus at low temperatures is not high enough to restrict the elastic recovery of the elastic matrix.

According to Figure 4.12, we fixed f_t as 70% in the next step of simulation to study the effects of modulus and T_h on R_r and σ_r. Free recovery and constrained recovery were simulated following the procedure as described in Section 4.1.3.

Figure 4.13 presents R_r and σ_r as a function of T_h and log (E_e/E_t^S). It can be seen that given a fixed E_e/E_t^S, R_r increases with the increase of T_h. R_r is seemingly more sensitive to the variation of T_h than that in E_e/E_t^S. σ_r increases with the increase of T_h before a peak value at temperature of T_p; then starts to decrease, which is the TME. Given a particular T_h, σ_r decreases with the increase of E_e/E_t^S.

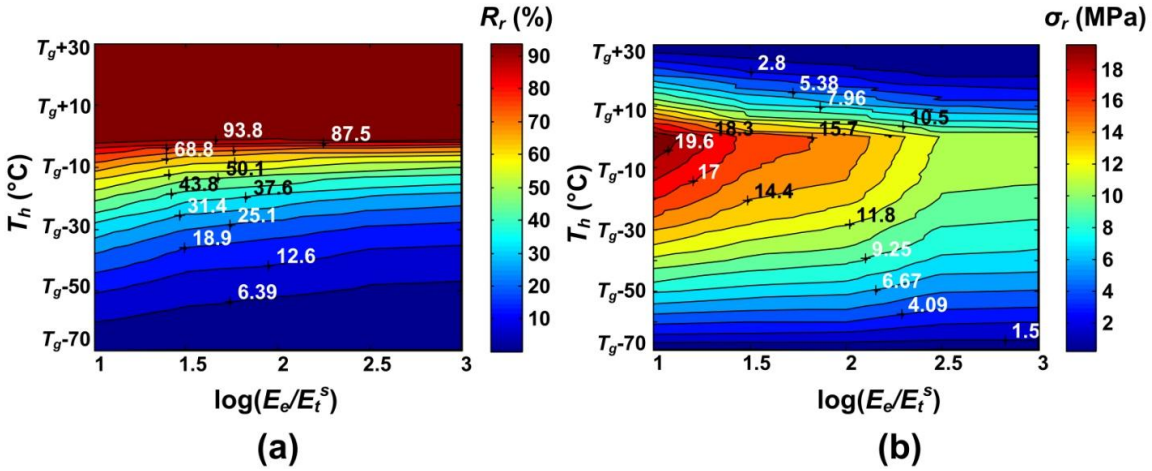

Figure 4.13 Contour of R_r and σ_r as a function of T_h and log (E_e/E_t^S).

4.3 Summary

In this chapter, a generic 3-D model is developed to simulate the shape memory behavior in polymeric SMMs. Simulation of PTM and DCM based polymeric SMM agree well with the experimental results. This model is also applicable for optimization of the SME.

Chapter 5 Thermo-/chemo-responsive SME in PMMA

Traditionally, PMMA is not well known for its SME, although its shape recovery ability induced by either heating or solvent absorption (limited to small strain) has actually been reported in the literature [171-173]. Our recent experiments revealed that the recoverable strain in PMMA (in free recovery) can be over 100% in uniaxial tension and over 50% in uniaxial compression, while the maximum actuation stress in constrained recovery in uniaxial tension can be over 2 MPa after optimization [97]. This chapter gives a detailed study on the SME in PMMA experimentally and analytically. In experimental investigation, the focus is on the chemo-responsive SME, while in simulation they are advanced features in PMMA (i.e., RP-SME and TME).

5.1 Experimental investigation

From the molecular structure aspect, PMMA is a typical physically cross-linked polymer. As such, according to our classification, the SME in PMMA belongs to DSM, which can be triggered by thermo- and chemo-stimuli. The SME in PMMA is associated with "quasi-elastic" energy storage and release during programming and recovery, respectively. Highly elastic polymeric networks, which are disordered, randomly coiled, and highly entangled molecular chains, have excellent capability to store elastic energy as the driving force for recovery.

PMMA (MC® cast sheet and MC® extruded rod) used in this study was bought from Ying Kwang Acrylic, Singapore. The PMMA used in the experiments is highly physical cross-linked, which is cell cast acrylic. The molecular weight (M_w) of it is in the order of 10^6.

The average molecular weight ($\overline{M_w}$) is about 2.5~3×10^6 g/mol. Before testing, all samples were annealed at 120°C for 1 hour to release any pre-strain/stress. DSC Q200 machine from TA Instruments was used for DSC test. All samples were thermally cycled between 20°C and 200°C at a speed of 10°C/min. As we can see, the T_g of this PMMA is about 115°C (Figure 5.1, only 80°C-200°C part is shown).

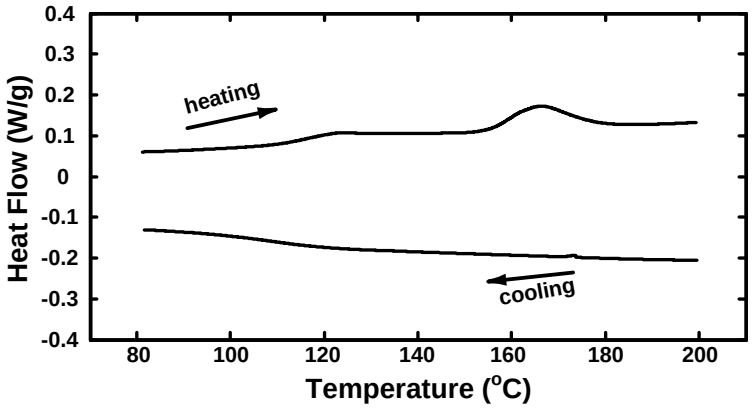

Figure 5.1 DSC result of PMMA within 80°C and 200°C range.

5.1.1 Thermally induced shape recovery in PMMA

Figure 5.2(b) reveals typical shape memory behavior in a 1 mm thick PMMA sample in uniaxial tension. The original PMMA sample in a dog-bone shape was stretched to 100% strain at a strain rate of 0.001s^{-1} and 120°C using Instron 5569. Dimensions of dog-bone shaped sample are shown in Figure 5.2(a). Full shape recovery was observed when the pre-stretched sample was reheated to 120℃. It should be pointed out that the PMMA sample is always highly transparent Figure 5.2(b).

Figure 5.3 reveals the shape recovery phenomenon in PMMA after micro-scale local deformation at room temperature (about 20°C). A micro-hardness tester (CSM

instruments) was used to make indentations atop 1 mm thick PMMA using standard Vickers and spherical indenters. The PMMA samples were indented to a maximum load of 100 mN at a speed of 5 mN/s with a 10 s holding stage between loading and unloading. After indentation, the sample was heated to 120°C for 10 mins. The surface morphology of indented samples before and after reheating was scanned using a confocal optical surface imaging profiler. Figure 5.3 reveals that PMMA has excellent SME at micro-scale.

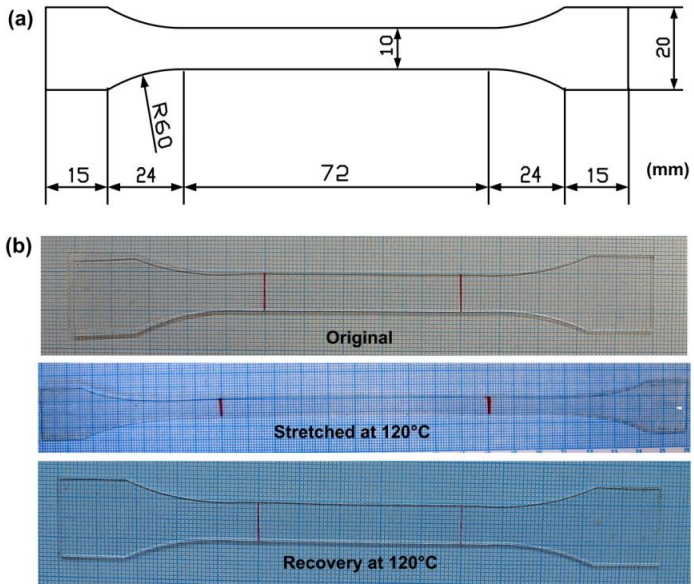

Figure 5.2 Shape recovery in PMMA (programmed by uniaxial tension).

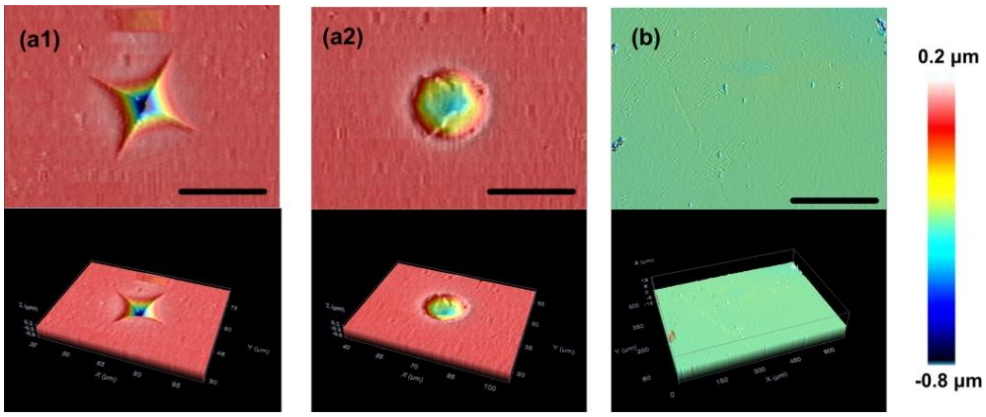

Figure 5.3 Shape recovery in micro-indented PMMA. (a) Indented at room temperature; (b) recovery after heating to 120°C. Scale bar: 20 µm.

A systematical experimental investigation was followed to reveal the detailed shape memory phenomenon in PMMA.

5.1.1.1 Effects of T_p on R_f

Generally speaking, in order to fully utilize the SME, R_f should be as high as possible. For the DSM based SMMs, R_f mainly depends on T_p. The relationship between R_f and T_p is reported in this section.

3 mm thick PMMA samples with dimensions of 20×20 mm^2 were heated to T_p and then uniaxially compressed along the thickness direction by 2.5% strain or 25% strain at a strain rate of 0.001s^{-1} using Instron 5569. After cooled back to room temperature, the samples were unloaded.

Typical stress vs. strain curves in programming are plotted in Figure 5.4(a). R_f is plotted against T_p in Figure 5.4(b). It is logical that, as T_p increases, after programming the residual strain and consequent R_f increase.

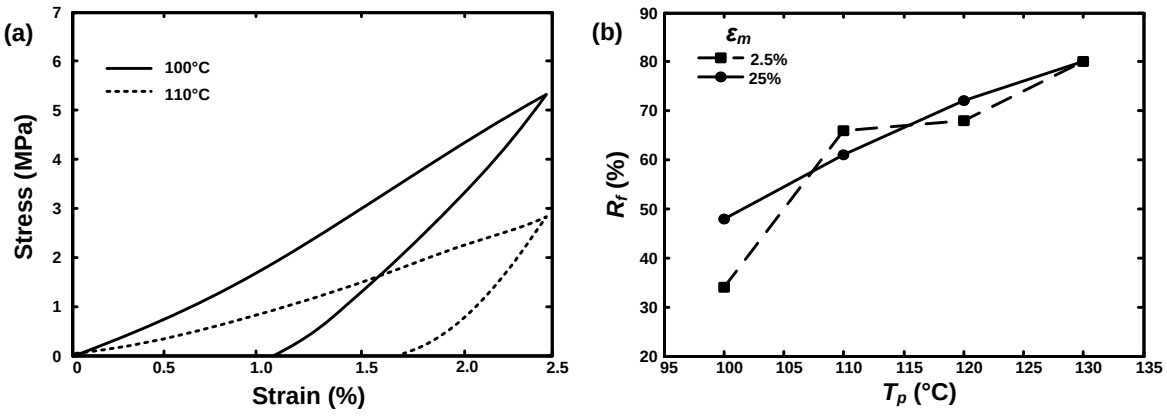

Figure 5.4 (a) Typical stress vs. strain curves (uniaxial compression). (b) R_f of PMMA at 2.5% and 25% compression strains at different T_ps.

5.1.1.2 Effects of programming parameters on R_r

In addition to R_f, R_r is another very important parameter to characterize the SME, which is more sensitive to the programming parameters. The effects of T_p, ε_m, and $\dot{\varepsilon}$ on R_r are reported in this section.

3 mm thick dog-bone shaped PMMA samples (Figure 5.5a) were heated to T_p and then uniaxially stretched using Instron 5569. The samples were stretched to 50%, 100% and 150% strains at different strain rates, followed by cooling back to room temperature and then unloading. A typical stress vs. strain curve is plotted in Figure 5.5(b). Subsequently, these samples were reheated to different temperatures in an oven. Shape change upon heating was measured.

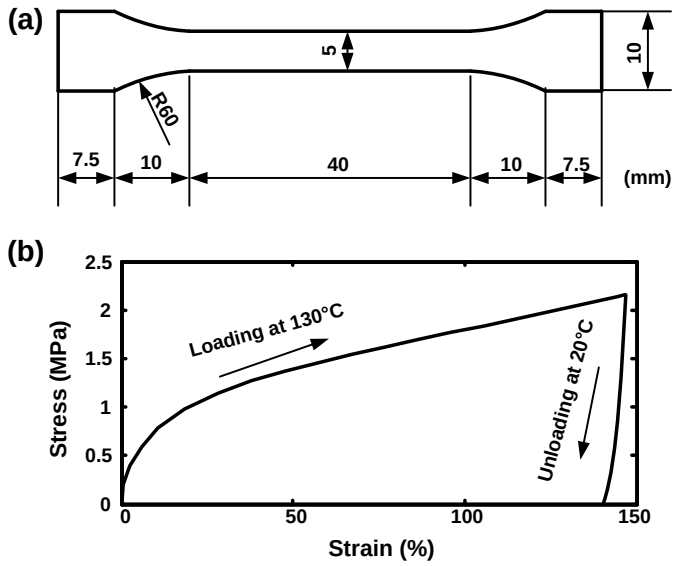

Figure 5.5 (a) Dimensions of dog-bone shaped sample. (b) Typical stress vs. strain curve (uniaxial tension at strain rate of $0.1s^{-1}$).

Figure 5.6(a) plots R_r of samples stretched at different T_ps to 150% strain at a strain rate of $0.0005s^{-1}$ upon heating. Figure 5.6(b) is a zoom-in view of the glass transition range

(80°C-140°C) according to the DSC result (Figure 5.1). As we can see, shape recovery occurs slightly earlier in the sample pre-stretched at low T_p. As we can see, R_r in samples programmed at 110°C and 130°C approaches 100%, while that at 150°C and 170°C is less. This is because 150°C is about the melting start temperature of this PMMA.

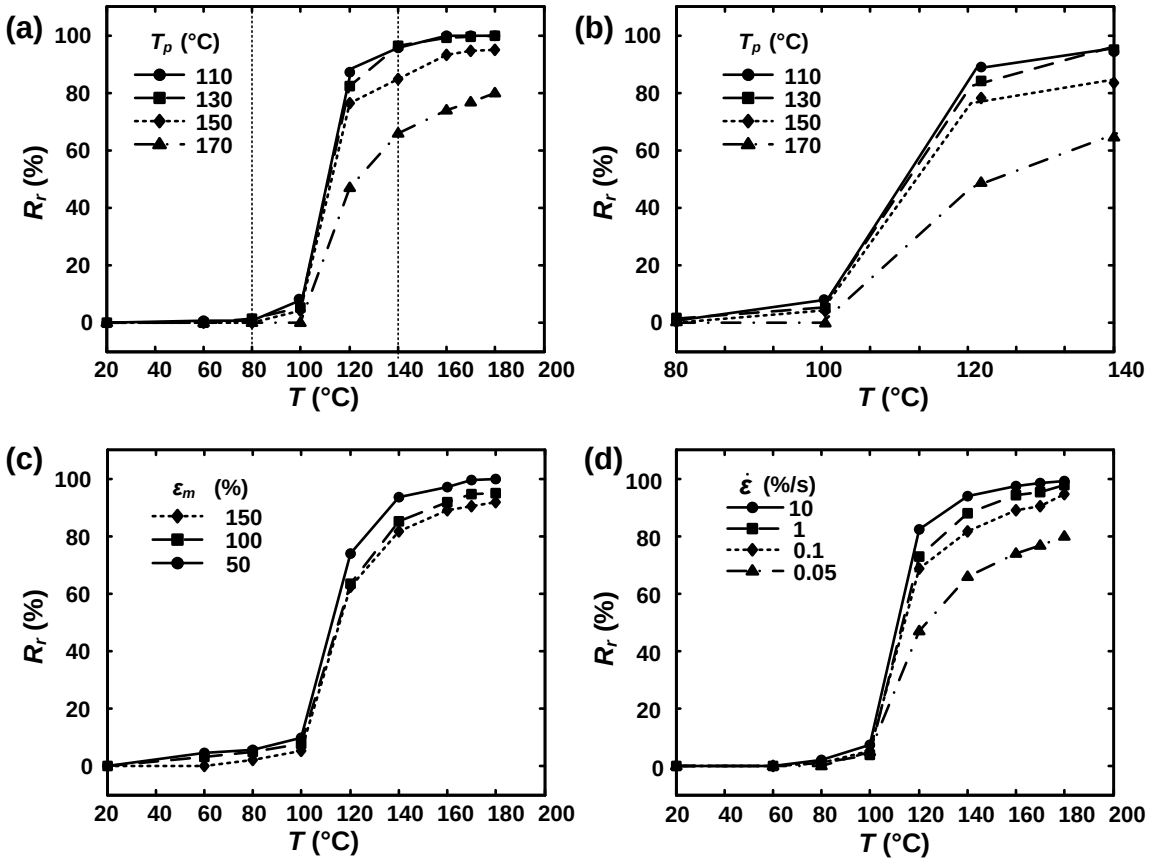

Figure 5.6 Effects of T_p, ε_m, and $\dot{\varepsilon}$ on R_r.

Figure 5.6(c) plots R_r of samples stretched to different strains at a same T_p of 170°C and strain rate ($0.001s^{-1}$) upon heating. Figure 5.6(d) plots R_r of samples stretched at different strain rates at a constant T_p of 170°C and programming strain of 150% upon heating. According to the DSC result (Figure 5.1), PMMA at 170°C is within its melting range. Therefore, flow of chains may happen, which leads to some permanent deformation. High

ε_m and low $\dot{\varepsilon}$ may lead to more permanent deformation, so that R_r decreases as ε_m increases and $\dot{\varepsilon}$ decreases.

5.1.2 Chemically induced shape recovery in PMMA

PMMA is a kind of amorphous glassy polymer. From thermodynamic aspect, in the stable state, PMMA appears as disordered, randomly coiled and highly entangled molecular chains as illustrated in Figure 5.7(a). Upon stretching at high temperatures, these chains rearrange and become unstable (Figure 5.7b). The rearranged chains store elastic energy locally. Subsequently, after cooling back to room temperature, limited instant recovery happens after unloading (Figure 5.7c). Upon immersing into a right solvent, molecular chains are softened. During softening from outer layer inward, the stored elastic energy is released by means of recoiling and entangling of the molecular chains, which causes a compressive stress within the softened area (Figure 5.7d). Upon further softening, more molecular chains are softened and eventually the PMMA may fully recover its original shape (Figure 5.7e).

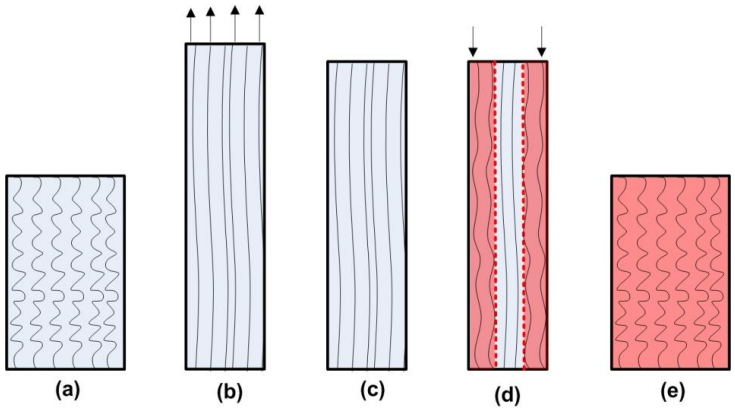

Figure 5.7 Illustration of underlying SME mechanism in PMMA. (a) Original amorphous PMMA; (b) uniaxial stretched at high temperatures; (c) cooling and unloading; (d) outer layer softened in a chemical stimulus; (e) final shape after recovery.

5.1.2.1 Softening and plasticization of PMMA in ethanol

A clear boundary can be observed during penetration of ethanol into PMMA. 1 mm thick PMMA sheets with a size of 15×5 mm^2 without any pre-straining were immersed into room temperature ethanol (95% concentration). Figure 5.8(a) reveals the boundary between outer swollen zone and inner glassy core (without ethanol) after 28 days in ethanol.

By measuring the dimensions of the swollen zone and glassy core, the ethanol penetration process can be monitored in real-time. During ethanol penetration, the original sample dimension h_0 is expanded to h, and the size of the glassy core (h_c) shrinks gradually until ethanol fully penetrates into PMMA (Figure 5.8b). According to the evolution of h_c against time t, the velocity of ethanol penetration boundary v_p can be expressed as $v_p = -dh_c/2dt$.

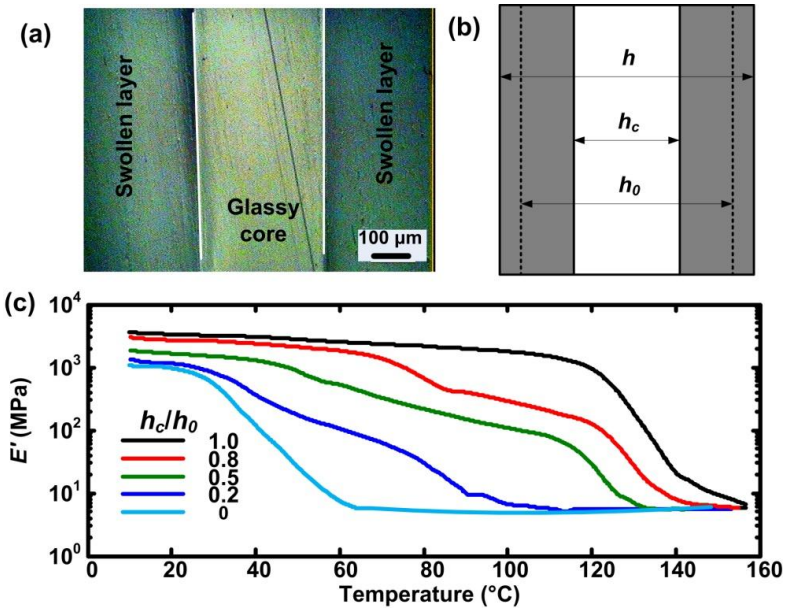

Figure 5.8 (a) Image of ethanol penetration in PMMA. (b) Model of ethanol penetration in PMMA. (c) Storage modulus from DMA test.

In the swollen zone, ethanol weakens the bonding in PMMA molecular chains, and thus the mobility of the molecular chains is enhanced and T_g is depressed. Consequently, the modulus decreases.

Different 1 mm thick PMMA samples were immersed into room temperature ethanol for different periods of time. Softening in these samples was verified by a series of DMA tests, in which samples with different h_c/h_0 were tested in three-point bending mode from 10°C to 150°C at a heating rate of 5°C/min. A static force of 11 mN, dynamic force of 10 mN, and frequency of 1 Hz were selected.

The storage modulus E' is plotted in Figure 5.8(c). As we can see, both the onset T_g and E' (at 20°C) are depressed from 110°C to 25°C, and from 3.5 GPa to 1.2 GPa, respectively.

We can roughly see two softening events. One occurs at about T_g in dry PMMA, and the other is at low temperatures. For dry PMMA, only high temperature one is observed. If ethanol is fully penetrated into PMMA, we can only see the low temperature one, while the high temperature one disappears. Similar phenomenon has been found in poly(vinyl alcohol) upon immersing into DMF [110].

Upon immersing into ethanol, h_c/h_0 was measured by tracking the boundary movement using an optical microscope.

Figure 5.9 plots the evolution of h_c/h_0 against time. As we can see, it is virtually a linear function. This reveals that v_p is more a less a constant (0.71 μm/hr) in PMMA without pre-straining. After full penetration of ethanol in PMMA, h/h_0 is about 1.2.

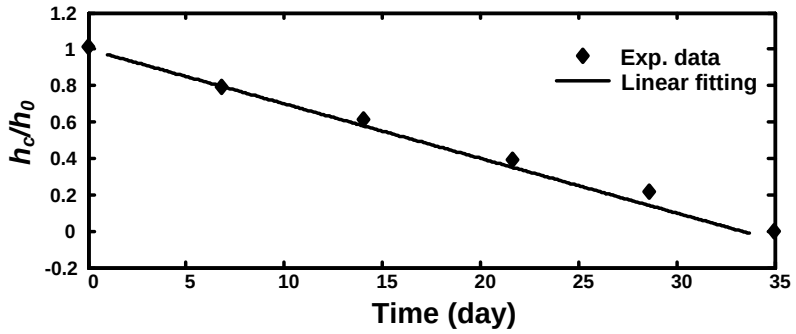

Figure 5.9 The h_c/h_0 vs. time relationship.

5.1.2.2 Shape recovery in pre-strained PMMA

In above section, softening of PMMA upon immersion into room temperature ethanol was investigated. All samples used there were without pre-straining. Here, shape recovery in pre-strained PMMA samples upon immersion into room temperature ethanol is reported.

(1) Shape recovery in pre-stretched PMMA

Three pieces of 3 mm thick dog-bone shaped PMMA samples (Figure 5.5a) were stretched to 50%, 100% and 150% strains at a strain rate of $0.001s^{-1}$ and 120°C, respectively, followed by cooling back to room temperature and then unloading. After programming, the rectangular central parts were cut out of the dog-bone shaped samples. Shape recovery phenomenon was monitored upon immersing these samples into room temperature ethanol.

Similar to that in PMMA sample without pre-straining, there is also a clear boundary showing ethanol penetration in pre-stretched PMMA upon immersing into room temperature ethanol (Figure 5.10a). Figure 5.10(b-d) shows some typical phenomena upon further immersing into ethanol, which correspond to 50%, 100% and 150% pre-strained samples, respectively.

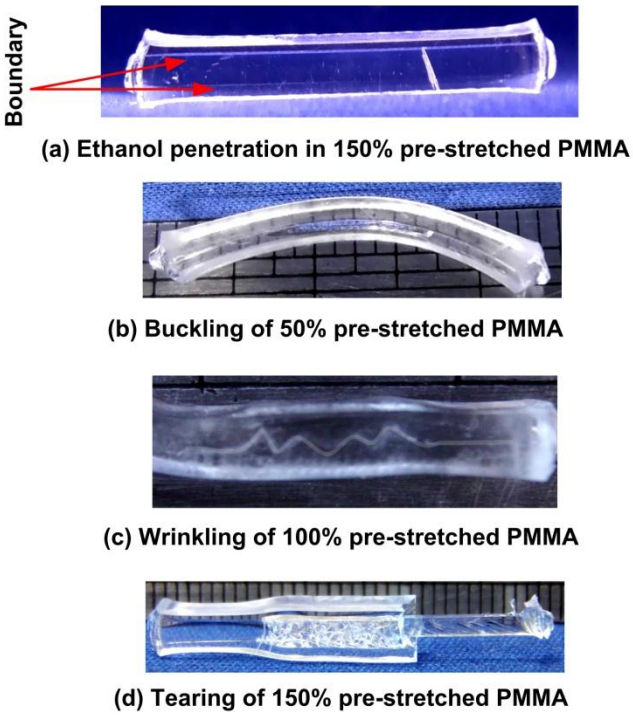

Figure 5.10 Shape recovery in pre-stretched PMMA after immersion into room temperature ethanol. (a) After 15 days in ethanol; (b)-(d) after 30 days in ethanol.

Buckling — Figure 5.11 illustrates ethanol penetration in a pre-stretched PMMA and the buckling phenomenon. The buckling condition for a pre-stretched PMMA sample in ethanol can be derived from Euler buckling formula [174, 175]. Different from the classical configurations of Euler columns, in which the compressive force/stress is applied at the ends, here, the compression stress (σ) is internally applied and is roughly a function of ε_r. Despite this difference, the buckling condition is essentially the same, i.e., [174, 175]

$$P = \frac{\pi^2 EI}{L^2} \tag{5.1}$$

where L should be the effective length of the sample, EI is the flexural rigidity,

$$EI = E_1 \frac{b_c a_c^3}{12} + E_2 \left(\frac{b a^3}{12} - \frac{b_c a_c^3}{12} \right) \tag{5.2}$$

and P is the total compressive force,

$$P = \sigma \left(ab - a_c b_c \right) = E_2 \varepsilon_r \left(ab - a_c b_c \right) \tag{5.3}$$

where E_1 and E_2 are the Young's moduli of inner hard core and outer soft layer, respectively. Refer to Figure 5.11(a) bottom for cross-section dimensions.

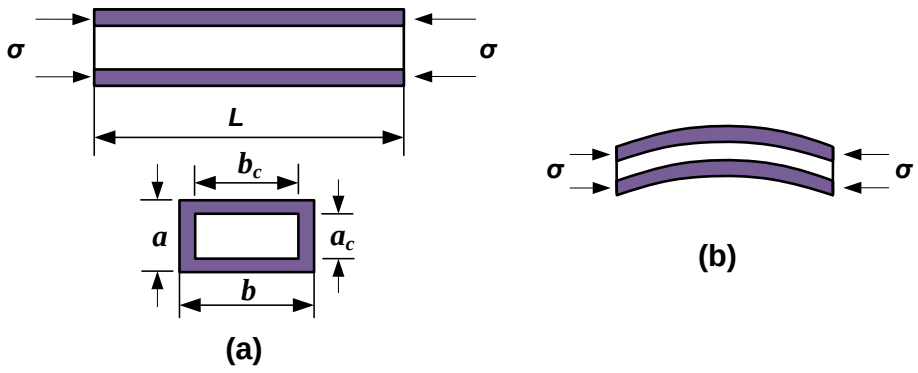

Figure 5.11 (a) Illustration of stretched PMMA in ethanol and (b) buckling. Shadowed area is soft layer; white area is glassy core.

Here, a-a_c=b-b_c=$2\nu_p t$. Based on Eqns. (5.1)-(5.3), the critical buckling condition can be theoretically predicted.

Wrinkling — Figure 5.12(a) illustrates the wrinkling phenomenon in a pre-stretched PMMA in ethanol. It can be seen that thin glassy core (thickness: h_c, modulus: E_1 and Poisson's ratio: ν_1) is covered with relatively thick outer soft layer (thickness: h_s, modulus: E_2 and Poisson's ratio: ν_2).

If the compressive stress, σ, is over a critical value, wrinkling (another type of buckling) occurs. Wrinkling of an elastic film atop a soft substrate has been extensively studied

before (will be discussed in Section 6.1.2) [176-178]. As shown in Figure 5.10(c), this kind of wrinkling belongs to the shallow mode [178]. For this kind of sandwich structure (soft outer layer and stiff core), the critical stress for wrinkling is a function of geometry and materials properties, which can be expressed as, [176-178]

$$\sigma_c \propto \frac{h_c}{h_s}\left(3\frac{E_2}{1-\nu_2{}^2}\right)^{1/3}\left(\frac{E_1}{1-\nu_1{}^2}\right)^{2/3} \tag{5.4}$$

Tearing — Figure 5.12(b) illustrates the tearing phenomenon in a pre-stretched PMMA in ethanol. Tearing occurs when the compressive stress is higher than the bonding stress between the soft layer and inner glassy core.

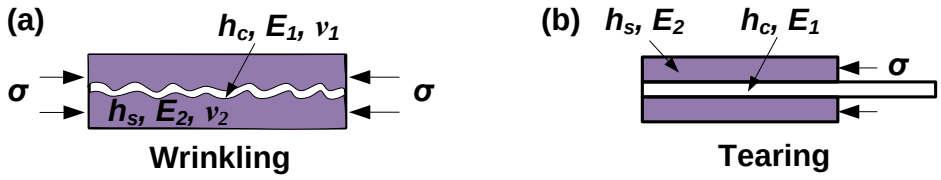

Figure 5.12 Illustration of wrinkling and tearing of PMMA immersed in ethanol.

When ethanol fully penetrates into PMMA, all residual strain/stress is released.

(2) Shape recovery in pre-compressed PMMA

Figure 5.13 illustrates the shape recovery process in a pre-compressed PMMA sample upon immersing into room temperature ethanol. More precisely speaking, edge areas should absorb more ethanol than the other parts, and thus shape recovery is faster at these edges, which results in concave faces during ethanol penetration.

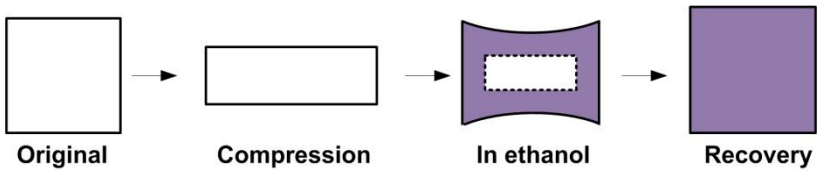

Figure 5.13 Shape recovery in compressed PMMA in ethanol. Shadowed area is soft layer; white area is glassy core.

When ethanol fully penetrates into PMMA, all residual strain/stress is released.

5.1.2.3 Effects of programming parameters on chemo-responsive SME

As aforementioned, thermo-responsive SME in PMMA is related to the programming parameters (ε_m, $\dot{\varepsilon}$ and T_p). Similarly, chemo-responsive SME in PMMA is also related to ε_m, $\dot{\varepsilon}$ and T_p as shown in Figure 5.14. It can be seen that R_r reaches the maximum in the sample deformed at 130°C (Figure 5.14a); R_r increases as ε_m increases at constant $\dot{\varepsilon}$ and T_p (Figure 5.14b); and R_r increases as $\dot{\varepsilon}$ increases at constant T_p and ε_m (Figure 5.14c).

In the case of deformation at temperatures lower than T_g, especially when ε_m is large, molecular chains may break, which leads to lower R_r; programming at temperatures much higher than T_g, causes easy slipping in intermolecular chains, which also leads to lower R_r; deformation at round T_g, is ideal for disentangling in molecular chains, which leads to higher R_r.

At the same $\dot{\varepsilon}$ and T_p, lower ε_m causes lower R_r for ethanol induced shape recovery in PMMA. Since the driving force for shape recovery depends on the degree of disentanglement in molecular chains, lower ε_m means lower degree of disentanglement, which induces a lower shape recovery driving force.

At the same T_p and ε_m, lower $\dot{\varepsilon}$ results in lower R_r, since lower $\dot{\varepsilon}$ means a longer molecular chain relaxation time, which may lead to slipping of intermolecular chains. Due to slipping within intermolecular chains, lower R_r is found after shape recovery.

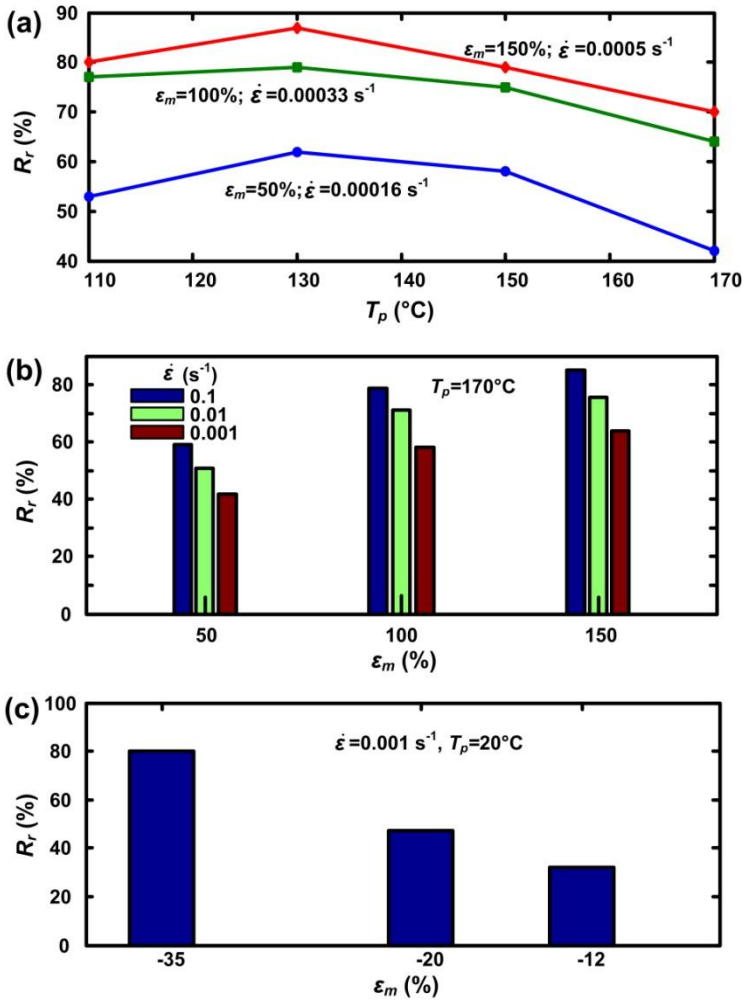

Figure 5.14 Relationships among R_r and ε_m, $\dot{\varepsilon}$ and T_p.

5.1.2.4 Pre-straining enhanced penetration (PSEP)

In addition to investigating the influence of programming parameters on shape recovery in pre-strained PMMA, we studied the influence of pre-strain on v_p. In this section, the pre-strain is mean for the residual strain after programming.

It has been reported that transportation of alcohols in strain/stress-free PMMA obeys case II theory (i.e., a swelling dominated diffusion process) [179-186]. Peterlin has proposed a physical model for this phenomenon [187]. It was reported that the swelling behavior in PMMA is a rearrangement process of molecular chains under osmotic stress (π) [188]. For a certain solvent/polymer system, ideally osmotic stress should be a constant. Thomas and Windle proposed that swelling behavior of PMMA in alcohols without pre-strain/stress is dominated by time-dependent mechanical deformation in response to π [188, 189].

Later on, alcohol absorption in pre-strained PMMA was qualitatively studied and the strong influence of pre-deformation on case II diffusion behavior was observed [190]. However, there is still seemingly a lack of a clear physical model to quantitatively describe the effect of deformation (pre-strain) on v_p till today.

Here, we extend Peterlin's model by means of taking into account the influence of pre-strain. The influence of ε_r on v_p is the focus in this study. We define the influence of pre-strain on ethanol transportation in PMMA as the PSEP effect. Based on this effect, a novel surface patterning method is proposed in Section 6.2.

In Figure 5.15(a), the profile of ethanol transportation and ethanol concentration over the cross-section of a piece of PMMA is sketched. Figure 5.15(c) shows the image of a sharp ethanol transportation front in PMMA.

Case II diffusion is characterized by a sharp penetration front with a constant v_p and a constant concentration (c_{eq}) in the swollen zone [186-189]. After an immersion time of t in ethanol, the swollen part with a thickness of $h_p(t)$ is separated from the glassy core [with a thickness of $h_c(t)$]. Consequently, the original PMMA thickness (h_0) expands to $h(t)$.

According to Peterlin's model [188], there is a thin element (also known as precursor, with a thickness of Δh) ahead of the sharp penetration front, which will swell in the next time step Δt. The swollen part (h_p) has a constant ethanol concentration of c_{eq}. The theoretical value of v_p can be expressed as,

$$v_p = \frac{h_0 - h_c(t)}{2t} = \frac{\Delta h}{\Delta t} \tag{5.5}$$

For case II diffusion, the diffusion speed of solvent is much higher than the relaxation speed of molecular chains. Therefore, Δh is related to the concentration dependent diffusion process, namely Fickian diffusion; and Δt is related to molecular rearrangement of the thin element. According to Fickian diffusion theory, solvent concentration (c) in the thin element may be expressed as $c = c_{eq} \exp\left[-M(h - h_c(t))\right]$, on the condition that $h_c(t) \le h \le h_c(t) + \Delta h$, where M is a constant (related to the diffusion coefficient and diffusion active energy, etc). Δh can be obtained according to $c_{eq} \exp(-M\Delta h) = 0$. Hence,

$$\Delta h = -\ln(c_{eq}) / M \tag{5.6}$$

Figure 5.15(b) is a sketch of the thin element (precursor) under osmotic stress and recovery stress.

As aforementioned, ethanol softens PMMA, so that molecular chains rearrange and relax under osmotic stress and recovery stress. The thin element with an initial thickness of Δh becomes Δh_{eq} in a small time step of Δt after the equilibrium state is reached. In the equilibrium state, the strain in the thin element [$\varepsilon_{eq} = \left(\Delta h_{eq} - \Delta h\right) \big/ \Delta h$] is a constant. Based

on a simple viscosity law [188], $\varepsilon_{eq}/\Delta t = (\pi + \sigma)/\eta$, where η is the viscosity of the swollen molecular chains, one has,

$$\Delta t = \varepsilon_{eq}\eta / (\pi + \sigma) \tag{5.7}$$

Substituting Eqns. (5.7) and (5.6) into Eqn. (5.5), v_p can be expressed as a function of σ or ε_r as,

$$v_p = k\pi + k\sigma = k\pi - kE\varepsilon_r, \tag{5.8}$$

where $k = -\ln(c_{eq})/M\varepsilon_{eq}\eta$ is a constant, and depends on the solvent diffusion coefficient and active energy in a particular polymer, viscosity of the unswollen and swollen polymer, and temperature, etc.

3 mm thick dog-bone shaped PMMA samples (refer to Figure 5.5a) were pre-stretched to different strain at different strain rates and/or temperatures. Then it was cooled back to 20°C and unloaded. ε_rs along length and thickness directions were measured. The rectangular central part was cut out of the dog-bone shaped samples. This rectangular sample was immersed into room temperature ethanol. v_p was obtained by monitoring of the ethanol penetration front along thickness or length directions.

Figure 5.15(d) shows v_p as a function of pre-strain, strain rates and temperature. It is clear that as a fixed strain rate and temperature, v_p is about linear function of pre-strain (ε_r). Furthermore, we may conclude that $k\pi$ depends on the programming temperature, and kE depends on both programming temperature and strain rate. In that programming temperature is a constant, $k\pi$ is a constant, but kE increases with strain rate.

By the way, after full penetration of room temperature ethanol in PMMA (with or without pre-strain), c_{eq} is a constant (about 30%).

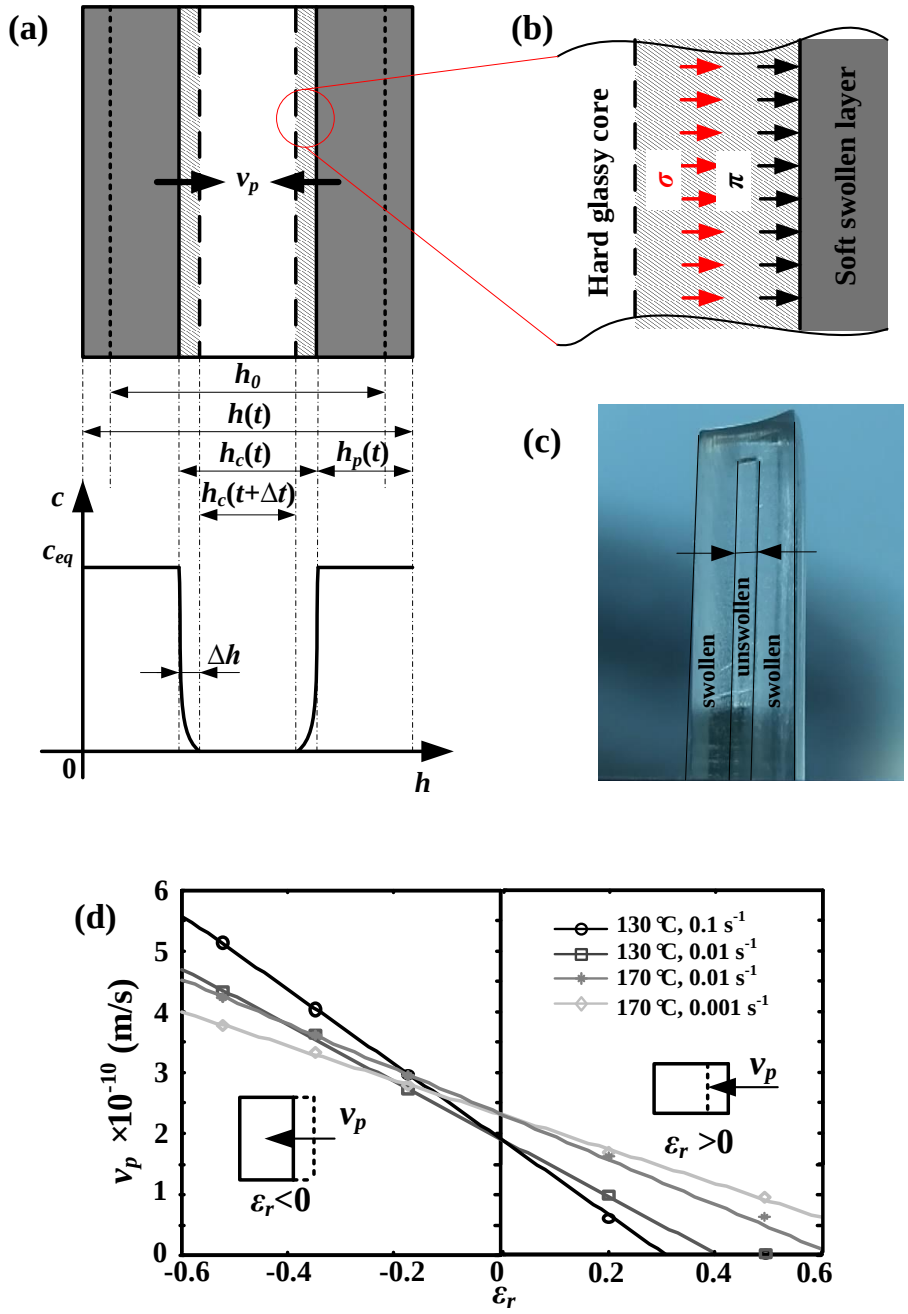

Figure 5.15 PSEP effect. (a) Sketch of ethanol transportation and profiler of ethanol concentration over cross-section; (b) sketch of thin element under osmotic stress and recovery stress; (c) sharp ethanol penetration front; (d) relationship between v_p and ε_r.

5.2 Numerical simulation and comparison

In Chapter 4, a generic 3-D finite element model is presented to simulate the thermo-responsive SME in polymeric SMMs. Here, we apply this model to study thermo-/chemo-responsive SME in PMMA.

5.2.1 Thermally induced recovery

In this section, thermally induced shape recovery in PMMA is simulated following the procedure described in Section 4.1.3.

5.2.1.1 Material models and parameters

Since all PMMA samples programmed at $T_p < T_g$ can fully recover, as shown in Figure 3.14, there is not any permanent plastic strain. As described in Section 3.3, RP-SME is observed in PMMA. We took into account RP-SME in this simulation. As aforementioned, RP-SME happens when the sample programmed at low temperatures ($<T_g$), in which recovery of one part of quasi-plastic strain occurs at lower heating temperatures and finishes at about T_g-20°C, i.e., LTR; recovery of the other part of quasi-plastic strain occurs at high heating temperatures and finishes above T_g i.e., HTR. Figure 5.16 illustrates this phenomenon.

We define ε_p as the total quasi-plastic strain, $\varepsilon_p^{\,l}$ as the low temperature recovery part, and $\varepsilon_p^{\,h}$ as the high temperature recovery part, so that,

$$\varepsilon_p = \varepsilon_p^{\,l} + \varepsilon_p^{\,h} \tag{5.9}$$

and the maximum programming strain (ε_m) can be expressed as

$$\varepsilon_m = \varepsilon_e + \varepsilon_p^{\,l} + \varepsilon_p^{\,h} \tag{5.10}$$

where ε_e is the elastic strain.

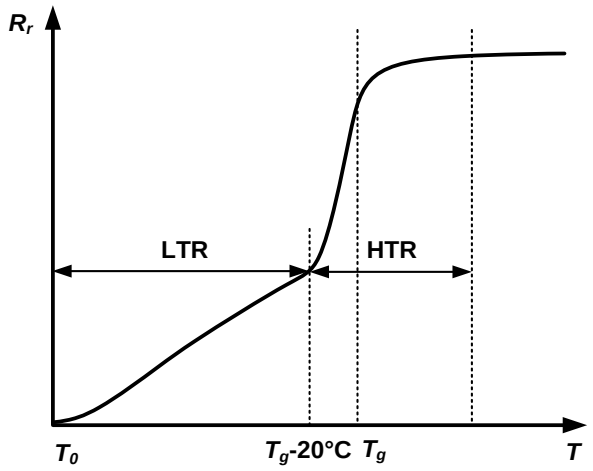

Figure 5.16 Illustration of RP-SME.

HTR corresponds to elastic stress (entropy force) release during reheating at high temperatures, which can be simulated as the hyper-elastic behavior. LTR corresponds to the stored elastic energy due to micro defects formation (e.g., micro shear domains), which can be simulated as a quasi-elastic behavior. It means that $\varepsilon_p^{\,l}$ can be considered as quasi-elastic strain in simulation, in which the driving force is a function of $\varepsilon_p^{\,l}$ and the modulus at T_g-20°C.

Although we divided the quasi-plastic strain into two parts, the constitutive law for material model is not changed. According to our proposed classification described in Section 3.1, PMMA is a typical DSM (glassy state and rubbery state) based SMM. A hyper-elastic model was used for rubbery state (refer to Section 4.1.2.3), and a visco-plastic model was used for glassy state (refer to Section 4.1.2.4). The materials properties used in simulation are listed in Table 5.1.

Table 5.1 Material properties for PMMA.

	Parameters	Values
Volume fraction evolution	A	6
	T_0 (°C)	100
Rubbery state	μ (MPa)	6
	λ_L	1.5
	k (MPa)	1000
Glassy state	E (MPa)	700
	ν	0.35
	σ_{y0} (MPa)	100
	m	0.24
	γ (s^{-1})	0.01
	n	2
	K_i (MPa)	1, 40
	ε_i	0.3, ∞

T_0 and A were obtained by curve fitting of the evolution in modulus obtained by DMA test. The details of curve fitting refer to [66]. Dashed line in Figure 5.17 shows the evolution of rubbery state in PMMA derived from Eqn. (4.3). Dotted line and solid line in Figure 5.17 show modulus vs. temperature relationship from DMA test and by prediction using the parameters in Table 5.1.

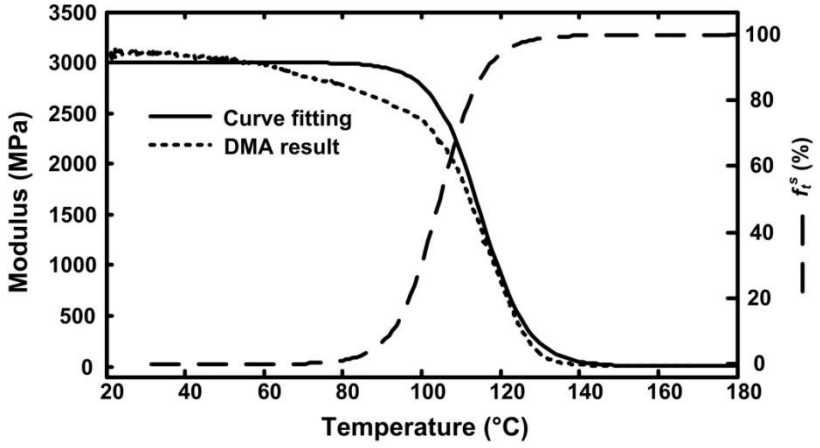

Figure 5.17 Modulus vs. temperature relationship and evolution of volume fraction of rubbery state in PMMA.

A series of uniaxial compressive tests were conducted at different strain rates at 130 ℃. The parameters for the hyper-elastic model (for the rubbery state) are determined by using the curve fitting tool in ANSYS based on the results of uniaxial compressive tests.

As aforementioned, the time-dependent unsteady behavior (relaxation and creeping) is relatively small in current study. The visco-plastic model used here just is only focused on the relationship between strain rate and yielding stress. The parameters for the visco-plastic model (for the glassy state) are determined in two steps. (1) In Eqn. (4.9), there are three parameters (σ_{y0}, m *and* γ) to be determined. In order to determine the actual values of them, a series of uniaxial compression tests at different strain rates were conducted at 20 ℃. σ_{y0}, m *and* γ were determined by means of data fitting of the stress vs. strain curves. (2) In a stress vs. strain curve, there are two apparent separated ranges after yielding (n=2); one is the strain softening range (K_1=1, ε_1=0.3), and the other is the strain hardening range (K_2=40, ε_2=∞). The actual meanings of these parameters are discussed in Section 4.1.2.4.

Figure 5.18 compares the predicted and experimental result of stress vs. strain curves of PMMA under different conditions. The parameters are from Table 5.1.

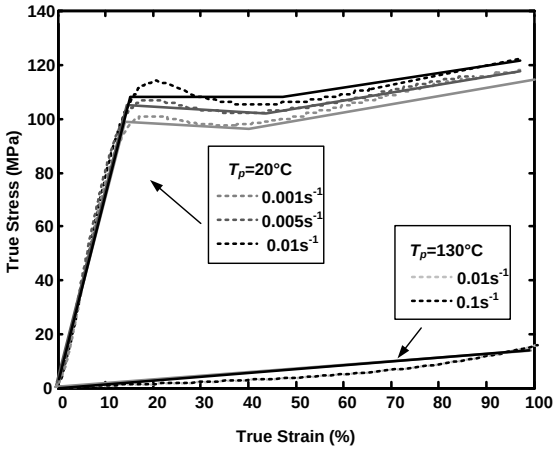

Figure 5.18 Stress vs. strain behavior of PMMA under uniaxial compression. Dotted line: experimental result; Solid line: predicted result.

5.2.1.2 Simulation and comparison

A 3-D, 10-node tetrahedral element was used. As shown in Figure 5.19, the representative unit is a $1 \times 1 \times 1$ mm^3 cubic with 6400 elements and 9929 nodes. Simulation follows the procedure described in Section 4.1.3.

Here, we focused on simulation of TME in both strain based in free recovery and stress based in constrained recovery, and RP-SME in PMMA. Refer to Section 3.2.3 for experimental results about TME in PMMA (refer to Figure 3.11a and Figure 3.12a). The experimental result of RP-SME is reported in Section 3.3 (refer to Figure 3.14). The actual experimental procedure was followed during simulation.

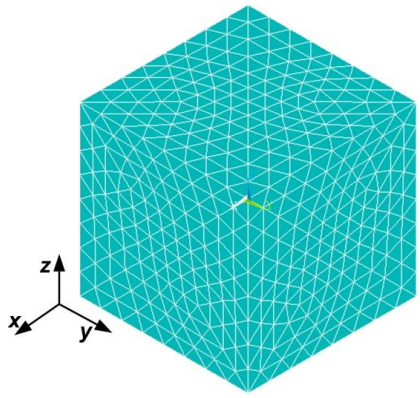

Figure 5.19 3-D finite element model for PMMA.

(1) TME in PMMA

As in experiments, cubic samples were compressed to 50% strain at different T_ps (within the glass transition range). Then they were cooled back to 20°C and unloaded. Finally, they were gradually heated to 140°C for free recovery or constrained recovery. The

detailed simulation procedure refers to Figure 4.3 and Section 4.1.3. Figure 5.20 illustrates the shape change in a shape memory cycle by simulation.

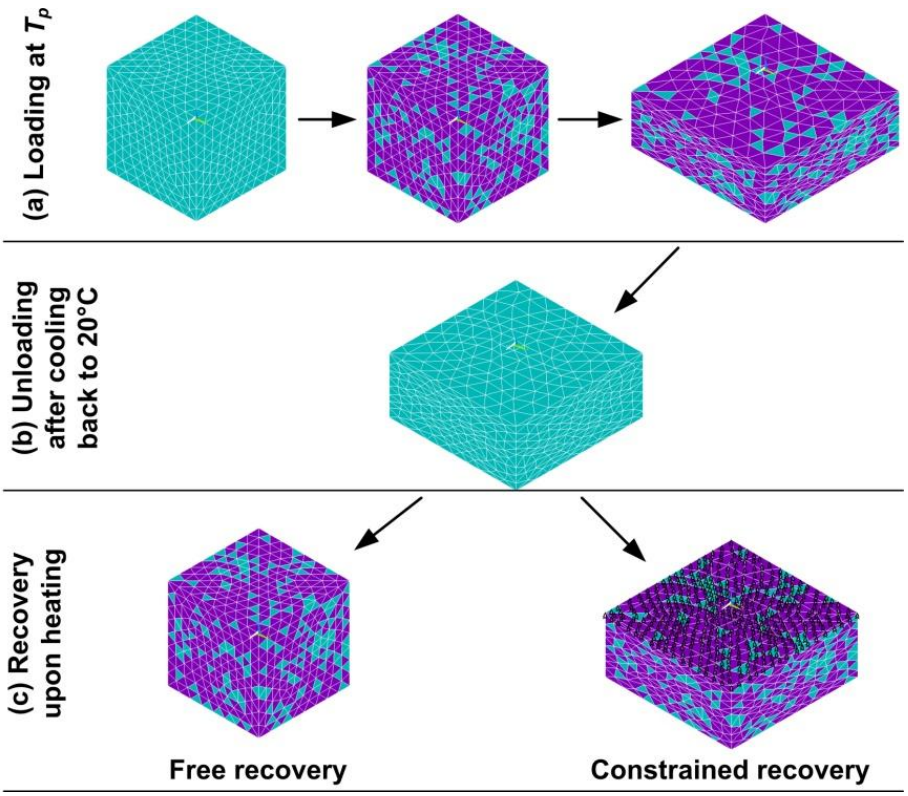

Figure 5.20 Illustration of a shape memory cycle. Blue area: glassy state; purple area: rubbery state.

Solid lines in Figure 5.21 show the relationships between R_r (in free recovery) and heating temperature in PMMA samples programmed at different T_ps (within the glass transition range, shown in Figure 5.1).

It can be seen the shape recovery temperature (T_r) is related to T_p. It increases as T_p increases. Dashed lines in Figure 5.21 represent the corresponding experimental results for comparison. It can be seen that simulation is able to catch the major trend as shown in the experimental results.

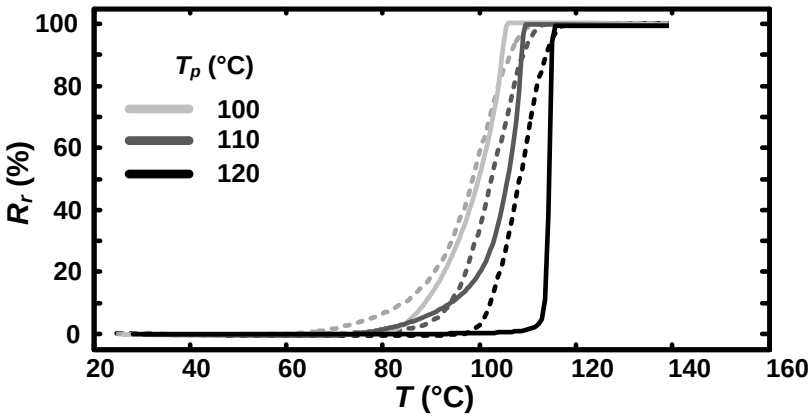

Figure 5.21 Strain based TME in PMMA.

Solid lines in Figure 5.22 show the relationships between σ_r (in constrained recovery) and heating temperature in PMMA samples programmed at different T_ps within the glass transition range. It can be seen that for samples programmed at 100°C, 105°C, and 110°C, σ_r continuously increases before reaching T_p, and then decreases continuously upon further heating; for the sample programmed at 120°C, σ_r monotonically increases upon heating and then reaches a constant value. Dashed lines in Figure 5.22 show the experimental results for comparison.

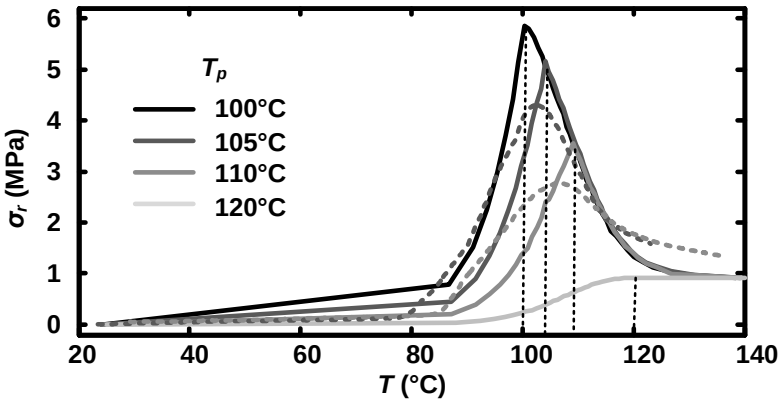

Figure 5.22 Evolution of recovery stress upon heating.

(2) RP-SME in PMMA

As aforementioned, at low temperature the recovery of quasi-plastic strain is divided into two parts, namely LTR and HTR. Due to different recovery mechanism for them, it is necessary to determine the ratio of them.

According to the experimental results (refer to Figure 3.14), the recovered strain in LTR range is defined as $\varepsilon_p^{\ l}$, and the recovered strain in HTR range is $\varepsilon_p^{\ h}$. The relationship between ($\varepsilon_p^{\ l}/\varepsilon_p^{\ h}$) and T_p was roughly obtained by curve fitting, and may be expressed as,

$$\varepsilon_p^{\ l}/\varepsilon_p^{\ h} = 2.85\exp(-T_p/33.67)-0.1 \tag{5.11}$$

Figure 5.23(a) plots the ($\varepsilon_p^{\ l}/\varepsilon_p^{\ h}$) vs. T_p relationship. Based on this, we can simulate the RP-SME in PMMA.

Figure 5.23(b) compares the experimental results and simulation of $\varepsilon_p^{\ l}$ and $\varepsilon_p^{\ h}$ at different T_ps.

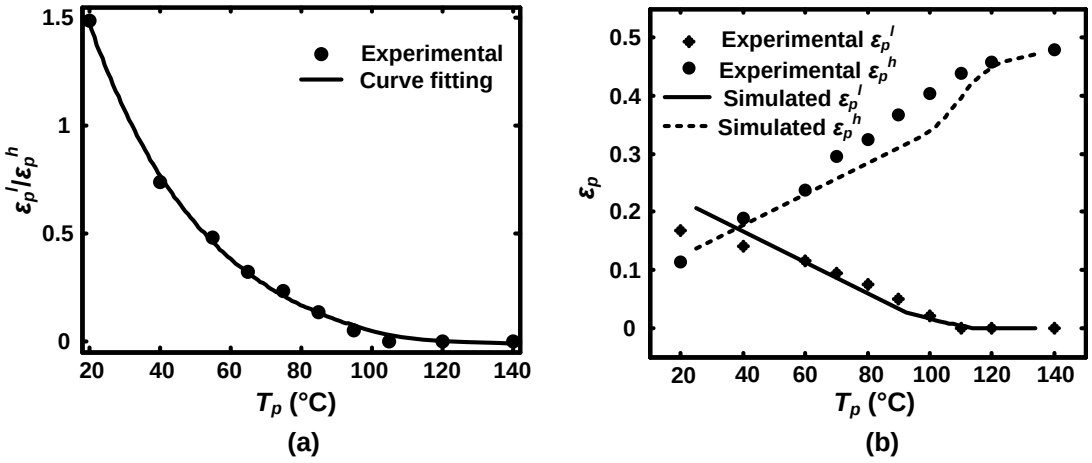

Figure 5.23 Influences of T_p on $\varepsilon_p^{\ l}$ and $\varepsilon_p^{\ h}$.

In a RP-SME simulation, the driving force for shape recovery includes not only the elastic stress (entropy force) in the rubbery state, but also the quasi-elastic stress in the glassy state. The first one is related to $\varepsilon_p^{\ h}$, and later one is related to $\varepsilon_p^{\ l}$.

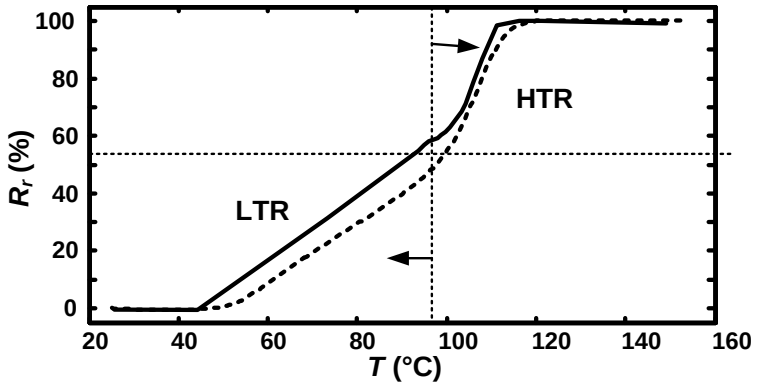

Figure 5.24 RP-SME in PMMA.

A cubic 3-D model was compressed to 50% strain at 20°C, and was unloading. Then, the cubic sample was heated to 140°C. Figure 5.24 reveals the RP-SME in PMMA, in which the solid line is simulation, and the dashed line is the experimental result (as described in Section 3.3). Good agreement is observed.

5.2.2 Chemically induced recovery

The *phase* transition approach also is applicable for simulation of chemo-responsive SME. We applied above model to simulate the chemo-responsive SME in PMMA. The programming part is essentially the same as in the thermo-responsive SME, while the recovery part is different.

Refer to Table 5.1 for the mechanical properties of PMMA used in programming. In the simulation of ethanol-induced recovery, the mechanical properties of the softened PMMA layer and glassy core were obtained from the DMA results (refer to Figure 5.8c).

A piece of 3 mm thick dog-bone shaped PMMA sample (refer to Figure 5.5a) was stretched to 50% strain at a strain rate of $0.01s^{-1}$ at 120°C. Then it was cooled back to 20°C and unloaded. The rectangular central part was cut out of the dog-bone shaped samples. This rectangular sample was immersed into room temperature ethanol. The boundary of ethanol penetration in PMMA was monitored. v_p is roughly obtained as 1.08 μm/hr, 1.08 μm/hr, and 0 μm/hr along thickness, width, and length directions, respectively. Figure 5.25(a) illustrates the real sample. R_r along length direction is obtained by monitoring of the displacement of point *A*.

A 3-D, 8-node hexahedron element was used in this simulation. Figure 5.25(b) shows the finite element model (15000 elements and 17238 nodes), which is 1/8 of the real sample.

The simulation of ethanol induced free recovery is similar to thermally induced shape recovery. However, unlike heating-induced glass transition, the penetration of ethanol into PMMA follows particular directions. v_p and time are key parameters in simulation.

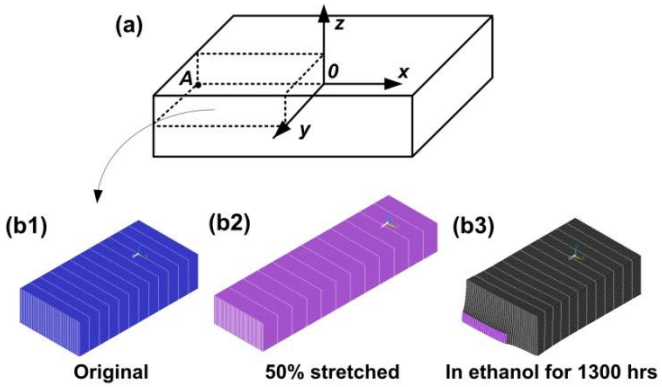

Figure 5.25 Demonstration of PMMA sample. (a) Sketch of the real sample; (b) finite element model corresponding to 1/8 of the real sample.

Solid line in Figure 5.26(a) shows evolution of R_r (length direction) as time increases. Figure 5.26(b) shows the pre-stretched PMMA in ethanol after 300 hrs. Figure 5.26(c)

shows simulated pre-stretched PMMA in ethanol for 300 hrs. It can be seen that simulation is in good agreement with the experimental result.

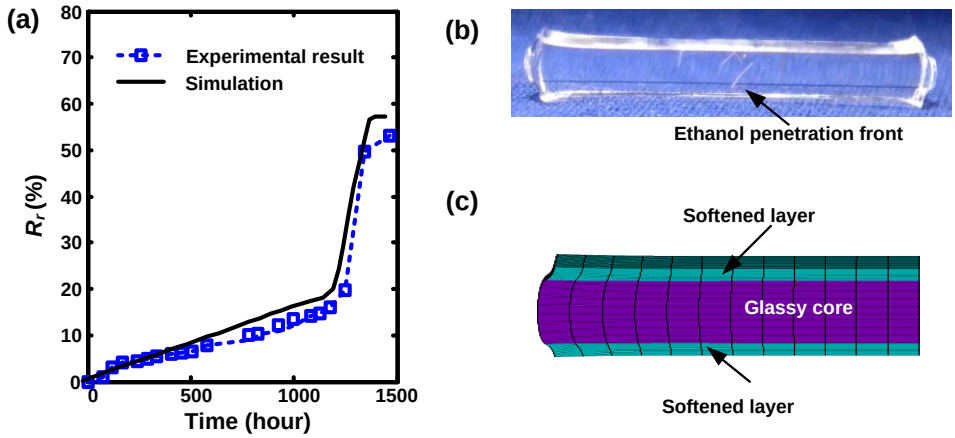

Figure 5.26 Chemically induced recovery in PMMA. (a) R_r vs. time relationship; (b) pre-stretched PMMA sample in ethanol after 300 hrs; (c) simulation of pre-stretched PMMA in ethanol after 300 hrs (1/2 of the real sample).

5.3 Summary

This chapter presents a systematical investigation on the thermo-/chemo-responsive SME in PMMA experimentally and analytically. PSEP phenomenon was studied in detail. It is demonstrated that the *phase* transition based 3-D finite element model is able to simulate the TME, RP-SME and chemo-responsive SME.

Chapter 6 Thermo/chemo-responsive SME for micro/nano surface patterning

Periodic micro/nano-sized surface features can significantly alter many surface-related properties, such as bonding, surface wetting, friction, reflection, drag and adhesion [191-193]. Fabrication of well defined surface patterns is in great demand. In this chapter, we present several surface patterning methods utilizing the thermo-/chemo-responsive SME in polymeric materials. Different micro/nano-scale surface patterns are obtained by utilizing these methods individually or combined. As shown here, both size and shape of resultant patterns can be well controlled. Furthermore, reversible surface pattern and 3-D pattern can be achieved.

6.1 Thermo-responsive SME for surface patterning

6.1.1 Indentation-polishing-heating method

A simple surface patterning technique, namely indentation-polishing-heating (IPH) method, was proposed previously, which can be used to produce different sized and shaped protrusion arrays atop a polymer by indentation, followed by polishing and heating for thermally induced shape recovery [164-166, 194], as revealed in Figure 6.1. As we can see in Figure 6.1(a), an indent with a depth of d_0 is obtained atop a piece of polymer using a spherical (e.g., a steel ball). Subsequently, a thin surface layer with a thickness of d_p is polished away. After polishing, the polymer is heated and a protrusion is resulted. The exact shape of the protrusion is dependent on the indentation depth and polishing depth, etc, as illustrated in Figure 6.1(c).

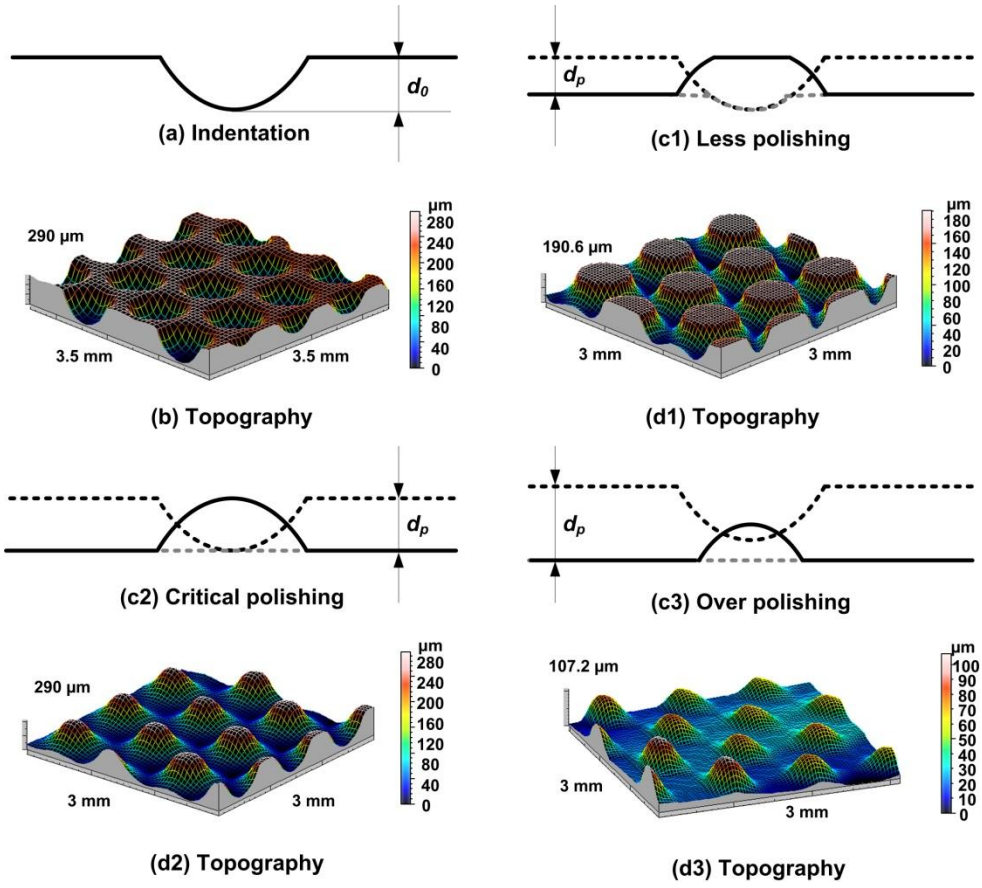

Figure 6.1 IPH method for surface patterning atop polymer (polystyrene). (a) and (c) Sketches of indent and protrusion; (b) and (d) 3-D images of arrays of indent/protrusion. d_o is the depth of the indent; and d_p is the depth of the polished layer.

In one real experiment, 1 mm diameter steel balls were packed atop a piece of 3 mm thick polystyrene (PS) plate [bought from Cornerstone Research Group (CRG), USA] and compressed by 0.3 mm at 100 ℃ at a loading speed of 0.003 mm/s using Instron 5569. After compression, a Taylor scanner (Taylor Hobson) was used to scan the sample surface. Figure 6.1(b) shows the topography of a typical indent array. Depending on the exact polishing depth (d_p) [300 nm diameter Al_2O_3 suspension (Buehler) was used in polishing to achieve a smooth surface], after heating to 100°C, which is well above the glass transition temperature (T_g, which is about 64^{o}C [164]) of this PS, different shaped protrusion arrays, from flat-top protrusion array to crown-shaped large/small protrusion

array, which correspond to less-polished, critical-polished, and over-polished cases, respectively, as shown in Figure 6.1(d) were resulted.

The underlying mechanism behind the IPH method is due to the thermo-responsive SME in this polymer. Figure 6.2(a) reveals the DMA result of this PS (sample dimensions: 5×15×1 mm^3, in three point bending mode, from 20°C to 140°C at a heating rate of 5°C min^{-1} and with a dynamic force of 110 mN, a static force of 100 mN, and a frequency of 1 Hz). The onset of glass transition based on storage modulus curve is about 65°C. Figure 6.2(b) shows a typical depth-versus-force curve in compressing an array of 1 mm diameter steel balls packed atop this PS plate.

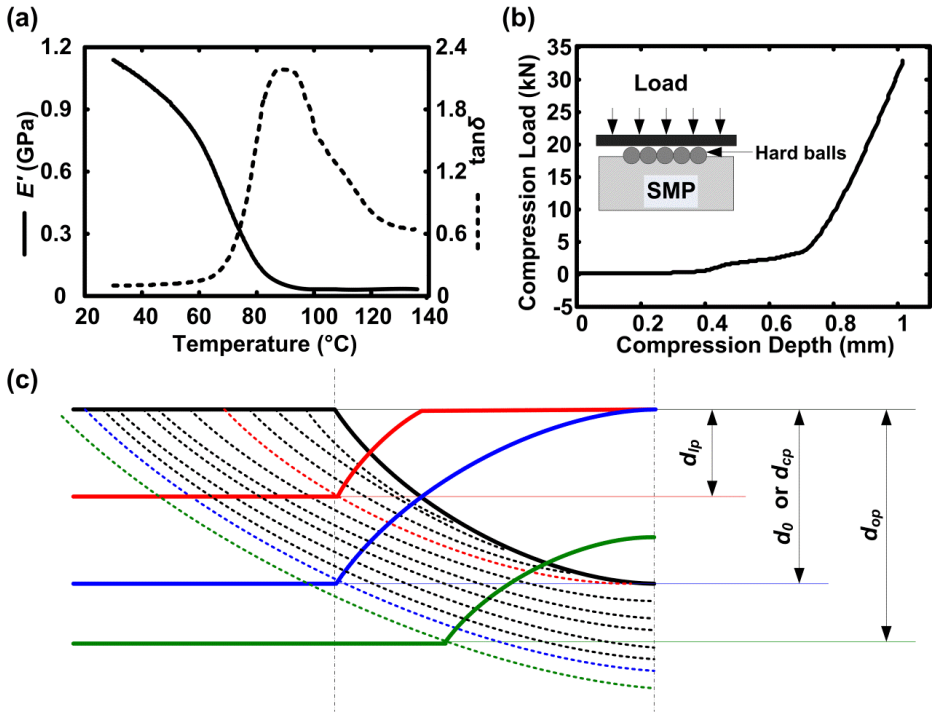

Figure 6.2 Mechanism of IPH method. (a) DMA result of PS; (b) Typical curve of indentation depth vs. compressive load; (c) illustration of the relationship between polishing depth and shape of protrusion. d_o is depth of indent; d_{lp} is thickness of less polished layer; d_{cp} is thickness of critical polished layer; and d_{op} is thickness of over polished layer.

Figure 6.2(c) is a sketch of the mechanism behind different shaped protrusions after polishing and heating. Dotted lines represent the "dislocation" (quasi-plastic deformation) in the polymer, which also represent the *plastic* zone. If without polishing, the indent will simply disappear after heating due to the thermally induced SME. If the indented sample is less-polished, the remaining indent is able to fully recover its original height upon heating, which results in a flat-top shape. With the increase of polishing depth, large and small crown shaped protrusions are produced. Theoretically speaking, the critical polishing depth (d_{cp}) for the transition from flat-top protrusion to crown shaped protrusion is the indentation depth (d_0).

On the other hand, in a pre-stretched (in the in-plane direction) sample, after IPH, elliptical shaped protrusion can be produced [164]. Furthermore, by using other shaped indenters, different shaped protrusions can be fabricated [164, 165]. This technique is simple for surface patterning to produce micro- and nano-sized protrusive features atop polymers (refer to [165] for a typical nano protrusion, which is about 400 nm in width and 400 nm in height). However, polishing is not a really favorable processing technique in engineering practice, in particular for nano-sized features.

6.1.2 Wrinkling

Probably the first systematic investigation of wrinkling phenomenon due to the buckling of a thin elastic film deposited atop a soft elastic substrate [such as polydimethylsiloxane (PDMS)] was carried out by Bowden et al. [177]. Since then, this phenomenon has attracted great interest from many researchers and has been utilized as a cost-effective approach for surface patterning [176, 195-199].

6.1.2.1 Theory of wrinkling

Figure 6.3 illustrates the basic mechanism of wrinkling of a stiff thin layer atop a soft substrate that exhibits highly nonlinear behavior and can be described by the Föppl-von Kármán equations [178] as,

$$\begin{aligned} &\frac{Eh^3}{12(1-\nu^2)}\Delta^2 w - h\frac{\partial}{\partial x_\beta}\left(\sigma_{\alpha\beta}\frac{\partial w}{\partial x_\alpha}\right) = P \\ &\frac{\partial \sigma_{\alpha\beta}}{\partial x_\beta} = 0 \end{aligned} \tag{6.1}$$

where E is the Young's modulus, $\sigma_{\alpha\beta}$ is stress tensor, h is the thickness of the thin layer, w is the out of plane deflection, ν is the Poisson's ratio, P is the external normal force per unit area of the plate, and Δ is 2-dimensional Laplacian. However, these nonlinear partial differential equations are too difficult to be solved analytically. Only some one-dimensional cases can be solved analytically to get closed-form solution [200, 201]. Different semi-analytical methods and numerical simulations are normally applied to quantitatively study the wrinkling behavior of a thin layer under an external force [178]. A brief summary of one semi-analytical method is presented here.

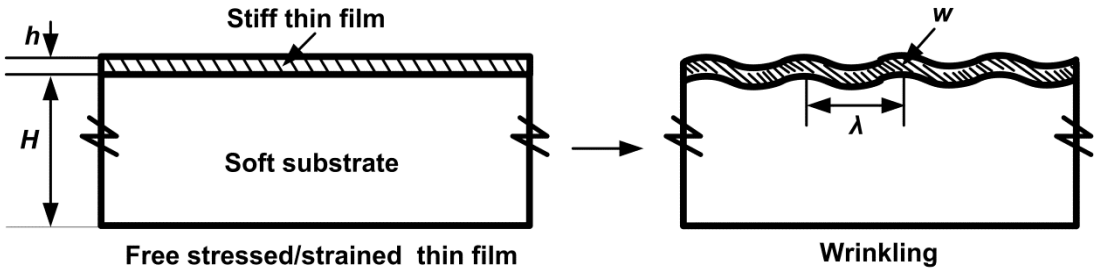

Figure 6.3 Wrinkling phenomenon.

The semi-analytical method focuses on the energies due to the in-plane strain (stretching), out-of-plane strain (bending), and the work done by the external in-plane stresses. Upon wrinkling, the work done by the in-plane stress is transferred into the wrinkling energy of the thin film, and the elastic energy of the soft substrate. This method can provide the critical conditions (critical stress, σ_c, and critical wavelength, λ_c) for wrinkling.

Strain energy in wrinkled thin film — The strain energy in a wrinkled thin film, U_f, is composed of stretching energy due to the in-plane strain, and bending energy due to the out-of-plane deformation. It may be expressed as [178, 202],

$$U_f = \int_A \left(\frac{h}{2} L_{ijkl} \dot{E}_{kl} \dot{E}_{ij} + \frac{h^3}{24} L_{ijkl} \dot{K}_{kl} \dot{K}_{ij} \right) dA \tag{6.2}$$

where h is thickness of thin film, L_{ijkl} is the fourth-order modulus tensor, $\dot{E}_{ij}$ is the increment in stretch strain, $\dot{K}_{ij}$ is the increment in bending strain, and A is the area where wrinkling occurs.

Wrinkling energy in substrate — According to Winkler's hypothesis [202], the influence of the soft substrate is equivalent to a group of springs with a stiffness of k (further discussed later in this section). Therefore, a part of the energy is stored in the substrate during wrinkling. Assume that the thin film is always well bonded to the substrate, and the displacement of the thin film/shell also represents the displacement of the top surface of the substrate. Hence, the wrinkling energy of the substrate, U_s, can be expressed as,

$$U_s = \frac{k}{2} \int_A w^2 dA \tag{6.3}$$

where *w* is the out-of-plane deflection.

Work done by in-plane stress — Work done by the in-plane stresses, *W,* can be presented in terms of the membrane stresses σ_i in the thin film and variation in its length Δl due to the out-of-plane deflection. Δl can be presented as [202],

$$\Delta l = \frac{1}{2} w_{,i}{}^2 dx_i \tag{6.4}$$

Subsequently, the work done by membrane force can be worked out as,

$$W = \frac{h}{2} \int_A \sigma_{ij} w_{,i} w_{,j} dA \tag{6.5}$$

where σ_{ij} is in-plane stress tensor, $w_{,i} = \frac{\partial w}{\partial x_i}$ and $w_{,j} = \frac{\partial w}{\partial x_j}$.

Winkler's hypothesis — This is a classical method to study the effects of soft substrate on mechanical deformation of a bilayer or sandwich structure. A parameter, *k,* is used to represent the effective stiffness of the substrate, which depends on the mechanical property of the material and characteristic depth of the deformation. It may be expressed as [202, 203],

$$k = \frac{f(\lambda / l_p) E_s}{l_p (1 - \nu_s{}^2)} \tag{6.6}$$

where E_s and ν_s are the Young's modulus and Poisson's ratio of the substrate, respectively and $\bar{E}_s = \frac{E_s}{1-\nu_s^2}$. $f(\lambda/l_p) \sim \lambda^2/l_p{}^2$ is a dimensionless function that depends on the geometry of the system, and l_p is the characteristic depth of the deformed substrate.

Figure 6.4 shows two kinds of substrate models. In different models, the effective stiffness is different. For the shallow substrate model ($h << H$), l_p is close to the characteristic thickness of the substrate (H), so that the stiffness of the substrate is given as $k \sim \frac{\bar{E}_s \lambda^2}{H^3}$ or $\frac{\bar{E}_s \lambda^2}{R^3}$ [177, 178]. For the deep substrate model ($h << \lambda \leq H$), l_p is close to the characteristic wavelength of the wrinkles on the substrate surface, so that the stiffness of the substrate is given as $k \sim \bar{E}_s / \lambda$ [178].

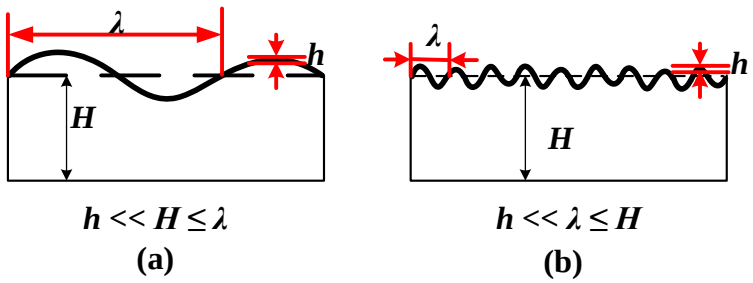

Figure 6.4 (a) Shallow substrate model. (b) Deep substrate model.

Wrinkling criterion — Wrinkles will appear when the work done by the thin film stresses is larger than the sum of the wrinkling energy of the thin film and the elastic energy of the soft substrate. Like the results of Hutchinson and Neale [204] for buckling of thin sheets or shells, the critical condition for wrinkling of thin films atop a soft substrate is,

$$W = U_f + U_s \tag{6.7}$$

Substituting Eqns. (6.1)-(6.6) into Eqn. (6.7), the wrinkling criterion can be derived as follows,

$$U_f + U_s - W = C \begin{pmatrix} w_0 \\ u_0 \\ v_0 \end{pmatrix} [M] \begin{pmatrix} w_0 & u_0 & v_0 \end{pmatrix} = 0 \tag{6.8}$$

Here, C is a constant (non-zero), w_0, u_0, and v_0 are the amplitude of out-of-plane deflection (w), amplitude of in-plane deformation (u and v) respectively, and $[M] = \begin{pmatrix} M_{11} & M_{12} & M_{13} \\ M_{21} & M_{22} & M_{23} \\ M_{31} & M_{32} & M_{33} \end{pmatrix}$. For an elastic thin film atop a flat substrate,

$$\begin{aligned}
M_{11} &= \frac{2\pi^4 h^3}{3}\left(\frac{L_{1111}}{\lambda_1^{\,4}} + \frac{L_{2222}}{\lambda_2^{\,4}} + \frac{2L_{1122}}{\lambda_1^{\,2}\lambda_2^{\,2}} + \frac{4L_{1212}}{\lambda_1^{\,2}\lambda_2^{\,2}}\right) - 2\pi^2 h\left(\frac{\sigma_1}{\lambda_1^{\,2}} + \frac{\sigma_2}{\lambda_2^{\,2}}\right) + \frac{k}{2} \\
M_{22} &= 2\pi^2 h\left(\frac{L_{1111}}{\lambda_1^{\,2}} + \frac{L_{1212}}{\lambda_2^{\,2}}\right) + \frac{k}{2} \\
M_{33} &= 2\pi^2 h\left(\frac{L_{1212}}{\lambda_1^{\,2}} + \frac{L_{2222}}{\lambda_2^{\,2}}\right) + \frac{k}{2} \\
M_{12} &= M_{21} = 0 \\
M_{13} &= M_{31} = 0 \\
M_{23} &= M_{32} = 2\pi^2 h\left(\frac{L_{1122}}{\lambda_1\lambda_2} + \frac{L_{1212}}{\lambda_1\lambda_2}\right)
\end{aligned} \tag{6.9}$$

where λ_1 and λ_2 are the wrinkles wavelength along the principle axes respectively, σ_1 and σ_2 are the in-plane stresses along principle axes respectively, the fourth-order tensor (L_{ijkl}) denotes the instantaneous modulus L_{ij}. For an isotropic elastic thin film, the elastic moduli (non-zero components) are $L_{1111} = L_{11} = \frac{E_f}{1-\nu_f^2}$, $L_{2222} = L_{22} = \frac{E_f}{1-\nu_f^2}$, $L_{1122} = L_{12} = \frac{\nu_f E_f}{1-\nu_f^2}$ and $L_{1212} = L_{44} = \frac{E_f}{2(1+\nu_f)}$, where E_f and ν_f are the Young's modulus and Poisson's ratio of the thin film, respectively, and $\bar{E}_f = \frac{E_f}{1-\nu_f^2}$.

Since w_0, u_0, and v_0 are not all zero, the wrinkling criterion can be obtained from,

$$\det[\mathrm{M}]=\begin{vmatrix} M_{11} & M_{12} & M_{13} \\ M_{21} & M_{22} & M_{23} \\ M_{31} & M_{32} & M_{33} \end{vmatrix}=0 \tag{6.10}$$

Case study: wrinkling of elastic thin film atop flat substrate — Assume that the system is under uniform biaxial stresses and ignore the in-plane displacement. For a flat substrate, h is the thin film thickness, H is the substrate thickness, $\lambda_1=\lambda_2=\lambda$, $\sigma_1=\sigma_2=\sigma_c$, $w\neq 0$ and $u=v=0$. [M] is obtained as,

$$\begin{aligned} M_{11} &= \frac{8\pi^4 h^3 \overline{E}_f}{3\lambda^4}+\frac{k}{2}-\frac{4\pi^2 h\sigma_c}{\lambda^2} \\ M_{22} &= M_{33}=\frac{\pi^2 h\left(3-\nu_f\right)\overline{E}_f}{\lambda^2} \\ M_{12} &= M_{21}=M_{13}=M_{31}=0 \\ M_{23} &= M_{32}=\frac{\pi^2 h\left(1+\nu_f\right)\overline{E}_f}{\lambda^2} \end{aligned} \tag{6.11}$$

Hence, the wrinkling criterion, which is det[M]=0, can be worked out as,

$$\det[\mathrm{M}]=\begin{vmatrix} M_{11} & 0 & 0 \\ 0 & M_{22} & M_{23} \\ 0 & M_{32} & M_{33} \end{vmatrix}=M_{11}\left(M_{22}M_{33}-M_{23}M_{32}\right)=0 \tag{6.12}$$

Since $(M_{22}M_{33}\text{-}M_{23}M_{32})\neq 0$, we can see that $M_{11}=0$ according to Eqn. (6.11). The criterion for wrinkling of a thin film atop a flat substrate is obtained as,

$$\sigma_c=\frac{2\pi^2 h^2 \overline{E}_f}{3\lambda^2}+\frac{\lambda^2 k}{8\pi^2 h} \tag{6.13}$$

where the effective stiffness of the substrate can be determined according to the substrate mode (shallow mode or deep mode, refer to Figure 6.4). The critical wavelength, λ_c, can be derived from Eqn. (6.13) when $d\sigma_c/d\lambda=0$.

For the shallow mode ($h << H \leq \lambda$), substituting $k = \pi \bar{E}_s \lambda^2 / H^3$ into Eqn. (6.13), the critical wavelength and critical stress are obtained as,

$$\lambda_c = \left(2\pi hH\right)^{1/2} \left(\frac{\overline{E}_f}{3\overline{E}_s}\right)^{1/6} ; \quad \sigma_c = \frac{\pi h}{2H}\left(3\overline{E}_s\right)^{1/3} \overline{E}_f^{\,2/3} \tag{6.14}$$

Similarly, for the deep mode ($h << \lambda \leq H$), substituting $k = \pi \bar{E}_s / \lambda$ into Eqn. (6.13), the critical wavelength and critical stress are obtained as,

$$\lambda_c = 2\pi h\left(\frac{4\overline{E}_f}{3\overline{E}_s}\right)^{1/3} ; \quad \sigma_c = \frac{1}{4}\left(3\overline{E}_s\right)^{2/3}\left(4\overline{E}_f\right)^{1/3} \tag{6.15}$$

Eqns. (6.14) and (6.15) are identical to the previous ones reported in, for instance Vandeparre et al. [205], Bowden et al. [177] and Cerda et al. [178].

6.1.2.2 Wrinkle patterns atop SMPs

Figure 6.5 presents the procedure of some typical wrinkling induced surface patterning methods atop different polymeric substrates. PS was from CRG, USA, with a T_g about 64 ℃ (Figure 6.5a). PMMA was purchased from Ying Kwang Acrylic Trading, Singapore, with a T_g about 110 ℃ (Figure 6.5b). PU (MM3520) was purchased from the SMP Technologies, Japan. Its T_g is about 35 ℃ (Figure 6.5c). Silicone-melting glue (SMG) was produced by mixing silicone elastomer (SYLGARD® 184) with an ethylene-vinyl acetate (EVA) based melting glue (Figure 6.5d).

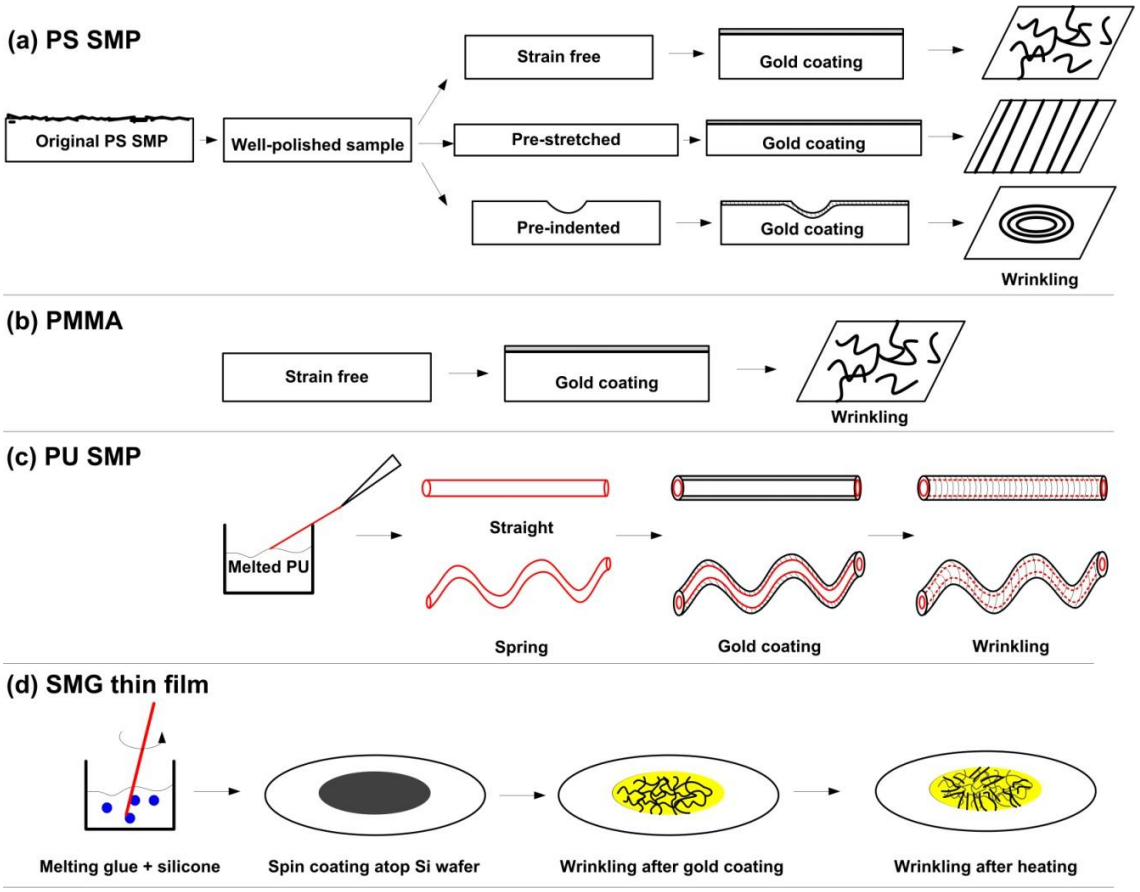

Figure 6.5 Procedure of sample preparation. The sputter-coated gold layer is about 10s nm.

Wrinkling atop PS SMP plate—As shown in Figure 6.6, different wrinkle patterns are obtained atop PS SMP plates. Bear in mind that the coefficient of thermal expansions of gold and PS are 1.4×10^{-5} K^{-1} and 5×10^{-5} K^{-1}, respectively, which are remarkably different.

Figure 6.6(a) shows a very smooth surface after gold coating. Figure 6.6(b) reveals typical isotropic labyrinth-shaped wrinkles atop a flat PS SMP (without any pre-strain) after being heated to 120 ℃. It was found that heating to below 120^{o}C did not result in any visible wrinkles at all.

It is well known that there is a critical compressive stress/strain value for wrinkling phenomenon to happen [177, 196, 197]. As noticed above, the PS SMP has a much higher

coefficient of thermal expansion than that of gold. In these samples, the compressive stress/strain is induced by means of thermal expansion mismatch (TEM) between the stiff/elastic thin film (gold) and soft/flexible substrate (polymer at high temperature), which is 2-dimensional, in-plane and isotropic. Hence, the resulted wrinkles are random without any preferential orientation, i.e., labyrinth.

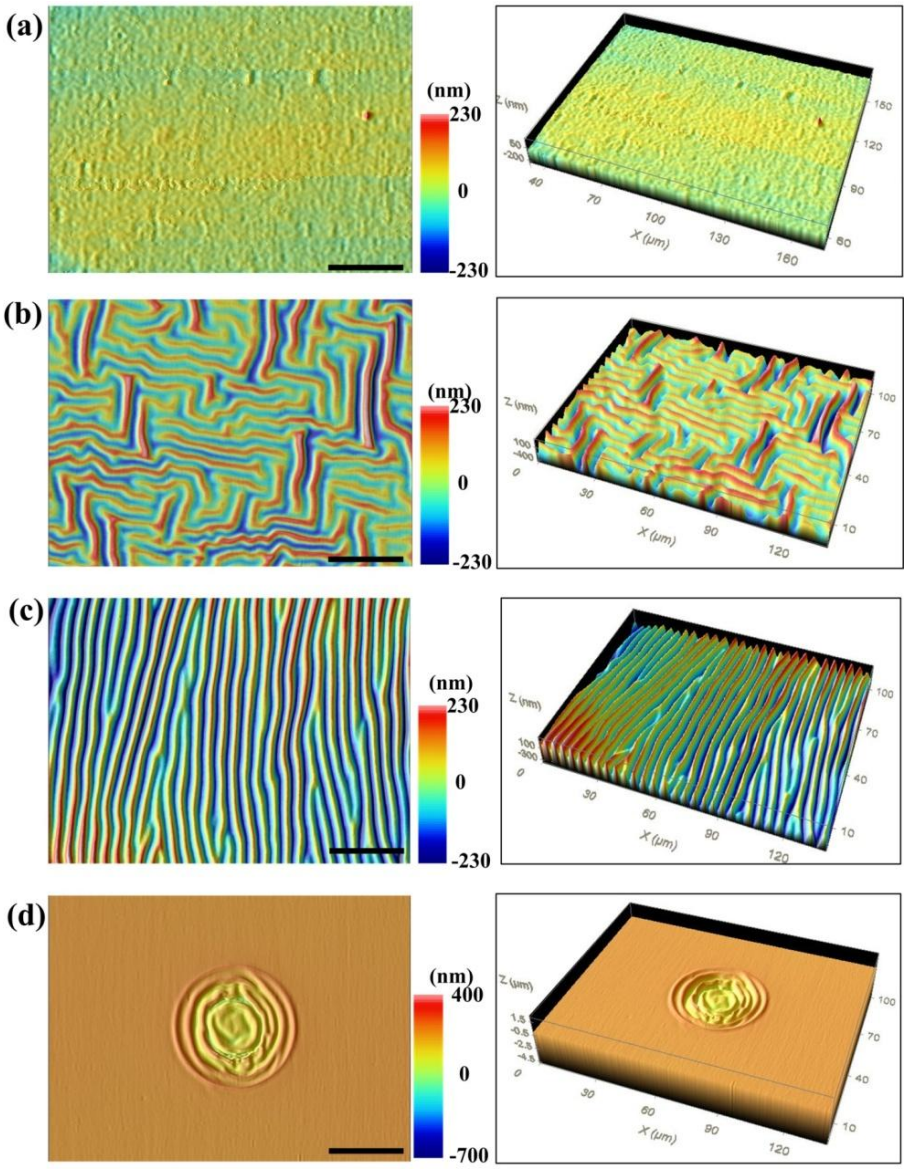

Figure 6.6 Different wrinkle patterns. 1: 2-D top view; 2: 3-D view. Scale bar: 20 μm.

In fact, the required heating temperature of 120 ℃ for wrinkling also indicates the minimal heating temperature to induce permanent slip between the gold film and polymer substrate to release the elastic stress due to the TEM between them upon heating. The fact that delamination has never been observed in our experiments implies excellent bonding between gold and polymer despite of the occurrence of slip between them. In the subsequent cooling process, the polymer substrate contracts more than that in the gold layer. Since the polymer substrate is soft, the compressive stress increases continuously till a critical condition is achieved, which results in the elastic buckling of the gold layer, i.e., wrinkling [191, 192].

Figure 6.6(c) shows typical anisotropic stripe-shaped wrinkles atop a pre-stretched PS SMP sample after being heated to 80 ℃, which is above the T_g of this polymer, and then cooled back to room temperature. Note that unless otherwise stated, hereinafter, the room temperature is about 20^{o}C. Since the polymer substrate was pre-stretched along one in-plane direction and then coated with a thin layer of gold, upon heating to 80 ℃ for shape recovery, the coated thin gold layer contracted together with the polymer substrate. Again, due to the difference in coefficient of thermal expansion, a compressive stress, which is along the pre-strain direction, is produced. During thermally induced shape recovery, the substrate softens remarkably at around the T_g. Consequently, the gold layer buckles along the shape recovery direction, resulting in stripe-shaped wrinkles.

Figure 6.6(d) reveals typical ring-shaped wrinkles atop a pre-indented sample. A spherical shaped indenter was used to make an indent before gold coating and then heating for shape recovery. As we can see, wrinkles are only formed within the indented area. This is because during shape recovery, the main deformation is longitudinal contraction, while the

latitudinal deformation is small. Therefore, the strain is dominated by the longitudinal deformation, which induces ring-shaped wrinkles perpendicular to the longitudinal direction.

Wrinkling atop PMMA plate — Figure 6.7 presents typical isotropic labyrinth-shaped wrinkles atop a piece of flat PMMA (without pre-straining). It should be pointed out that PMMA is a conventional engineering polymer. However, its shape memory phenomenon induced by either heating or solvent absorption is only briefly reported in the past and all limited to small strain range [170-172].The sample was coated with a thin layer of gold and then heated to 140 ℃, which is above its T_g. It was found that heating to below 140^{o}C did not result in any visible wrinkles at all. Coefficient of thermal expansion of PMMA is 2.22×10^{-4} K^{-1}, which is higher than that of gold. Same as in Figure 6.6(b), the wrinkles are random without any preferential orientation, i.e., labyrinth. Wavelength of the wrinkles is about 1 μm, and amplitude of them is about 10 nm.

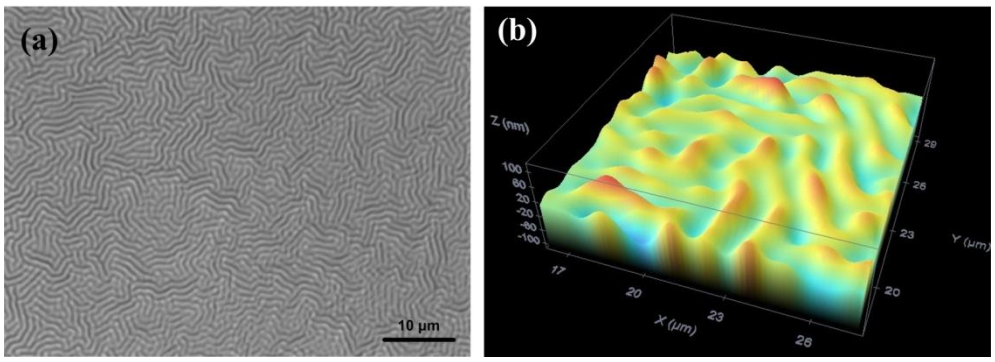

Figure 6.7 Isotropic wrinkles atop PMMA. (a) Optical image; (b) 3-D topography.

Wrinkling atop PU SMP fibres — As illustrated in Figure 6.5(c) and shown in Figure 6.8, there are two kinds of PU fibres. In general, straight PU fibre is produced at a low drawing speed, while PU spring is resulted at a high drawing speed. Significant

temperature gradient within the cross section of PU thread during pulling at a high speed, triggers the buckling of outer surface (which is at low temperatures and thus stiff) during thermally induced shape recovery of the inner part (which is at high temperatures and thus soft). This should be the underlying mechanism for these.

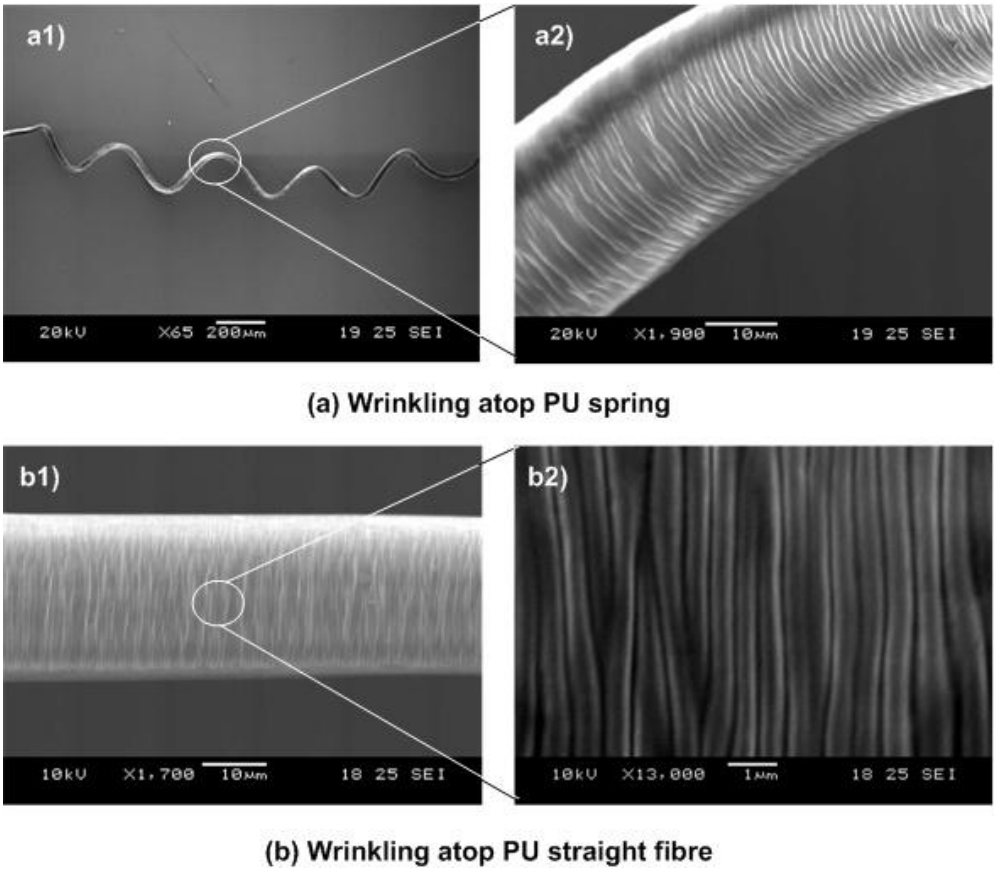

Figure 6.8 Wrinkling atop PU SMP fibres.

Figure 6.8(a1) reveals wrinkles atop a PU spring which has a wire diameter around 40 μm. In the experiment, after coating a thin gold layer atop, the spring was heated to 60℃. Regular strip shaped wrinkles with a wavelength close to submicron scale are observed in Figure 6.8(a2). Since 60^{o}C is the shape recovery temperature of this PU SMP, we may conclude that the shape recovery in the fibre is the cause of these wrinkles.

Figure 6.8(b) reveals the typical wrinkle patterns at two different scales in a piece of straight SMP fibre. According to Figure 6.8(b2), it is clear that the wavelength of these strip shaped wrinkles atop a cylindrical SMP fibre is actually at submicron scale. Since in the experiment, the fibre was heated to 60^{o}C only, again shape recovery should be the mechanism which induces the nano-sized wrinkles.

Wrinkling atop SMG thin film — Figure 6.9 reveals the typical wrinkle patterns atop a SMG thin film. After a piece of SMG thin film (about 300 μm thick) was prepared, a thin gold film was sputtered atop it. Right after gold deposition, random and tiny wrinkles were generated as shown in Figure 6.9(a). In the next step, the sample was heated to 100^{o}C. After the sample was cooled back to room temperature, a larger sized wrinkle feature was observed, as shown in Figure 6.9(b).

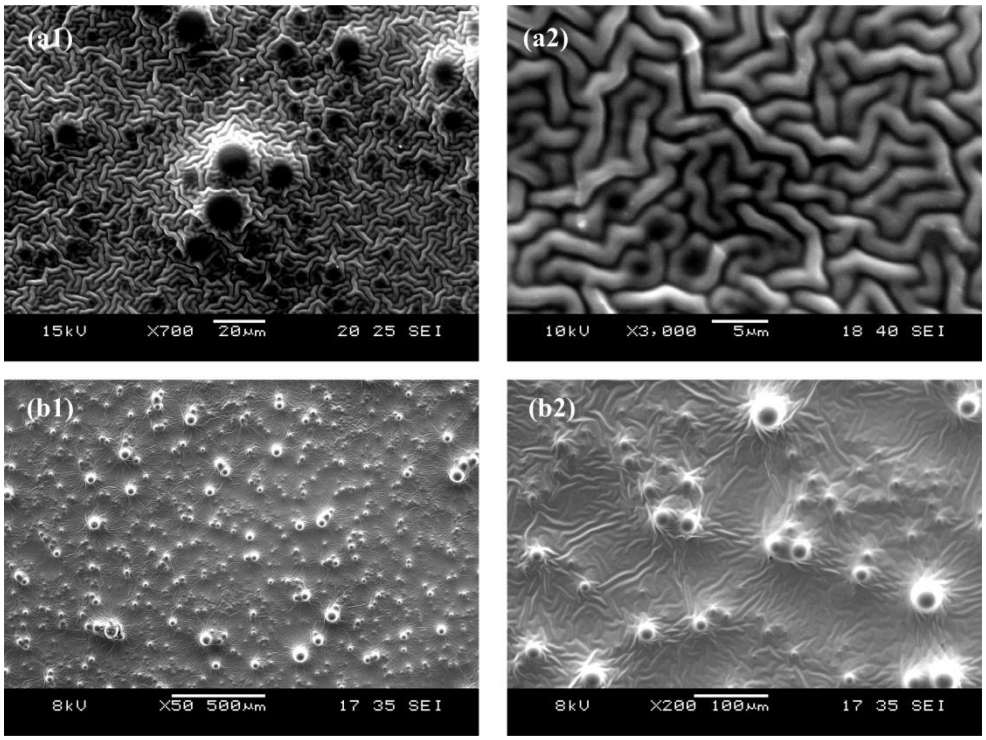

Figure 6.9 Wrinkling of SMG thin film. (a) Tiny wrinkles; (b) coarse wrinkles.

The wrinkles observed right after gold deposition should be due to TEM between gold and SMG film. The larger wrinkles after thermal cycling should be the result of melting and solidification of the spherical melting glue inclusions. Figure 6.10 reveals an interesting combination of both types of wrinkles, i.e., wrinkles inside wrinkles. The observed circular shaped particles should be melting glue inclusions.

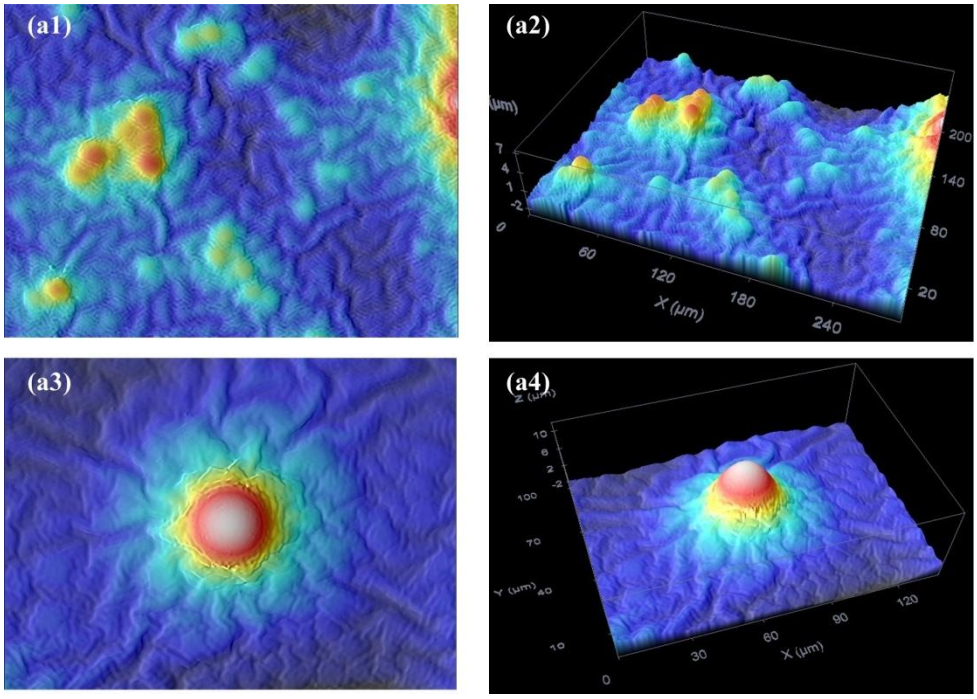

Figure 6.10 Wrinkles in wrinkles atop SMG thin film.

Evolution of wrinkle patterns — According to the theoretical analysis of the wrinkling behavior [18,19,21,22], the exact wrinkle pattern is dependent upon the stress/strain distribution. Here, evolution of wrinkle pattern as a function of heating temperature is investigated. Figure 6.11 reveals the evolution of surface morphology atop different PS SMP substrates. Figure 6.11(a) shows the evolution of surface morphology in a pre-stretched PS SMP sample. No wrinkle can be found if the heating temperature is below the T_g. Stripe-shaped wrinkles appear after heating to 80 ℃. The contraction of substrate

upon heating to 80^{o}C is able to generate enough compressive stress in the thin film and subsequently induce wrinkling. Upon further heating the sample with strip-shaped wrinkles to 120 ℃, wrinkle pattern changes from strip-shape to S-shape after cooling back to room temperature. This is due to the newly generated compressive stress induced by the TEM, which is isotropic.

Figure 6.11(b) reveals the evolution of surface morphology in a pre-indented PS SMP sample after being heated to different temperatures. After heating to 80 ℃, shape recovery within the indented area induces a compressive stress in the stiff gold film. When the compressive stress is over a critical value, ring-shaped wrinkles appear within the indented area, which means that extension deformation (in indentation)/contractive recovery (in heating) is limited within the indented area.

Upon heating to 100°C, the SMP substrate is fully in the rubber state, and the Young's modulus reaches the minimum. Therefore, a lower stress is enough to induce wrinkling. During indentation, right underneath the indented area the molecular chain is stretched along the longitudinal direction. On the other hand, the molecular chain is stretched within the area around the indent, and the strain over there is lower than the strain within the indented area. Therefore, it induces radial-shaped wrinkles around the indent at 100^{o}C. After heating to 120 ℃, the compressive stress induced by the TEM between gold film and SMP substrate is strong enough for wrinkling (labyrinth-shaped wrinkles) to happen. However, existing radial-shaped wrinkles (as initial defects) take the advantage and extend into areas far away from the indent, where if without initial defects, labyrinth-shaped wrinkles should be dominant.

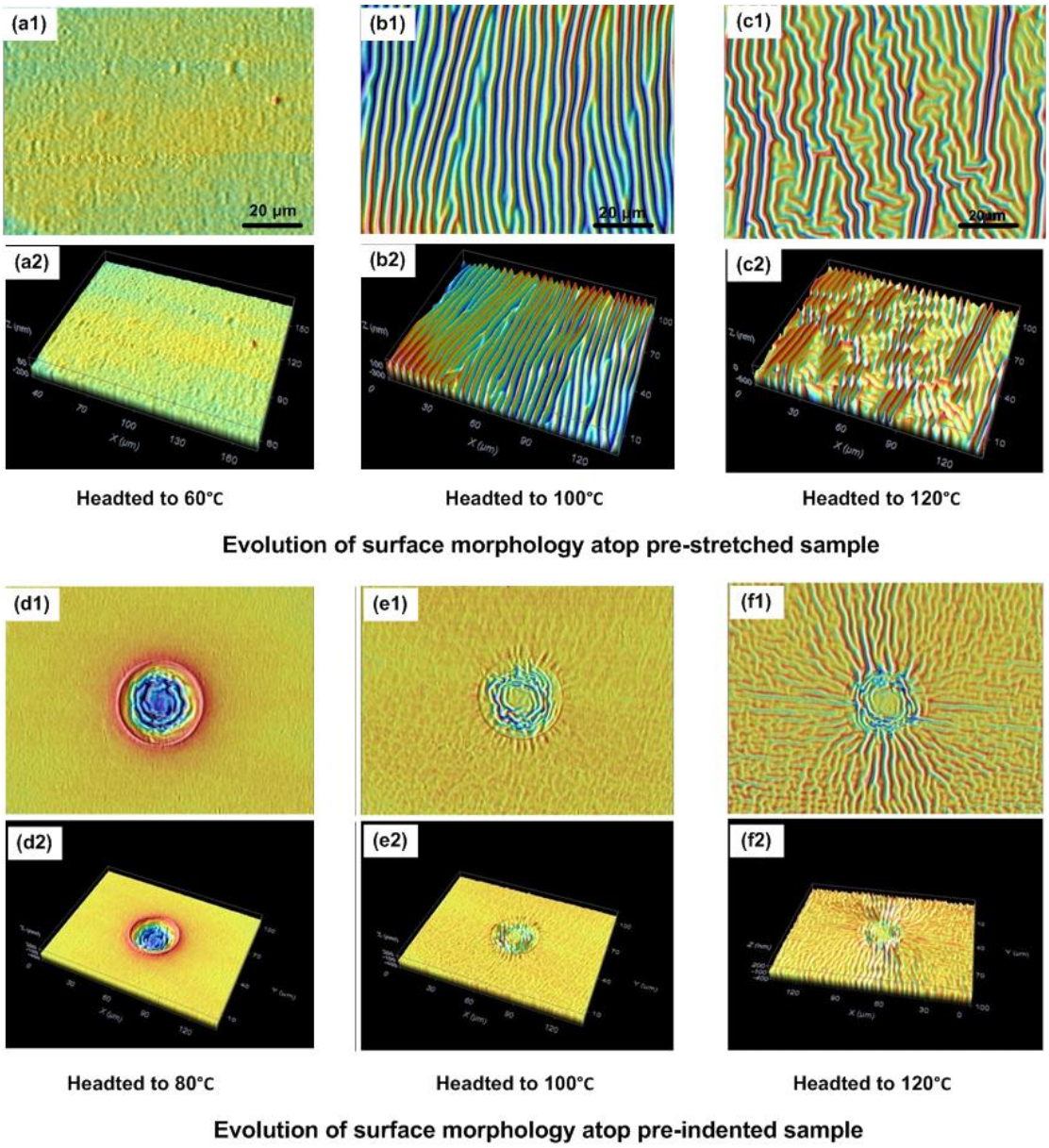

Figure 6.11 Evolution of surface morphology. 1: 2-D top view; 2: 3-d view.

Same as in the study of the PS SMP samples mentioned above, evolution of surface morphology atop both straight and spiral PU SMP fibres was experimentally investigated under different heating conditions. Both types of SMP fibres virtually follow the same trend. Hence, we only report one of them here.

Figure 6.12(a) reveals the surface morphology of PU SMP fibres (both straight and spiral shaped ones) after being heated to 25 ℃, which is below the T_g of this PU SMP. As expected, no visible wrinkles appear. Figure 6.12(b) presents the surface morphology of PU fibre after being heated to 35 ℃, which is the T_g of this polymer.

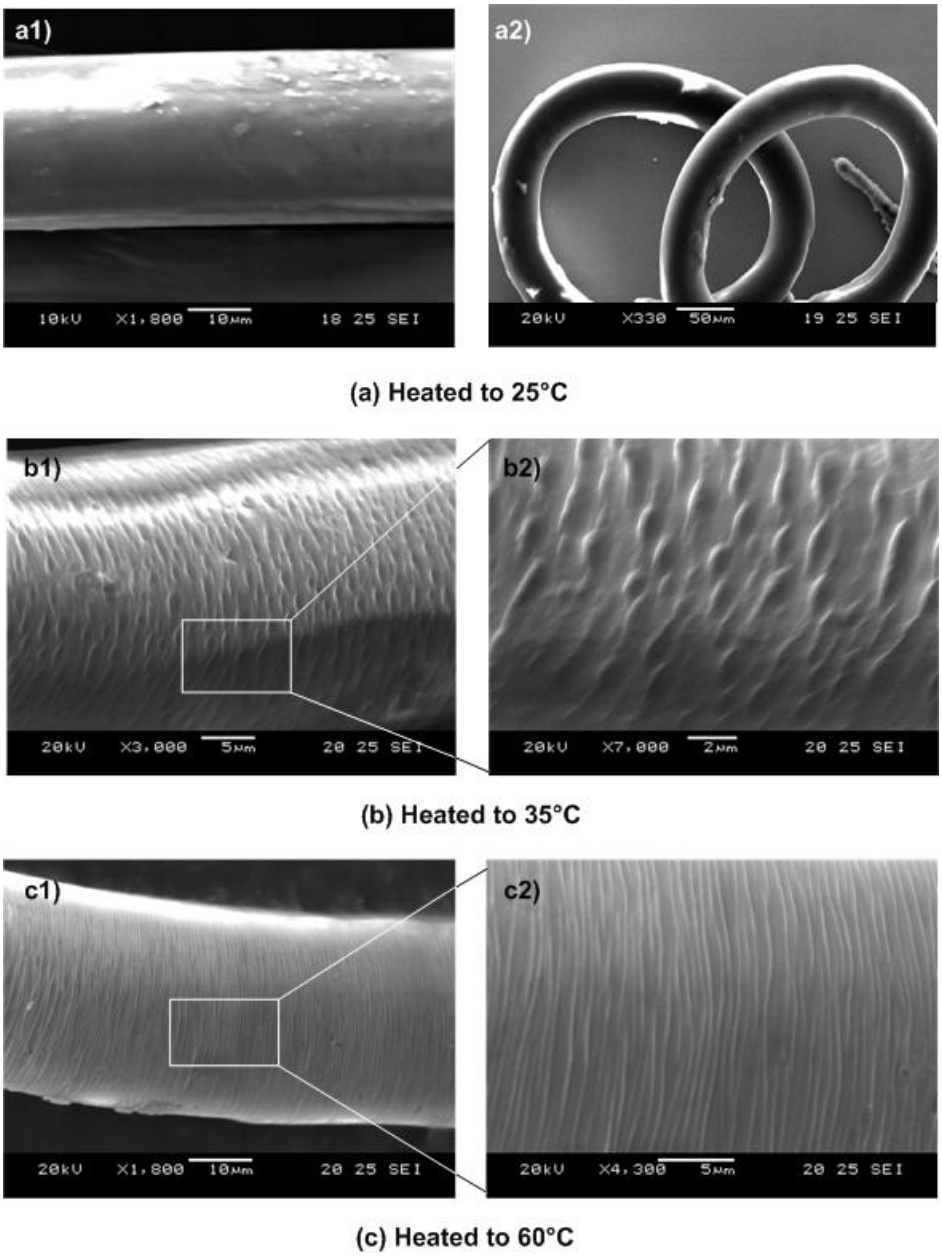

Figure 6.12 Evolution of surface morphology.

It can be seen that wrinkling only happens within some local areas and thus, wrinkles are discrete. Apparently, at this point of time, the compressive stress just reaches the wrinkling condition, but is not yet strong enough to produce continues wrinkles over the whole cross-section upon heating to this temperature. Since, at the T_g, the substrate is not full softened, full-scale wrinkling is prevented. After further heating to 60 ℃, which is well above the T_g, continuous wrinkles with a wavelength around 700 nm over the whole cross-section is observed as shown in Figure 6.12(c).

Size effect for wrinkling occurrence — Samples with different sized spherical indents were prepared following a standard procedure using a spherical and then heated to 80 ℃. The diameter of the spherical diamond indenter used here is 20 μm in radius. Different sized indents were achieved by using different maximum compression force.

Figure 6.13 shows typical surface profiles of pre-indented PS SMP with indent before and after being heated to 80 ℃. It is clear that the PS SMP almost fully recovers its original flat surface shape after heating. Wrinkles are only formed within the indented area. This is due to the compressive stress in the thin gold film (only within the indented area) during shape recovery.

In order to quantitatively study the critical stress/strain for wrinkling due to the shape recovery effect, a series of tests were conducted with different sized indents. Figure 6.14 shows the resulted surface morphology of them. It can be seen that we can hardly see any wrinkles if the diameter of a produced indent is smaller than about 24 μm. As such, this size might relate to the critical stress/strain value for wrinkling.

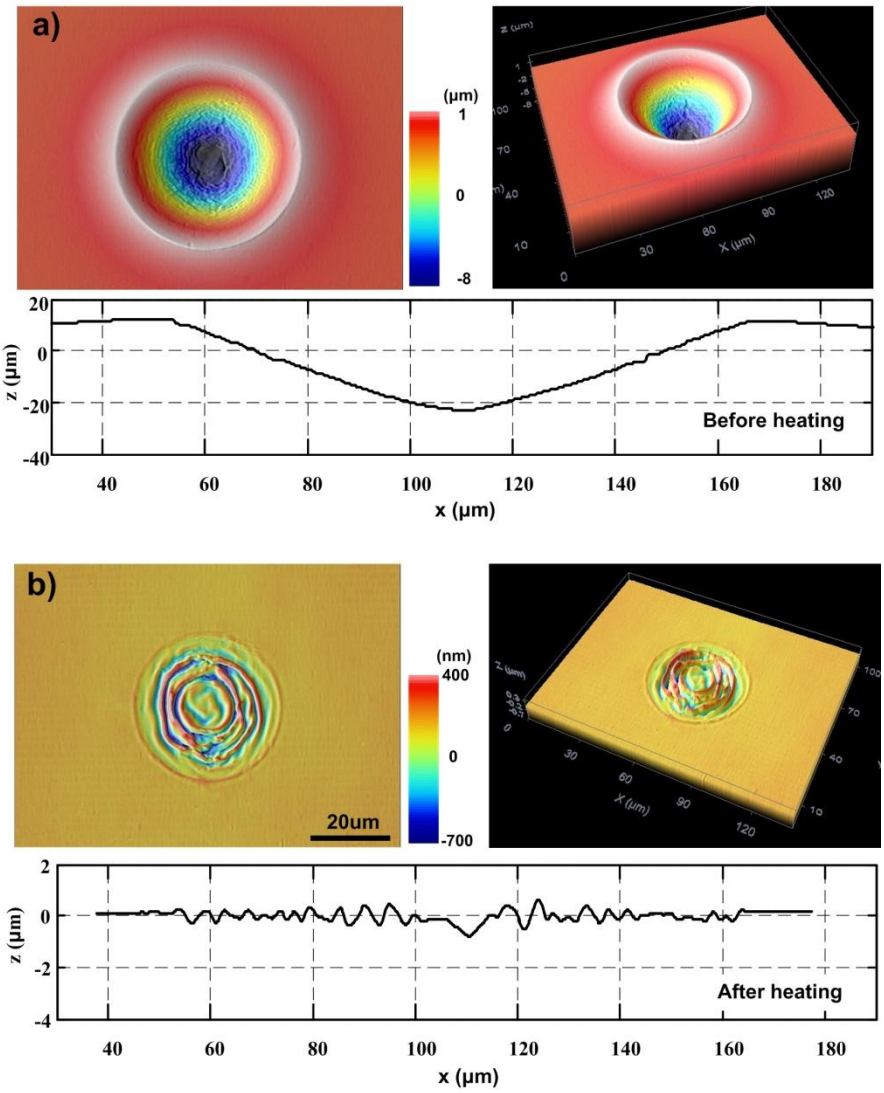

Figure 6.13 Morphology and cross-section of an indent. (a) Before heating; (b) after heating.

We further studied the wrinkling behavior during shape recovery in these indents. As shown in Figure 6.15, in-plane strain mainly results from the longitudinal deformation, which can be calculated according to following equation,

$$\varepsilon = \frac{L}{L_0} - 1 \tag{6.16}$$

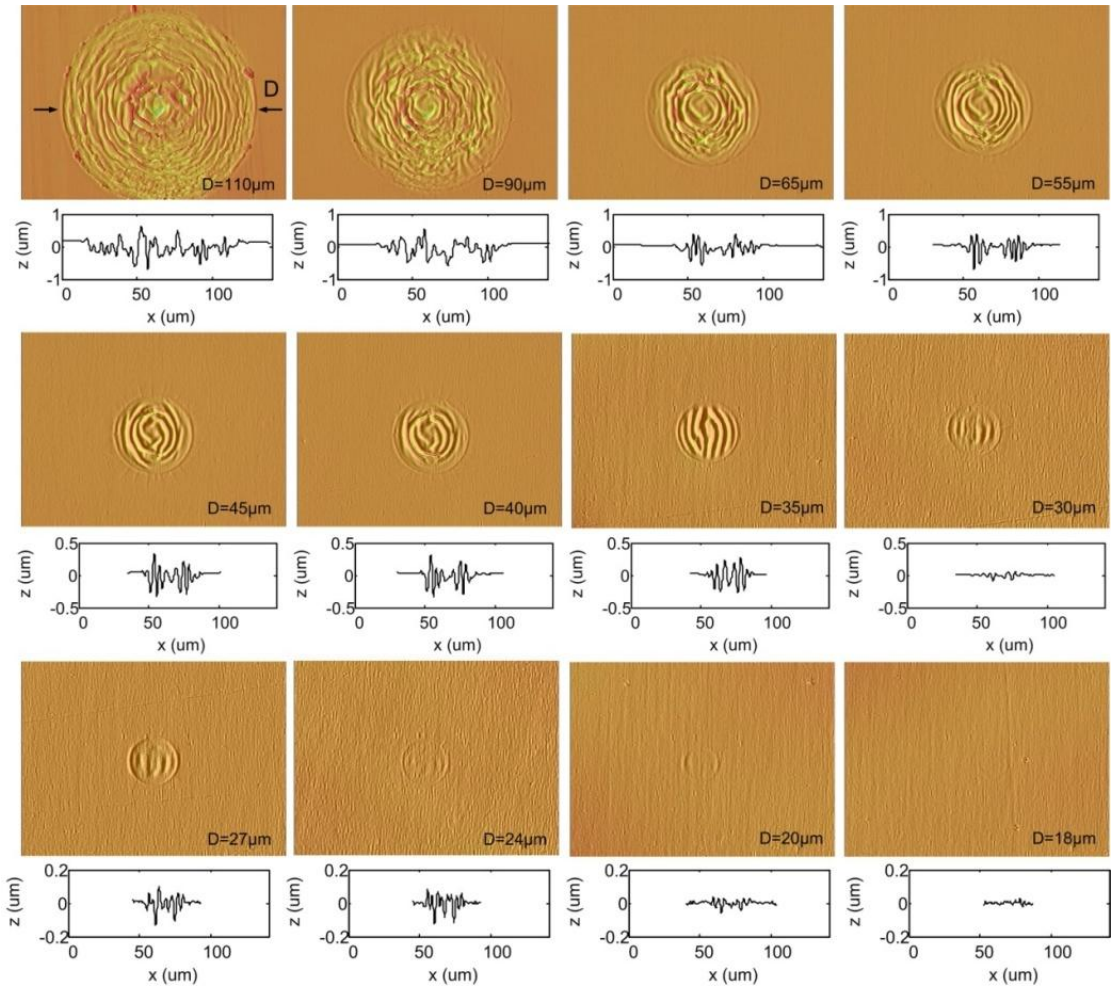

Figure 6.14 Surface morphology after heating to 80^{o}C. Initially, different sized spherical indents were produced before coated with a thin layer of gold.

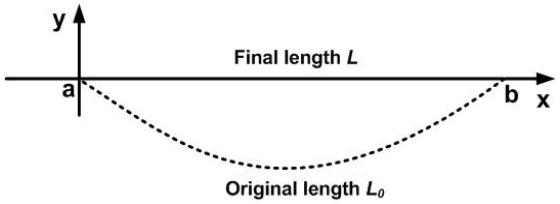

Figure 6.15 Illustration of shape change during shape recovery

According to Eqns. (6.15) and (6.16), the critical size is about 24.4 μm. The theoretical value is in good agreement with the experimental result. During shape recovery, the main

deformation is longitudinal contraction, while the latitudinal deformation is smaller. Therefore, the strain is mainly due to longitudinal deformation, which induces ring-shaped wrinkles perpendicular to the longitudinal direction.

6.1.3 Combination of IPH and wrinkling

Surface patterns — Figure 6.16 illustrates the sample preparation procedure. The samples are initially well polished to achieve a very smooth surface.

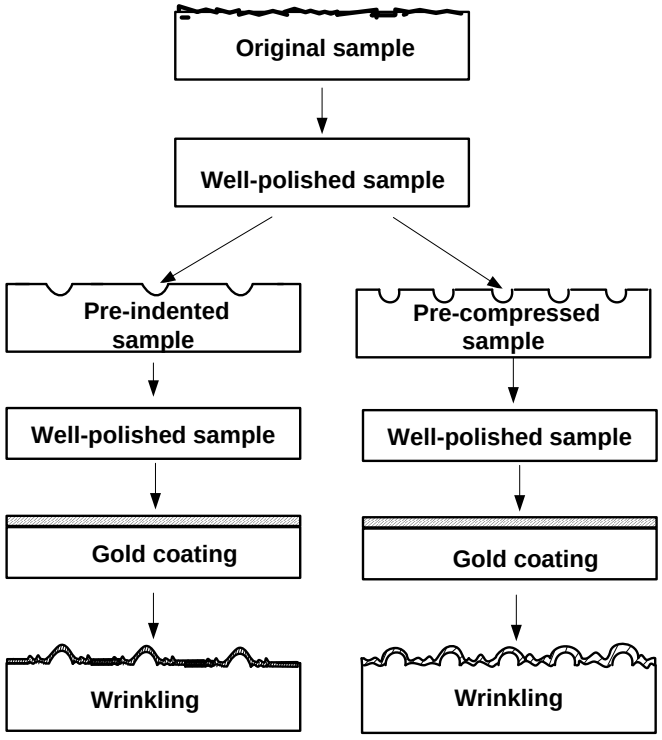

Figure 6.16 Procedure of sample preparation.

The pre-indented samples are prepared using a CSM Micro-hardness tester with a spherical diamond indenter (R=20 μm) at a loading/unloading speed of 0.2 μm/s to a prescribed maximum depth (with a holding time of 10 s after the prescribed maximum

depth is reached). And then these samples are slightly polished following the above mentioned polishing procedure until the indents just disappear.

The pre-compressed samples are produced by compressing one single layer of compactly packed steel balls (with a diameter of 1 mm) atop a piece of well-polished sample at 80 ℃ and a loading speed of 0.05 mm/s to a maximum depth of 0.15 mm. Subsequently, the samples are well polished until the dimple array just disappears.

A thin gold layer about 10s nm in thickness is sputter deposited atop all samples. Finally, these samples are heated to the required temperature and then cooled back to room temperature.

Figure 6.17 shows some typical radial-shaped wrinkles atop well polished pre-indented PS plates after being heated to 100 ℃ and then cooled back to room temperature. Upon heating, part of the deposited thin gold film bends convexly due to the formation of spherical crown within the right underneath polymer substrate (as a result of the shape recovery). As such, within this part, the polymer is in tensile and thus no wrinkle is formed. While within the surround area, it is in contraction in the latitudinal direction after being heated to 100^{o}C, which causes radial-shaped wrinkles.

Figure 6.18 shows typical surface features atop a pre-compressed sample, which was heated to 120 ℃ and then cooled back to room temperature. It can be seen that there are two kinds of patterns, protrusion array and wrinkles. During heating, three types of force/stress arise, namely

- Latitudinal compressive stress due to the formation of protrusion.

- Bending force due to the formation of protrusion.
- Compressive stress due to the TEM.

The first and last ones induce wrinkling; while the second restrains buckling. Within the central area of a protrusion, TEM plays an important role in wrinkle formation. The isotropic compressive stress induced by the TEM contributes to the formation of isotropic wrinkles (Figure 6.18a3 and a6). However, the anisotropic latitudinal strain is larger than the isotropic thermal strain in a area far away from the centre of the protrusion (Figure 6.18a4). Consequently, anisotropic radial-shaped wrinkles are generated within this area (Figure 6.18a1 and a4).

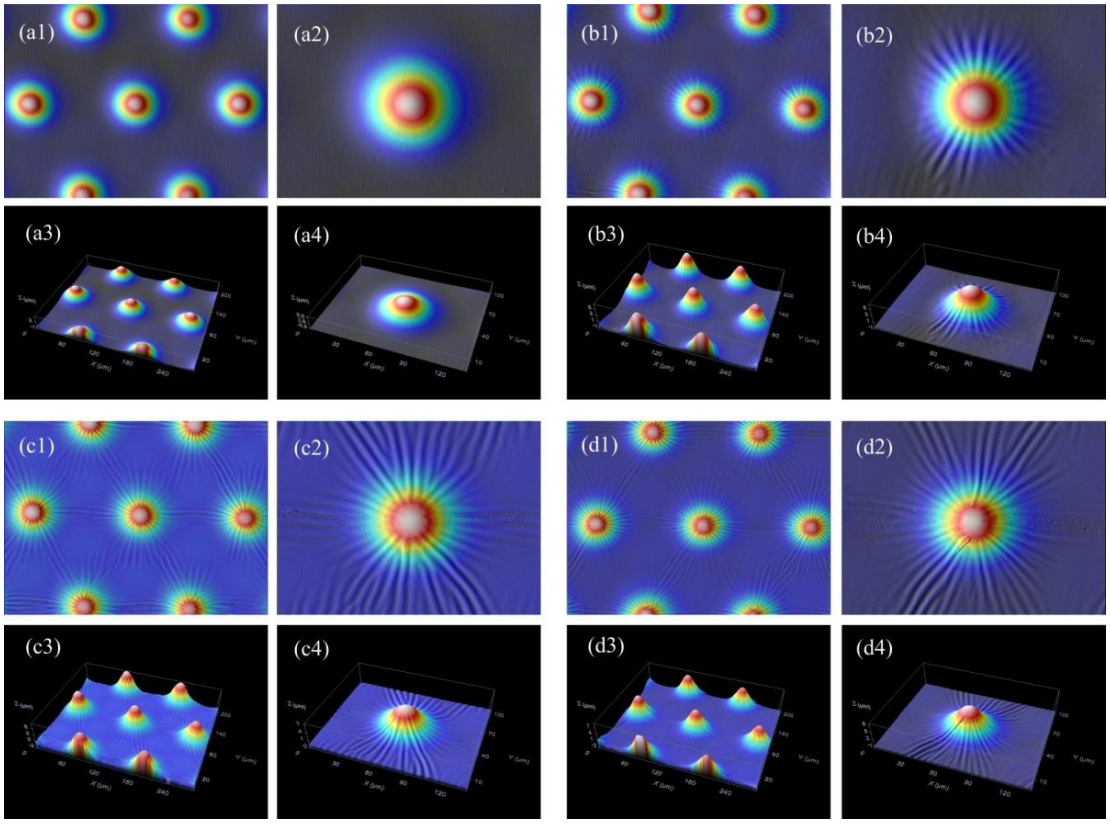

Figure 6.17 Radial-shaped wrinkles.

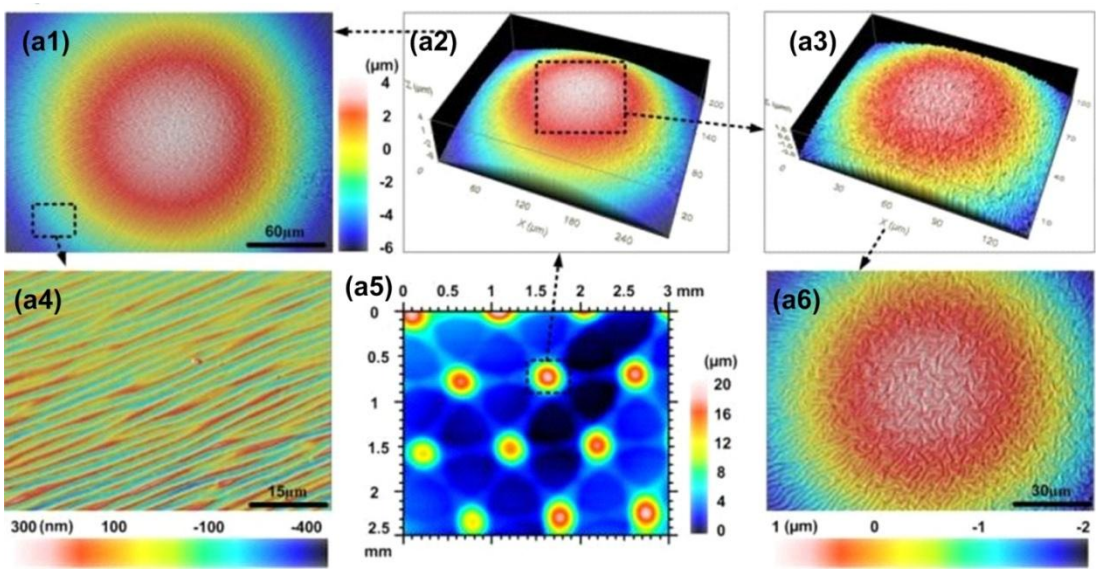

Figure 6.18 Surface patterns produced by a combination of IPH and wrinkling.

Size effect for wrinkling occurrence — Following the IPH approach, different sized protrusions were obtained by indentation using different sized sphericals. The curvatures of the spherical protrusions were measured individually. A thin gold film was sputtered atop these protrusions. The sputtering time was 120 s at a current of 20 mA and voltage of 2 kV. The thickness of the gold thin film was about 30 nm.

The samples were heated in an oven to a series of particular temperatures (between 100 ℃ and 160 ℃ in an increasing order) and cooled in air. After each heating/cooling cycle, surface morphology of the sample was examined using the Confocal imaging profiler to check the appearance of wrinkles. Figure 6.19 shows the surface feature before and after heating to 120 ℃. Figure 6.20 reveals the surface morphology of the gold layer atop different sized spherical protrusions after heated to 130 ℃. We can clearly see that isotropic wrinkles may appear atop the spherical SMP protrusions after heating only if the size of protrusion is large enough.

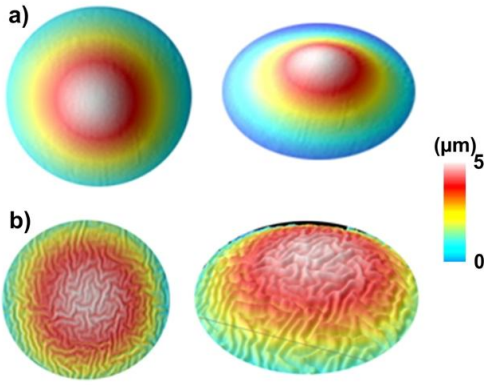

Figure 6.19 Surface feature atop a protrusion. (a) Before heating; (b) after heating.

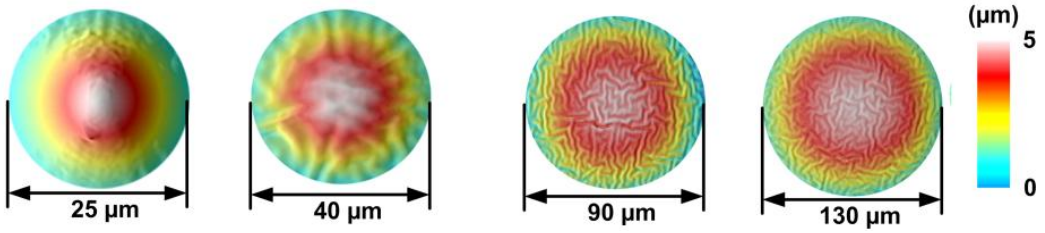

Figure 6.20 Surface morphology after heated to 130 ℃.

The relationship between radius of protrusion, *R*, and critical heating temperature for wrinkling was experimentally investigated and shown in Figure 6.21 (symbols). It clearly shows the influence of protrusion size on the critical heating temperature for wrinkling. Higher temperatures are required for wrinkles to occur in smaller sized protrusions.

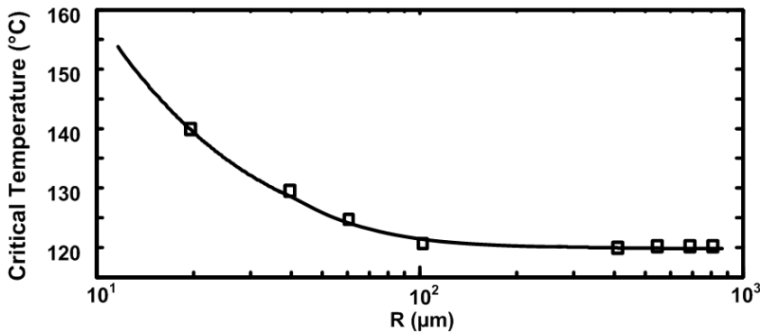

Figure 6.21 Effect of radius of protrusion on critical heating temperature for wrinkling. Symbols: experimental results; curve: data-fitting.

Figure 6.22 further reveals the relationship between critical wavelength, λ_c, and radius of protrusion (experimentally measured). It is clear that at $R > 100$ μm, λ_c is about a constant. At $R < 100$ μm, λ_c decreases dramatically with the decrease of R.

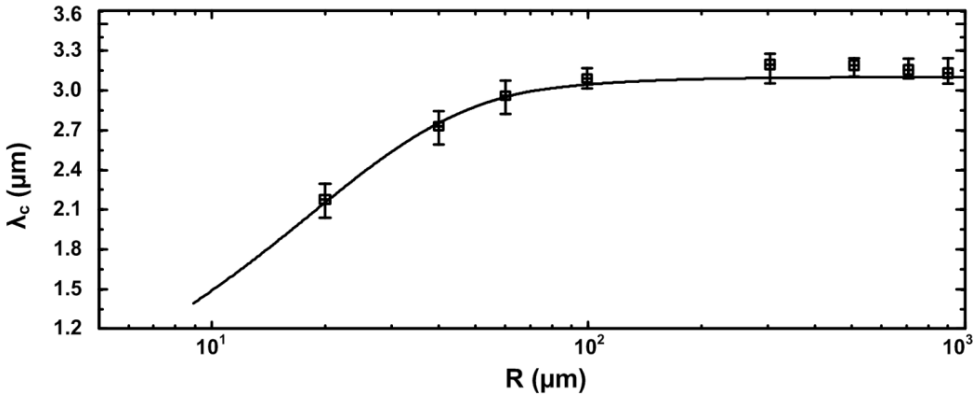

Figure 6.22 Relationship between R and λ_c. Symbols: experimental results (with derivation); curve: data-fitting.

6.2 Chemo-responsive SME for surface patterning

In above section, different thermo-responsive surface patterning methods are presented. This section discusses a chemo-responsive surface patterning method, namely, pre-straining enhanced penetration (PSEP) based micro-protrusive patterning (PSEP-MPP) method, which can be utilized for microlens array (MLA) fabrication.

Figure 6.23 reveals the detailed procedure of PSEP-MPP method and the resulted different micro-protrusive patterns atop PMMA. As we can see, there are only two major steps. In the first step (mechano-process) (Figure 6.23a), local deformation (pre-straining) atop PMMA is conducted by means of either micro-indentation using, for instance, a micro-hardness tester or an embossing method using a pre-patterned mold (e.g., an array of packed steel/glass balls). After this process, local plastic deformation (an indent with a size of w_r and depth of h_r) is introduced into the polymer, and thus PMMA is locally pre-

strained. In the second step (chemo-process) (Figure 6.23b), PMMA is immersed into ethanol (95% concentration) at room temperature (20-25°C). Protrusive pattern(s) (a protrusion with a size of w_f and height of h_f) is resulted. Usually, $w_f \approx 2w_r$, and $h_f \approx 2h_r$. Some typical experimental results are presented in Figure 6.23c.

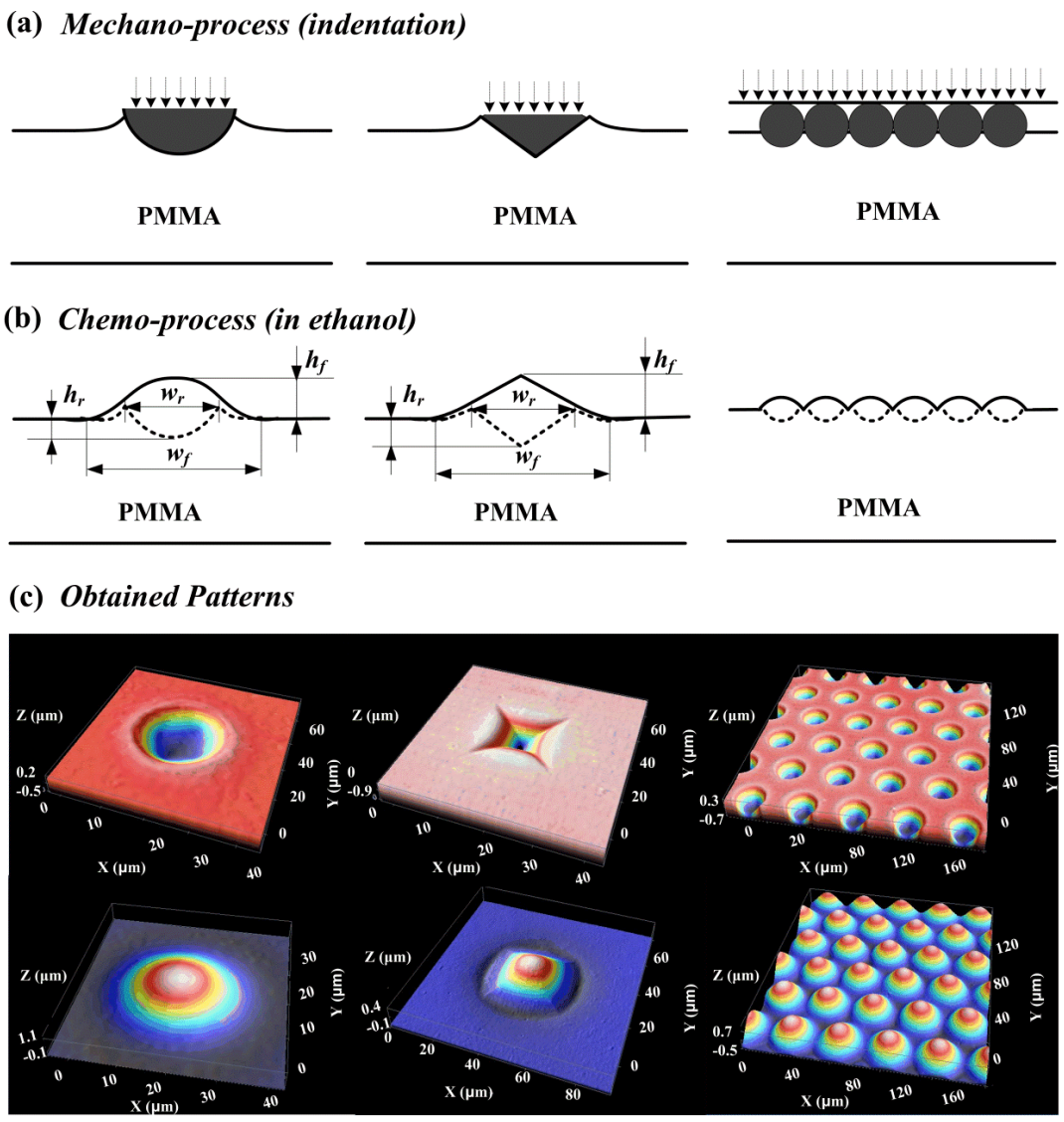

Figure 6.23 Schematic procedure of PSEP patterning method and fabricated patterns. (a) Mechano-process: micro-indentation with different indenters or embossing with a patterned mold; (b) chemo-process: local deformed PMMA sample was immersed into ethanol; (c) obtained patterns. Top one is surface image after indentation. Bottom is surface image after immersion in ethanol for 24 hours.

It is apparent that that the resulted protrusive pattern is a replicate of the indented/embossed patterns. These protrusive patterns can be well controlled by tailoring the exact parameters in both mechano-process and chemo-process. For instance, by using different shaped indenters or molds, different shaped protrusions can be fabricated; by forming different patterns of indent array, different protrusive patterns can be produced; by applying different compressive loads to vary the size of resultant protrusions; and by controlling the ethanol absorption time to modify the shape/dimension of protrusions.

This simple two-step method can be utilized for MLAs fabrication [206]. Refer to Figure 6.24, first, two indent arrays with different pattern/density are fabricated atop PMMA (Figure 6.24a); and then the PMMA samples are immersed into room temperature ethanol for 9 hours, which results in MLAs with different patterns (Figure 6.24b). Cross-sectional view of indents/protrusions is presented in Figure 6.24(c1) for comparison. These lenses are well-ordered, densely *packed* and have an individual size of about 40 μm (w_f) and a height (h_f) of about 1 μm (refer to Figure 6.23 for the definitions of w_f and h_f). Figure 6.24(c2) further reveals the evolution from indent to protrusion after being immersed into ethanol for different periods of time. As indentation is conducted at room temperature, so that PMMA is hard, the resultant spherical indent is actually pile-up [207]. Upon immersing into ethanol, pile-up grows gradually before spherical protrusion is finally formed (after about 4 hours immersion) and then grows (a useful phenomenon, which can be used to control the curvature, conic constant and focus length of lens). As we can see, after 9 hours, w_f is about 40 μm, which is about twice as w_r, while h_f is about 1 μm, which is about 0.5 times larger than h_r.

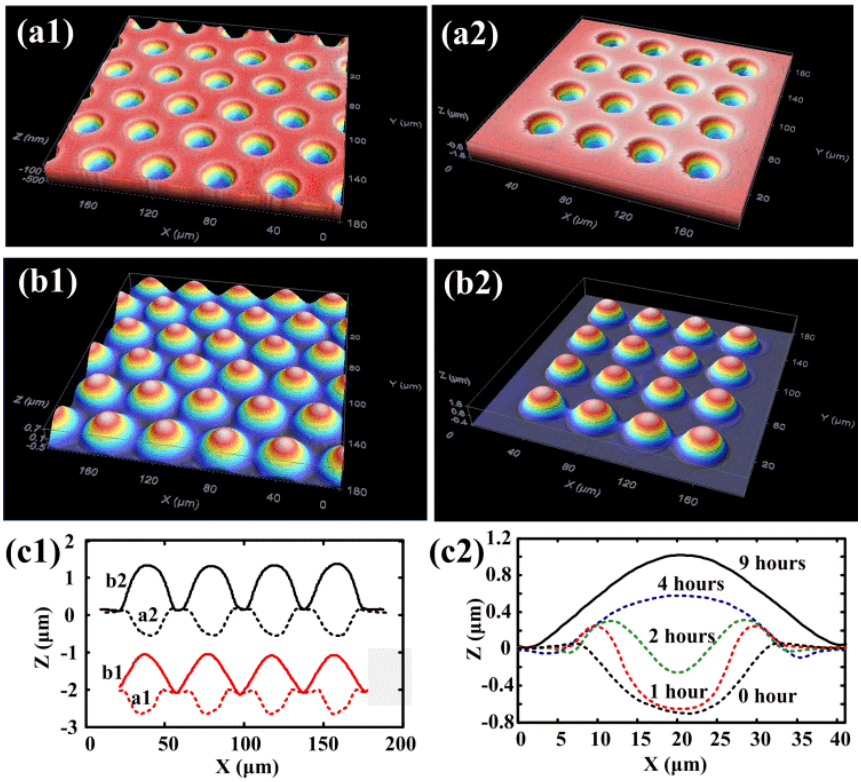

Figure 6.24 MLAs and surface profile.

Since this method is based on swelling of PMMA upon immersing into ethanol, desorption of ethanol may be an issue which brings the reliability of these MLAs into question. To address this point, different sized spherical lenses were fabricated on different PMMA samples following the above two-step method and then put inside an oven of 25 ℃ or 60 ℃.

Figure 6.25(a1) reveals the surface profile of an indent array, in which three different sized indents were made by a 20 μm spherical under three different maximum loads (namely, 150 mN, 100 mN and 80 mN, respectively).

Figure 6.25(a2) reveals the surface profile of MLA after immersion in ethanol for 24 hours.

Figure 6.25(a3) and (a4) present two typical MLA surface profiles after being kept inside an oven for thermal stability test.

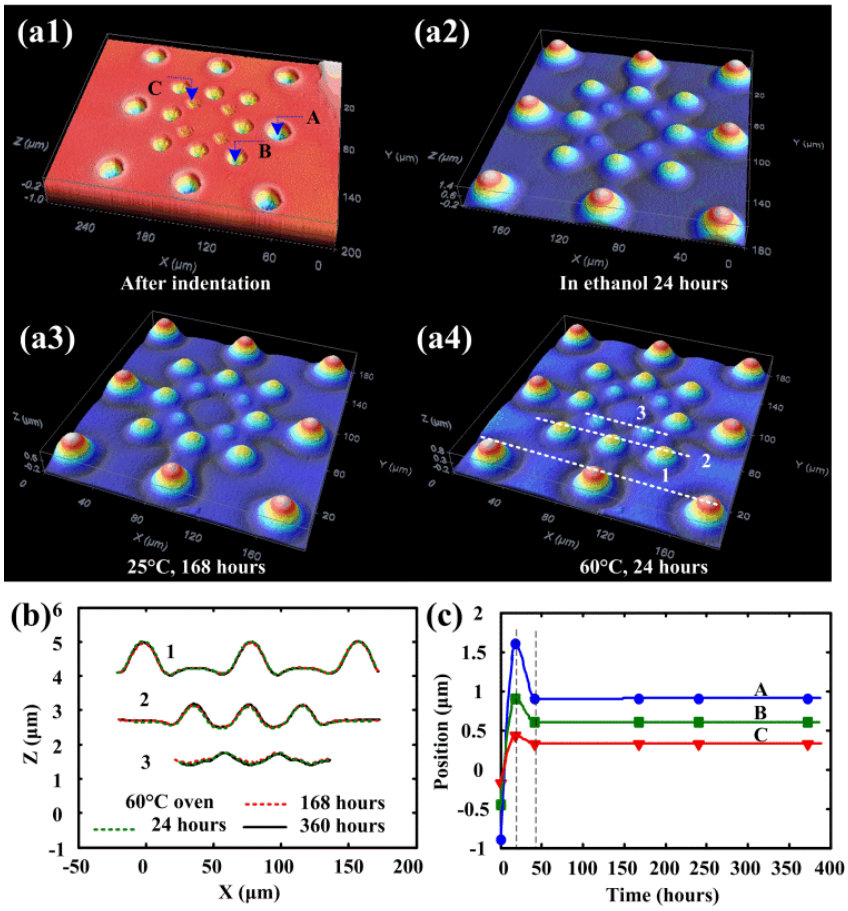

Figure 6.25 Thermal stability of MLAs.

It is found that MLAs are stabilized after 168 hours in a 25 ℃ oven, while it takes 24 hours if the oven temperature is set to be 60 ℃. Figure 6.25(b) compares the profiles of lenses after 24, 168 and 360 hours inside 60 ℃ oven. It is concluded that all three sized lens arrays are stablized after 24 hours at 60 ℃.

Figure 6.25(c) plots the evolution of the center points of three different sized indents/protrusions (depth/height) against time in the whole process (i.e., after indentation,

immersion in ethanol and placed in 60 ℃ oven). It can be seen that there are three major stages during the whole process. The first is the gradual formation of micro lens during immersion into ethanol (from indent to protrusion within 24 hours). Relaxation due to desorption of ethanol is followed (decreasing in protrusion height inside a 60^{o}C oven for 24 hours). After this, MLA becomes stable (no visible change in height in 60^{o}C air after 360 hours). After being put into 60^{o}C oven for 24 hours, stabilized lens has a diameter of 39.95 ± 0.55 μm, center-to-center distance of 40 μm and a sag height of 0.8 ± 0.02 μm (Figure 6.24b1).

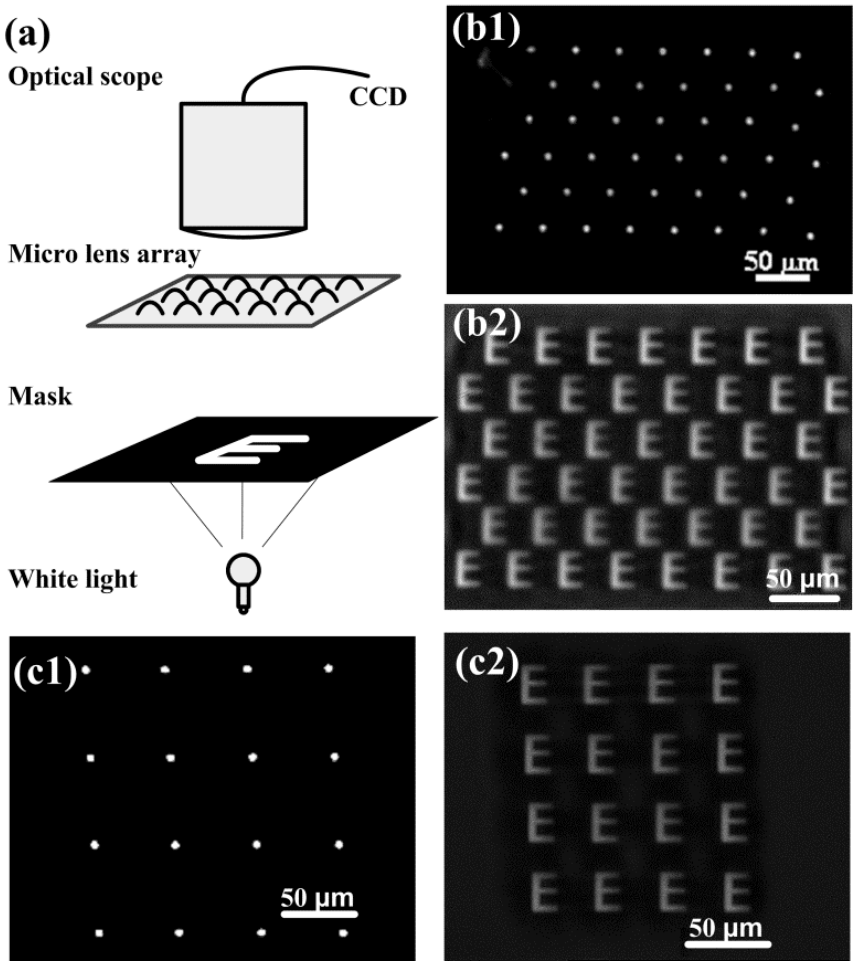

Figure 6.26 Projection experiment and results.

Projection experiment has been conducted on stabilized MLAs. Refer to Figure 6.26(a) for the illustration of the experimental setup. The optical scope is a microscope (Axiotech 100 HD, Zeiss). A PMMA MLA is placed atop a stage and illuminated with white light from bottom through a mask with a letter E (size 12×18 mm) in the middle. The projected image at the top is recorded by a CCD system. Figure 6.26(b) and (c) shows the focus spot and projected images through two different MLAs (as shown in Figure 6.24b1 and b2). The focus length of these MLAs was measured to be 500 μm by this optical microscope system. It can be seen that letter Es are clearly projected.

6.3 Combination of thermo-/chemo-responsive SME for surface patterning

Above mentioned thermo-/chemo-responsive SMEs can be combined together to fabricate more complex surface patterns. In this section, we demonstrate two applications, namely, reversible surface pattern and patterning atop a curved substrate.

6.3.1 Reversible surface pattern

Figure 6.27 illustrates the procedure of the formation of reversible wrinkles.

Following the same procedure described in Section 6.2, protrusion(s) is generated atop a pre-stretched PMMA sample due to the PSEP effect.

Then, the sample is heated at high temperatures (> T_g of PMMA). Wrinkles are obtained due to the compressive stress generated during shape recovery of PMMA.

Subsequently, we immerse the wrinkled sample into ethanol again. The wrinkled sample swells again and thus wrinkles disappear due to ethanol absorption induced swelling in PMMA. An elliptical shaped protrusion is resulted.

In the next step, the sample is re-heated again and wrinkles re-appear. Such a procedure can be repeated again and again.

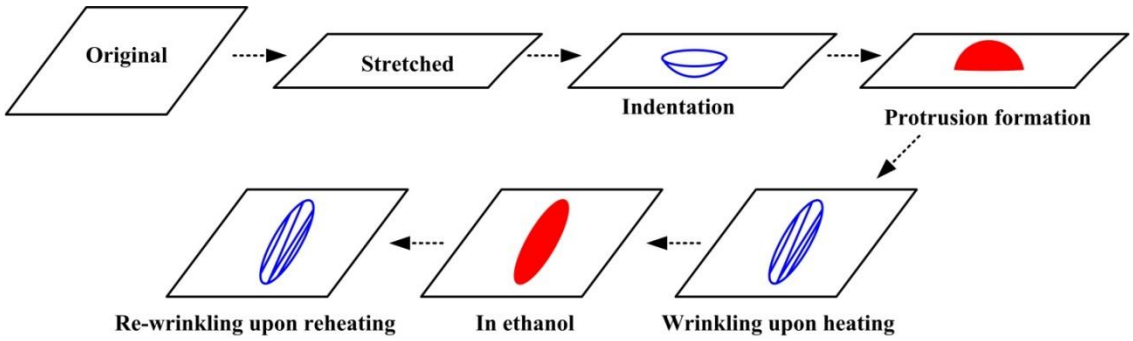

Figure 6.27 Fabrication of reversible surface pattern.

Figure 6.28 presents a typical reversible wrinkle pattern. Firstly, a piece of PMMA plate with a thickness of 1 mm was pre-stretched to a maximum of strain 20% at 140°C at a strain rate of $0.001s^{-1}$. Then, indent(s) was produced atop it. Subsequently, as obtained sample was immersed into ethanol for 12 hours, and protrusion(s) was formed due to the PSEP effect. In next step, the sample was heated at 140°C for 1 minute.

Wrinkled pattern was generated due to the shape recovery of the stretched sample (Figure 6.28a). After wrinkling, the sample was immersed into ethanol again for swelling. After 48 hours, the wrinkled pattern disappeared (Figure 6.28b) and as expected elliptical shape protrusive lenses were found. If the sample was reheated again, swollen sample wrinkled again (Figure 6.28c).

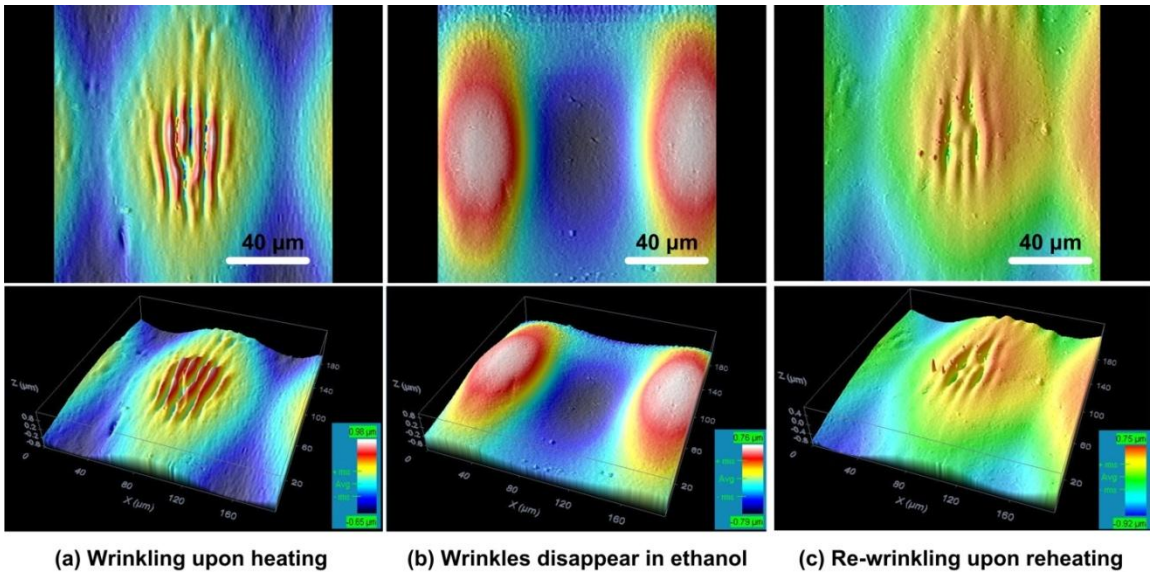

Figure 6.28 Reversible wrinkles.

6.3.2 Patterning atop curved substrate

We propose a novel 3-D surface patterning method for PMMA [193], which is based on the thermo-/chemo-responsive SME in PMMA. This method is simpler and easier to implement as compared with many existing methods, such as lithography, self-assembly and imprinting [208-211], and has the advantage of precise control of the patterned area, which is lack of in current wrinkling based patterning methods [198]. Since PMMA is a conventional optical polymer, this method is potentially applicable to fabricate 3-D artificial compound eye (insect eye) in optics applications.

Figure 6.29 schematically illustrates the fabrication procedure of 3-D surface patterning. This patterning method is actually based on two kinds of phenomena. One is PSEP effect, and the other is the SME. Typically, a 3-D surface pattern can be fabricated in four steps as follows,

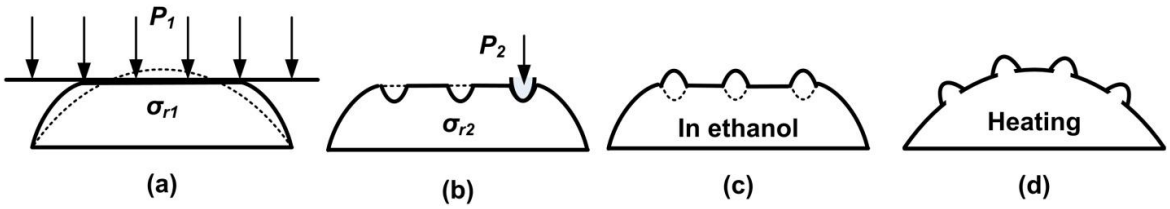

Figure 6.29 3-D surface patterning.

Step 1: A hemi-spherical (or hemi-cylindrical) PMMA sample is compressed to a maximum load of P_1, using, for instance, an Instron at room temperature or high temperatures. After compression, a residual stress field, σ_{r1}, is introduced into the deformed sample, as shown in Figure 6.29(a).

Step 2: A micro-indents array is fabricated atop the pre-compressed PMMA sample using a micro indenter (e.g., Micro-Hardness tester, CSM Instrument) with a maximum indentation load of P_2. After indentation an additional residual stress field, σ_{r2}, is generated around these indents, as shown in Figure 6.29(b).

Step 3: After indentation, the PMMA sample is immersed into room temperature ethanol and thus swelling occurs. Due to the PSEP effect, if $\sigma_{r2} >> \sigma_{r1}$, a micro-protrusion array can be formed, as shown in Figure 6.29(c).

Step 4: After formation of micro-protrusion array, the PMMA sample is placed into an oven for ethanol evaporation. Usually, a stable protrusion array is obtained after heating at 60 ℃ for 24 hours. Subsequently, the PMMA sample is heated to 120 ℃ for 1~5 minutes, so that a stable 3-D surface pattern is obtained, as shown in Figure 6.29(d).

Figure 6.30 shows two typical micron-protrusion arrays (4×2 and 5×5) atop a PMMA cylindrical substrate following this procedure. In the first step, a 5 mm diameter PMMA

rod was compressed by 1.5 mm at a loading rate of 0.005 mm/s at room temperature. Next, a 4×2 indent array was fabricated using a 20 μm radius spherical with a maximum load of 0.5 N at a loading/unloading rate of 15 mN/s and with a 10s holding period. The 5×5 indent array was fabricated using the same indenter and had the same holding period, but the maximum load was 0.15 N and the applied loading/unloading rate was 5 mN/s. In the third step, the pre-indented PMMA samples were immersed into room temperature ethanol. Due to the PSEP effect, protrusions were formed after 12 hours in ethanol. Finally, the samples were heated to 60 ℃ for 24 hours for ethanol desorption, and then the stable samples were heated to 120 ℃ for 1 min. Due to the SME, the flattened PMMA samples recovered their original cylindrical shape. A surface scanning instrument (Talyscan 150 3-D, Taylor Hobson) was used to obtain their 3-D surface profiles, as shown in Figure 6.30. The size of one single protrusion in Figure 6.30(a) is about 200 ± 2 μm in width and 40 ± 0.5 μm in height, while that in Figure 6.30(b) is about 100 ± 1 μm in width and 7 ± 1 μm in height.

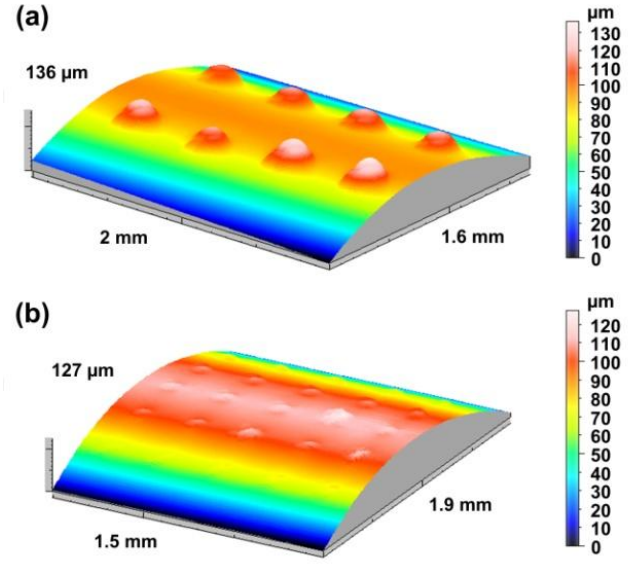

Figure 6.30 3-D surface patterns atop PMMA. (a) 4×2; (b) 5×5 protrusions array.

The obtained PMMA pattern can be used as a 3-D artificial compound eye. Compound eye is very efficient for local and global motion analysis over a large field-of-view (FOV) [206]. The optical performance of the 3-D PMMA pattern was characterized using an optical microscope system (Axiotech 100 HD, Carl Zeiss). A 3-D patterned PMMA sample was fixed atop the sample stage and illuminated with white light through a mask, which is made of a black paper with a word "NTU" cut out of it. Miniaturized image of NTU was projected through the 3-D PMMA pattern and captured by a CCD system. Figure 6.31 shows projected image of NTU atop these protrusions. The projected images atop the central protrusions are clear since the light was focused on them, and the rest which are away from the center are blur. Each protrusion has its own focus spot that depends on its exact position. This is exactly the special feature of a 3-D compound eye.

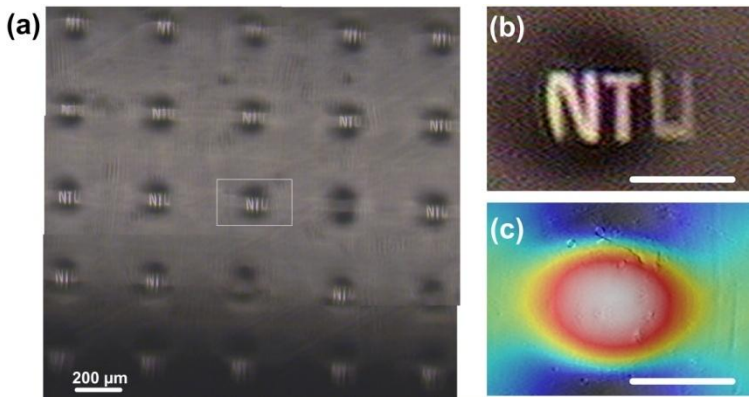

Figure 6.31 5×5 protrusions array atop a 5 mm diameter PMMA rod. (a) Projected image; (b) zoom-in view of one central protrusion as marked in (a); (c) 3-D surface image of a single protrusion. Scale bar in (b) and (c) is 50μm.

6.4 Summary

We propose several novel, simple and cost-effective surface patterning methods utilizing the thermo- and chemo-responsive SMEs in polymeric materials. Different micro/nano-

scale surface patterns are obtained by these methods. The size and shape of the patterns are well controllable. By combining these two SMEs, reversible pattern and 3-D pattern can be easily achieved.

Chapter 7 Conclusions and future work

7.1 Conclusions

Based on the working mechanisms, we classified the shape memory effect (SME) in shape memory materials (SMMs) into three categories, namely dual-state mechanism (DSM), dual-component mechanism (DCM), and partial-transition mechanism (PTM). From these three categories, the concept of advanced shape memory technology (ASMT) was proposed to enable the SME in materials, to design/synthesize new SMMs with tailored features, and to optimize the SME in materials.

According to the concept of ASMT, a generic 3-D model (followed *phase* transition approach) was developed to simulate the shape memory behavior in polymeric SMMs. This model was verified by the experimental results of the thermo-responsive SME in PTM and DCM based polymeric SMMs. It was also applied for optimization of the SME.

The thermo-/chemo-responsive SME in PMMA were systematically studied by experiments and simulation. Chemo-responsive SME and pre-straining enhanced penetration (PSEP) in PMMA were focused in experimental investigation. The temperature memory effect (TME) and reversible plasticity (RP)-SME were focused in simulation using the above mentioned 3-D model. We further gave a brief discussion on simulation of chemo-responsive SME in PMMA by this model.

Based on above discussed thermo-/chemo-responsive SME, we proposed several novel, simple and cost-effective surface patterning methods. Different micro/nano-sized surface

patterns were obtained by these methods. The size and shape of the patterns were well controllable. Reversible pattern and 3-D pattern were achieved.

In summary, there are four main contributions in this project.

(1) A new approach to classify all of SMMs is presented.
(2) The concept of ASMT is proposed. Utilizing ASMT, we can enable SME in materials, design new SMMs with required function and tailored features, and optimize the SME.
(3) A generic 3-D model is developed for the thermo-/chemo-responsive SME in polymeric SMMs. This model is applicable for PTM, DCM and DSM based SMMs.
(4) Based on the thermo-/chemo-responsive SME individually or combined, some novel, simple and cost-efficient surface patterning methods are developed. Reversible surface features and 3-D patterns are demonstrated.

7.2 Future work

This project provides a sketch of ASMT, and may serve as the start point for further development, since ASMT is really a very big topic. The focus here is limited on polymeric materials only, while the fundamentals are applicable to many other types of materials as well.

For simplicity, in numerical simulation, all time-dependent effects are ignored, so that the predicted R_r and σ_r are normally higher than the experimental results. The proposed

simulation model should be further developed to be more precise by coupling of unsteady behavior (relaxation and creeping).

Only one application, namely surface patterning, was studied in this dissertation. Since the SME is a generic phenomenon in many materials, we should be able to apply the effect in many other applications as well.

References

1. Liu C., Qin H., and Mather P.T., Review of progress in shape-memory polymers. *Journal of Materials Chemistry*, 2007. 17(16): 1543-1558.
2. Dietsch B. and Tong T., A review - Features and benefits of shape memory polymers (SMPs). *Journal of Advanced Materials*, 2007. 39(2): 3-12.
3. Havens E., Snyder E., and Tong T., Light-activated shape memory polymers and associated applications. *Proc. SPIE*, 2005. 5762(1): 48-54.
4. Ratna D. and Karger-Kocsis J., Recent advances in shape memory polymers and composites: a review. *Journal of Materials Science*, 2008. 43(1): 254-269.
5. Gunes I.S. and Jana S.C., Shape memory polymers and their nanocomposites: A review of science and technology of new multifunctional materials. *Journal of Nanoscience and Nanotechnology*, 2008. 8(4): 1616-1637.
6. Mather P.T., Luo X.F., and Rousseau I.A., Shape memory polymer research. *Annual Review of Materials Research*, 2009. 39: 445-471.
7. Lendlein A., Shape-memory Polymers. 2010: Springer-Verlag Berlin Heidelberg.
8. Sun L., et al., Stimulus-responsive shape memory materials: A review. *Materials & Design*, 2012. 33: 577-640.
9. Aschwanden M. and Stemmer A., Polymeric, electrically tunable diffraction grating based on artificial muscles. *Optics Letters*, 2006. 31(17): 2610-2612.
10. Haertling G.H., Ferroelectric ceramics: history and technology. *Journal of the American Ceramic Society*, 1999. 82(4): 797-818.
11. Otsuka K. and Wayman C.M., Shape memory materials. 1998, New York: Cambridge University Press. xiv, 284.
12. Miyazaki S., Fu Y.Q., and Huang W.M., Thin film shape memory alloys: fundamentals and device applications. 2009, New York: Cambridge University Press. xxv, 459.
13. Behl M., et al., Shape-memory capability of binary multiblock copolymer blends with hard and switching domains provided by different components. *Soft Matter*, 2009. 5(3): 676-684.
14. Luo X. and Mather P.T., Triple-Shape Polymeric Composites (TSPCs). *Advanced Functional Materials*, 2010. 20(16): 2649-2656.
15. Roy D., Cambre J.N., and Sumerlin B.S., Future perspectives and recent advances in stimuli-responsive materials. *Progress in Polymer Science*, 2010. 35(1-2): 278-301.

16. Xie T., Tunable polymer multi-shape memory effect. *Nature*, 2010. 464(7286): 267-270.
17. DiOrio A.M., et al., A functionally graded shape memory polymer. *Soft Matter*, 2011. 7(1): 68-74.
18. Fan K., et al., Water-responsive shape memory hybrid: Design concept and demonstration. *eXPRESS Polymer Letters*, 2011. 5(5): 409-416.
19. He Z.W., et al., Remote controlled multishape polymer nanocomposites with selective radiofrequency actuations. *Advanced Materials*, 2011. 23(28): 3192-3196.
20. Hsu L., Weder C., and Rowan S.J., Stimuli-responsive, mechanically-adaptive polymer nanocomposites. *Journal of Materials Chemistry*, 2011. 21(9): 2812-2822.
21. Kumpfer J.R. and Rowan S.J., Thermo-, photo-, and chemo-responsive shape-memory properties from photo-cross-linked metallo-supramolecular polymers. *Journal of the American Chemical Society*, 2011. 133(32): 12866-12874.
22. Zhao Y., et al., Buckling of poly(methyl methacrylate) in stimulus-responsive shape recovery. *Applied Physics Letters*, 2011. 99(13).
23. Kawakami H., Kanda N., and Nanzai Y., Deformation recovery of largely deformed epoxy resin. *Materials Science Research International*, 2001. 7(4): 243-248.
24. Kawakami H., Yamanaka H., and Nanzai Y., Thermally stimulated recovery of plastic strain in crosslinked and uncrosslinked epoxy/amine systems. *Polymer*, 2005. 46(25): 11806-11813.
25. Willett J.L., Humidity-responsive starch-poly(methyl acrylate) films. *Macromolecular Chemistry and Physics*, 2008. 209(7): 764-772.
26. Chaunier L. and Lourdin D., The Shape Memory of Starch. *Starch-Starke*, 2009. 61(2): 116-118.
27. Vechambre C., Chaunier L., and Lourdin D., Novel Shape-Memory Materials Based on Potato Starch. *Macromolecular Materials and Engineering*, 2010. 295(2): 115-122.
28. Chaunier L., Vechambre C., and Lourdin D., Starch-based foods presenting shape memory capabilities. *Food Research International*, 2012. 47(2): 194-196.
29. Washburn J., Experimental observations concerning the collapse of dislocation loops during annealing. *Transactions of the American Institute of Mining and Metallurgical Engineers*, 1956. 206(2): 189-191.
30. Mendez J., et al., Bioinspired mechanically adaptive polymer nanocomposites with water-activated shape-memory effect. *Macromolecules*, 2011. 44(17): 6827-6835.

31. Chang B.T.A. and Li J.C.M., Indentation recovery of atactic polystyrene. *Journal of Materials Science*, 1980. 15(6): 1364-1370.
32. Chang B.T.A. and Li J.C.M., Recovery of compressive strain in atactic polystyrene. *Journal of Materials Science*, 1981. 16(4): 889-899.
33. Dismore P.F. and Statton W.O., Chain folding in oriented 66-nylon fibers. *Journal of Polymer Science Part B-Polymer Letters*, 1964. 2(12P): 1113-1116.
34. Dumbleton J.H., Chain folding in oriented Poly(Ethylene Terephthalate). *Journal of Polymer Science Part a-2-Polymer Physics*, 1969. 7(4pa2): 667-674.
35. Statton W.O., Koenig J.L., and Hannon M., Characterization of chain folding in poly(ethylene terephthalate) fibers. *Journal of Applied Physics*, 1970. 41(11): 4290-4295.
36. Wilson M.P.W., Shrinkage and chain folding in drawn poly(ethylene terephthalate) fibres. *Polymer*, 1974. 15(5): 277-282.
37. Crystal R.G. and Hansen D., Repeated cold drawing and annealing of polypropylene. *Journal of Applied Physics*, 1967. 38(8): 3103-3108.
38. Ito E., Horie T., and Kobayashi Y., Thermal shrinkage of drawn polystyrene. *Journal of Applied Polymer Science*, 1978. 22(11): 3193-3201.
39. Wing G., et al., Time dependent response of polycarbonate and microcellular polycarbonate. *Polymer Engineering & Science*, 1995. 35(8): 673-679.
40. Yang F.Q. and Li J.C.M., Impression recovery of PMMA. *Journal of Materials Research*, 1997. 12(10): 2809-2814.
41. Yang F.Q., Zhang S.L., and Li J.C.M., Impression recovery of amorphous polymers. *Journal of Electronic Materials*, 1997. 26(7): 859-862.
42. Kung T.M. and Li J.C.M., Recovery processes in amorphous polymers. *Journal of Materials Science*, 1987. 22(10): 3620-3630.
43. Quinson R., et al., Beta-relaxations and Alpha-relaxations in poly(methyl-methacrylate) and polycarbonate - Nonlinear anelasticity studies by antistress relaxation. *Polymer*, 1995. 36(4): 743-752.
44. Quinson R., et al., Components of non-elastic deformation in amorphous glassy polymers. *Journal of Materials Science*, 1996. 31(16): 4387-4394.
45. Basit A., L'Hostis G., and Durand B., Multi-shape memory effect in shape memory polymer composites. *Materials Letters*, 2012. 74: 220-222.
46. Xie T., Recent advances in polymer shape memory. *Polymer*, 2011. 52(22): 4985-5000.

47. Zotzmann J., et al., Reversible triple-shape effect of polymer networks containing polypentadecalactone- and poly(ε-caprolactone)-segments. *Advanced Materials*, 2010. 22(31): 3424-3429.
48. Thorsten P., Triple-shape properties of a thermoresponsive poly(ester urethane). *Smart Materials and Structures*, 2010. 19(1): 015006.
49. Sun L. and Huang W.M., Mechanisms of the multi-shape memory effect and temperature memory effect in shape memory polymers. *Soft Matter*, 2010. 6(18): 4403-4406.
50. Pretsch T., Triple-shape properties of a thermoresponsive poly(ester urethane). *Smart Materials and Structures*, 2010. 19(1): 015006.
51. Volynskii A.L. and Bakeev N.F., Structural aspects of inelastic strain in glassy polymers. *Polymer Science Series C*, 2005. 47: 74-100.
52. Volynskii A.L. and Bakeev N.F., Structural aspects of deformation of amorphous polymers. *Russian Chemical Bulletin*, 2005. 54(1): 1-15.
53. Oleinik E.F., et al., Energy storage in cold non-elastic deformation of glassy polymers. *E-Polymers*, 2006.
54. Baer G., et al., Shape-memory behavior of thermally stimulated polyurethane for medical applications. *Journal of Applied Polymer Science*, 2007. 103(6): 3882-3892.
55. Sokolowski W., et al., Medical applications of shape memory polymers. *Biomedical Materials*, 2007. 2(1): S23-S27.
56. Yakacki C.M., et al., Strong, tailored, biocompatible shape-memory polymer networks. *Advanced Functional Materials*, 2008. 18(16): 2428-2435.
57. Sun L. and Huang W.M., Thermo/moisture responsive shape-memory polymer for possible surgery/operation inside living cells in future. *Materials & Design*, 2010. 31(5): 2684-2689.
58. Wischke C. and Lendlein A., Shape-memory polymers as drug carriers - a multifunctional system. *Pharmaceutical Research*, 2010. 27(4): 527-529.
59. Lake M.S. and Campbell D., The fundamentals of designing deployable structures with elastic memory composites. *IEEE Aerospace Conference Proceedings, Vols 1-6*, 2004: 2745-2756.
60. Sokolowski W.M. and Tan S.C., Advanced self-deployable structures for space applications. *Journal of Spacecraft and Rockets*, 2007. 44(4): 750-754.
61. Chiodo J.D., Harrison D.J., and Billett E.H., An initial investigation into active disassembly using shape memory polymers. *Proceedings of the Institution of*

Mechanical Engineers Part B-Journal of Engineering Manufacture, 2001. 215(5): 733-741.

62. Hussein H. and Harrison D., New technologies for active disassembly: using the shape memory effect in engineering polymers. *International Journal of Product Development*, 2008. 6(3): 431-449.
63. Tobushi H., et al., Thermomechanical constitutive modeling in shape memory polymer of polyurethane series. *Journal of Intelligent Material Systems and Structures*, 1997. 8(8): 711-718.
64. Tobushi H., et al., Thermomechanical constitutive model of shape memory polymer. *Mechanics of Materials*, 2001. 33(10): 545-554.
65. Liu Y.P., et al., Thermomechanics of shape memory polymers: Uniaxial experiments and constitutive modeling. *International Journal of Plasticity*, 2006. 22(2): 279-313.
66. Qi H.J., et al., Finite deformation thermo-mechanical behavior of thermally induced shape memory polymers. *Journal of the Mechanics and Physics of Solids*, 2008. 56(5): 1730-1751.
67. Nguyen T.D., et al., A thermoviscoelastic model for amorphous shape memory polymers: Incorporating structural and stress relaxation. *Journal of the Mechanics and Physics of Solids*, 2008. 56(9): 2792-2814.
68. Diani J., Liu Y.P., and Gall K., Finite strain 3D thermoviscoelastic constitutive model for shape memory polymers. *Polymer Engineering and Science*, 2006. 46(4): 486-492.
69. Barot G., Rao I.J., and Rajagopal K.R., A thermodynamic framework for the modeling of crystallizable shape memory polymers. *International Journal of Engineering Science*, 2008. 46(4): 325-351.
70. Chen Y.C. and Lagoudas D.C., A constitutive theory for shape memory polymers. Part I - Large deformations. *Journal of the Mechanics and Physics of Solids*, 2008. 56(5): 1752-1765.
71. Chen Y.C. and Lagoudas D.C., A constitutive theory for shape memory polymers. Part II - A linearized model for small deformations. *Journal of the Mechanics and Physics of Solids*, 2008. 56(5): 1766-1778.
72. Bhattacharyya A. and Tobushi H., Analysis of the isothermal mechanical response of a shape memory polymer rheological model. *Polymer Engineering and Science*, 2000. 40(12): 2498-2510.

73. Morshedian J., Khonakdar H.A., and Rasouli S., Modeling of shape memory induction and recovery in heat-shrinkable polymers. *Macromolecular Theory and Simulations*, 2005. 14(7): 428-434.
74. Barot G. and Rao I.J., Constitutive modeling of the mechanics associated with crystallizable shape memory polymers. *Zeitschrift Fur Angewandte Mathematik Und Physik*, 2006. 57(4): 652-681.
75. Nguyen T.D., et al., Modeling the Relaxation Mechanisms of Amorphous Shape Memory Polymers. *Advanced Materials*, 2010. 22(31): 3411-3423.
76. Gunes I.S., Cao F., and Jana S.C., Effect of thermal expansion on shape memory behavior of polyurethane and its nanocomposites. *Journal of Polymer Science Part B-Polymer Physics*, 2008. 46(14): 1437-1449.
77. Hasan O.A. and Boyce M.C., Energy-stroage during inelastic deformation of glassy-polymers. *Polymer*, 1993. 34(24): 5085-5092.
78. Hasan O.A. and Boyce M.C., A constitutive model for the nonlinear viscoelastic viscoplastic behavior of glassy-polymers. *Polymer Engineering and Science*, 1995. 35(4): 331-344.
79. Boyce M.C., Arruda E.M., and Jayachandran R., The large-strain compression, tension, and simple shear of polycarbonate. *Polymer Engineering and Science*, 1994. 34(9): 716-725.
80. Boyce M.C., Socrate S., and Llana P.G., Constitutive model for the finite deformation stress-strain behavior of poly(ethylene terephthalate) above the glass transition. *Polymer*, 2000. 41(6): 2183-2201.
81. van Dommelen J.A.W., et al., Micromechanical modeling of the elasto-viscoplastic behavior of semi-crystalline polymers. *Journal of the Mechanics and Physics of Solids*, 2003. 51(3): 519-541.
82. Qi H.J. and Boyce M.C., Stress-strain behavior of thermoplastic polyurethanes. *Mechanics of Materials*, 2005. 37(8): 817-839.
83. Boyce M.C., Parks D.M., and Argon A.S., Large inelastic deformation of glassy-polymers. 1. Rate dependent constitutive model. *Mechanics of Materials*, 1988. 7(1): 15-33.
84. Arruda E.M., Boyce M.C., and Jayachandran R., Effects of strain-rate, temperature and thermomechanical coupling on the finite strain deformation of glassy-polymers. *Mechanics of Materials*, 1995. 19(2-3): 193-212.
85. Mulliken A.D. and Boyce M.C., Mechanics of the rate-dependent elastic-plastic deformation of glassy polymers from low to high strain rates. *International Journal of Solids and Structures*, 2006. 43(5): 1331-1356.

86. Boyce M.C. and Arruda E.M., An experimental and analytical investigation of the large strain compressive and tensile response of glassy-polymers. *Polymer Engineering and Science*, 1990. 30(20): 1288-1298.
87. Arruda E.M. and Boyce M.C., Evolution of plastic anisotropy in amorphous polymers during finite straining. *International Journal of Plasticity*, 1993. 9(6): 697-720.
88. Rodriguez E.D., Luo X.F., and Mather P.T., Linear/Network Poly(epsilon-caprolactone) Blends Exhibiting Shape Memory Assisted Self-Healing (SMASH). *ACS Applied Materials & Interfaces*, 2011. 3(2): 152-161.
89. Tobushi H., et al., The influence of shape-holding conditions on shape recovery of polyurethane-shape memory polymer foams. *Smart Materials & Structures*, 2004. 13(4): 881-887.
90. Hu J.L., Ji F.L., and Wong Y.W., Dependency of the shape memory properties of a polyurethane upon thermomechanical cyclic conditions. *Polymer International*, 2005. 54(3): 600-605.
91. Gall K., et al., Thermomechanics of the shape memory effect in polymers for biomedical applications. *Journal of Biomedical Materials Research Part A*, 2005. 73A(3): 339-348.
92. Stachurski Z.H., Deformation mechanisms and yield strength in amorphous polymers. *Progress in Polymer Science*, 1997. 22(3): 407-474.
93. Beloshenko V.A., Varyukhin V.N., and Voznyak Y.V., The shape memory effect in polymers. *Russian Chemical Reviews*, 2005. 74(3): 265-283.
94. Khan F., et al., Characterization of shear deformation and strain recovery behavior in shape memory polymers. *Polymer Testing*, 2008. 27(4): 498-503.
95. Small W., et al., Laser-activated shape memory polymer microactuator for thrombus removal following ischemic stroke: Preliminary in vitro analysis. *Ieee Journal of Selected Topics in Quantum Electronics*, 2005. 11(4): 892-901.
96. Small W., et al., Laser-activated shape memory polymer intravascular thrombectomy device. *Optics Express*, 2005. 13(20): 8204-8213.
97. Sun L., et al., Optimization of the shape memory effect in shape memory polymers. *Journal of Polymer Science Part A: Polymer Chemistry*, 2011. 49(16): 3574-3581.
98. Huang W.M., Shape memory alloys and their application to actuators for deployable structures, in *Cambridge University*. 1998, Cambridge University.
99. Tobushi H., et al., Thermomechanical properties in a thin film of shape memory polymer of polyurethane series. *Smart Materials & Structures*, 1996. 5(4): 483-491.

100. Huang W.M., et al., Shape memory materials. *Materials Today*, 2010. 13(7-8): 54-61.
101. Huang W.M., et al., Thermo-moisture responsive polyurethane shape-memory polymer and composites: a review. *Journal of Materials Chemistry*, 2010. 20(17): 3367-3381.
102. Du H.Y., et al., Microwave-Induced Shape-Memory Effect of Chemically Crosslinked Moist Poly(vinyl alcohol) Networks. *Macromolecular Chemistry and Physics*, 2011. 212(14): 1460-1468.
103. Voit W., Ware T., and Gall K., Radiation crosslinked shape-memory polymers. *Polymer*, 2010. 51(15): 3551-3559.
104. Leng J., et al., Electroactive thermoset shape memory polymer nanocomposite filled with nanocarbon powders. *Smart Materials and Structures*, 2009. 18(7): 074003.
105. Leng J.S., et al., Electrical conductivity of thermoresponsive shape-memory polymer with embedded micron sized Ni powder chains. *Applied Physics Letters*, 2008. 92(1).
106. Yang B., Influence of moisture in polyurethane shape memory polymers and their electrical conductive composites, in *Nanyang Technological University*. 2007, Nanyang Technological University: Singapore.
107. Yang B., et al., Effects of moisture on the glass transition temperature of polyurethane shape memory polymer filled with nano-carbon powder. *European Polymer Journal*, 2005. 41(5): 1123-1128.
108. Yang B., et al., On the enects of moisture in a polyurethane shape memory polymer. *Smart Materials & Structures*, 2004. 13(1): 191-195.
109. Yang B., et al., Effects of moisture on the thermomechanical properties of a polyurethane shape memory polymer. *Polymer*, 2006. 47(4): 1348-1356.
110. Du H.Y. and Zhang J.H., Solvent induced shape recovery of shape memory polymer based on chemically cross-linked poly(vinyl alcohol). *Soft Matter*, 2010. 6(14): 3370-3376.
111. Lendlein A., et al., Light-induced shape-memory polymers. *Nature*, 2005. 434(7035): 879-882.
112. Lendlein A. and Kelch S., Shape-memory polymers. *Angewandte Chemie-International Edition*, 2002. 41(12): 2034-2057.
113. Bellin I., et al., Polymeric triple-shape materials. *Proceedings of the National Academy of Sciences of the United States of America*, 2006. 103(48): 18043-18047.

114. Bellin I., Kelch S., and Lendlein A., Dual-shape properties of triple-shape polymer networks with crystallizable network segments and grafted side chains. *Journal of Materials Chemistry*, 2007. 17(28): 2885-2891.
115. Xie T., Xiao X.C., and Cheng Y.T., Revealing triple-shape memory effect by polymer bilayers. *Macromolecular Rapid Communications*, 2009. 30(21): 1823-1827.
116. Boyd J.G. and Lagoudas D.C., A thermodynamical constitute model for shape memory materials .1. The monolithic shape memory alloy. *International Journal of Plasticity*, 1996. 12(6): 805-842.
117. Fu Y.Q., et al., TiNi-based thin films in MEMS applications: a review. *Sensors and Actuators a-Physical*, 2004. 112(2-3): 395-408.
118. O'Handley R.C., Model for strain and magnetization in magnetic shape-memory alloys. *Journal of Applied Physics*, 1998. 83(6): 3263-3270.
119. Sun Q.P. and Hwang K.C., Micromechanics modeling for the constitutive behavior of polycrystalline shape memory alloys. 1. Derivation of general relations. *Journal of the Mechanics and Physics of Solids*, 1993. 41(1): 1-17.
120. Khonakdar H.A., et al., Investigation and modeling of temperature dependence recovery behavior of shape-memory crosslinked polyethylene. *Macromolecular Theory and Simulations*, 2007. 16(1): 43-52.
121. Long K.N., et al., Photo-induced deformation of active polymer films: Single spot irradiation. *International Journal of Solids and Structures*, 2011. 48(14-15): 2089-2101.
122. Long K.N., et al., Photomechanics of light-activated polymers. *Journal of the Mechanics and Physics of Solids*, 2009. 57(7): 1103-1121.
123. Tobushi H., et al., Thermomechanical properties of shape memory polymers of polyurethane series and their applications. *Journal De Physique Iv*, 1996. 6(C1): 377-384.
124. Buckley C.P., Prisacariu C., and Caraculacu A., Novel triol-crosslinked polyurethanes and their thermorheological characterization as shape-memory materials. *Polymer*, 2007. 48(5): 1388-1396.
125. Chaterji S., Kwon I.K., and Park K., Smart polymeric gels: Redefining the limits of biomedical devices. *Progress in Polymer Science*, 2007. 32(8-9): 1083-1122.
126. Ding X.M., et al., Morphology and water vapor permeability of temperature-sensitive polyurethanes. *Journal of Applied Polymer Science*, 2008. 107(6): 4061-4069.

127. Lendlein A. and Kelch S., Shape-memory polymers as stimuli-sensitive implant materials. *Clinical Hemorheology and Microcirculation*, 2005. 32(2): 105-116.
128. Lendlein A. and Langer R., Biodegradable, elastic shape-memory polymers for potential biomedical applications. *Science*, 2002. 296(5573): 1673-1676.
129. Thomas S.M. and Lendlein A., Solving a knotty problem - surgical sutures from shape memory polymers. *Materials World*, 2002. 10(7): 29-32.
130. Huang W.M., et al., Water-responsive programmable shape memory polymer devices - art. no. 64231S, in *International Conference on Smart Materials and Nanotechnology in Engineering, Pts 1-3*, S. Du, J. Leng, and A.K. Asundi, Editors. 2007. p. S4231-S4231.
131. O'Brien B. and Carroll W., The evolution of cardiovascular stent materials and surfaces in response to clinical drivers: A review. *Acta Biomaterialia*, 2009. 5(4): 945-958.
132. Kelch S., et al., Shape-memory polymer networks from oligo[(epsilon-hydroxycaproate)-co-glycolate]dimethacrylates and butyl acrylate with adjustable hydrolytic degradation rate. *Biomacromolecules*, 2007. 8(3): 1018-1027.
133. Knight P.T., et al., PLGA-POSS End-Linked Networks with Tailored Degradation and Shape Memory Behavior. *Macromolecules*, 2009. 42(17): 6596-6605.
134. Huang W.M., Yang B., and Fu Y.Q., Polyurethane shape memory polymers. 2011, USA: CRC Press.
135. Rivkin I., et al., Paclitaxel-clusters coated with hyaluronan as selective tumor-targeted nanovectors. *Biomaterials*, 2010. 31(27): 7106-7114.
136. Fernandes R. and Gracias D.H., Toward a miniaturized mechanical surgeon. *Materials Today*, 2009. 12(10): 14-20.
137. Huang W.M., Thermo-moisture responsive polyurethane shape memory polymer for biomedical devices. *The Open Medical devices Journal*, 2010. 2: 11-19.
138. Liu Y., et al., Self-folding of polymer sheets using local light absorption. *Soft Matter*, 2012. 8(6): 1764-1769.
139. Carrell J., et al., Shape memory polymer snap-fits for active disassembly. *Journal of Cleaner Production*, 2011. 19(17-18): 2066-2074.
140. Chiodo J.D., et al., Active Disassembly using Shape Memory Polymers for the mobile phone industry, in *Proceedings of the 1999 IEEE International Symposium on Electronics and the Environment, Isee - 1999*. 1999. p. 151-156.
141. Chiodo J.D., et al., Shape memory alloy actuators for active disassembly using 'smart' materials of consumer electronic products. *Materials & Design*, 2002. 23(5): 471-478.

142. Huang W.M., Novel applications and future of shape memory polymers, in *Shape-Memory Polymers and Multifunctional Composites*, J. Leng and S. Du, Editors. 2010, CRC Press/Taylor and Francis Group, LLC: Boca Raton. p. 333-363.
143. Pretsch T., et al., Switchable information carriers based on shape memory polymer. *Journal of Materials Chemistry*, 2012. 22(16): 7757-7766.
144. Hu J.L. and Chen S.J., A review of actively moving polymers in textile applications. *Journal of Materials Chemistry*, 2010. 20(17): 3346-3355.
145. Hu J.L., et al., A review of stimuli-responsive polymers for smart textile applications. *Smart Materials and Structures*, 2012. 21(5).
146. Wang Y.D., et al., Direct evidence on magnetic-field-induced phase transition in a NiCoMnIn ferromagnetic shape memory alloy under a stress field. *Applied Physics Letters*, 2007. 90(10): 101917.
147. Wei Z.G., Sandstrom R., and Miyazaki S., Shape-memory materials and hybrid composites for smart systems - Part I Shape-memory materials. *Journal of Materials Science*, 1998. 33(15): 3743-3762.
148. Li J.H., et al., Shape-memory effects in polymer networks containing reversibly associating side-groups. *Advanced Materials*, 2007. 19(19): 2851-2855.
149. Kushner A.M., et al., A biomimetic modular polymer with tough and adaptive properties. *Journal of the American Chemical Society*, 2009. 131(25): 8766-8768.
150. Jeffrey G.A., An introduction to hydrogen bonding. Topics in physical chemistry. 1997, New York: Oxford University Press. vii, 303 p.
151. Page K.A., Cable K.M., and Moore R.B., Molecular origins of the thermal transitions and dynamic mechanical relaxations in perfluorosulfonate ionomers. *Macromolecules*, 2005. 38(15): 6472-6484.
152. Li F.K., et al., Shape memory effect of ethylene-vinyl acetate copolymers. *Journal of Applied Polymer Science*, 1999. 71(7): 1063-1070.
153. Hayashi S., Technical report on preliminary investigation of shape memory polymers. 1990: Nagoya research and development center, Mitsubishi Heavy Industries Inc., Japan.
154. Ping P., et al., Poly(epsilon-caprolactone) polyurethane and its shape-memory property. *Biomacromolecules*, 2005. 6(2): 587-592.
155. Kim B.K., Lee S.Y., and Xu M., Polyurethanes having shape memory effects. *Polymer*, 1996. 37(26): 5781-5793.
156. Li F.K., et al., Studies on thermally stimulated shape memory effect of segmented polyurethanes. *Journal of Applied Polymer Science*, 1997. 64(8): 1511-1516.

157. Wang W.S., et al., Polylactide-based polyurethane and its shape-memory behavior. *European Polymer Journal*, 2006. 42(6): 1240-1249.
158. Xu J.W., Shi W.F., and Pang W.M., Synthesis and shape memory effects of Si-O-Si cross-linked hybrid polyurethanes. *Polymer*, 2006. 47(1): 457-465.
159. Hu J., Shape memory polymers and textiles. 2007, Cambridge: Woodhead Publishing Limited.
160. Chung Y.C., Choi J.H., and Chun B.C., Shape-memory effects of polyurethane copolymer cross-linked by dextrin. *Journal of Materials Science*, 2008. 43(18): 6366-6373.
161. Park J.S., et al., Shape memory effects of polyurethane block copolymers cross-linked by celite. *Fibers and Polymers*, 2008. 9(6): 661-666.
162. Jung D.H., Jeong H.M., and Kim B.K., Organic-inorganic chemical hybrids having shape memory effect. *Journal of Materials Chemistry*, 2010. 20(17): 3458-3466.
163. Ding Z., Shape memory hybrids: Mechanism and design for tailored properties, in *Nanyang Technological University*. 2012, Nanyang Technological University: Singapore.
164. Liu N., et al., A generic approach for producing various protrusive shapes on different size using shape-memory polymer. *Smart Materials & Structures*, 2007. 16(6): N47-N50.
165. Liu N., et al., The formation of micro-protrusions atop a thermo-responsive shape memory polymer. *Smart Materials & Structures*, 2008. 17(5): 057001.
166. Liu N., et al., Formation of micro protrusion arrays atop shape memory polymer. *Journal of Micromechanics and Microengineering*, 2008. 18(2): 027001.
167. Quinson R., et al., Yield criteria for amorphous glassy polymers. *Journal of Materials Science*, 1997. 32(5): 1371-1379.
168. Arruda E.M., Boyce M.C., and Quintusbosz H., Effects of initial anisotropy on the finite strain deformation-behavior of glassy-polymers. *International Journal of Plasticity*, 1993. 9(7): 783-811.
169. Arruda E.M. and Boyce M.C., A 3-dimensional constitutive model for the large stretch behavior of rubber elastic-materials. *Journal of the Mechanics and Physics of Solids*, 1993. 41(2): 389-412.
170. Peirce D., Shih C.F., and Needleman A., A tangent modulus method for rate dependent solids. *Computers & Structures*, 1984. 18(5): 875-887.
171. Harmon J.P. and Li J.C.M., Transport of alcohols in deformed PMMA. *Annals of the New York Academy of Sciences*, 1981. 371(OCT): 310-311.

172. Harmon J.P., Lee S., and Li J.C.M., Methanol transport in PMMA - The effect of mechanical deformation. *J. Polym. Sci. Part A Polym. Chem.*, 1987. 25(12): 3215-3229.
173. Yang F.Q., Zhang S.L., and Li J.C.M., Impression recovery of amorphous polymers. *J. Electron. Mater.*, 1997. 26(7): 859-862.
174. Landau L. and Lifshitz E.M., eds. *Theory of elasticity*. 3rd ed. 1986, Pergamon, New York.
175. Hutchinson J.W., Plastic buckling. *Advances in applied mechanics*, 1974. 14: 74.
176. Bowden N., et al., The controlled formation of ordered, sinusoidal structures by plasma oxidation of an elastomeric polymer. *Applied Physics Letters*, 1999. 75(17): 2557-2559.
177. Bowden N., et al., Spontaneous formation of ordered structures in thin films of metals supported on an elastomeric polymer. *Nature*, 1998. 393(6681): 146-149.
178. Cerda E. and Mahadevan L., Geometry and physics of wrinkling. *Physical Review Letters*, 2003. 90(7): 074302.
179. Andrews E.H. and Levy G.M., Solvent stress crazing in PMMA. 1. Geometrical effects. *Polymer*, 1974. 15(9): 599-607.
180. Andrews E.H., Levy G.M., and Willis J., Environmental crazing in a glassy polymer - role of solvent absorption. *Journal of Materials Science*, 1973. 8(7): 1000-1008.
181. Hopfenberg H.B., Nicolais L., and Drioli E., Relaxation controlled (case II) transport of lower alcohols in poly(methyl methacrylate). *Polymer*, 1976. 17(3): 195-198.
182. Hopfenberg H.B. and Hsu K.C., Swelling-controlled, constant rate delivery systems. *Polymer Engineering and Science*, 1978. 18(15): 1186-1191.
183. Kramer E.J. and Bubeck R.A., Growth kinetics of solvent crazes in glassy polymers. *Journal of Polymer Science Part B-Polymer Physics*, 1978. 16(7): 1195-1217.
184. Kramer E.J., Krenz H.G., and Ast D.G., Mechanical-properties of methanol crazes in poly(methyl methacrylate). *Journal of Polymer Science Part B-Polymer Physics*, 1978. 16(2): 349-366.
185. Nicolais L., et al., Diffusion-controlled penetration of polymethyl methacrylate sheets by monohydric normal alcohols. *Journal of Membrane Science*, 1978. 3(2-4): 231-245.
186. Thomas N. and Windle A.H., Transport of methanol in poly(methyl methacrylate). *Polymer*, 1978. 19(3): 255-265.

187. Peterlin A., Diffusion in a network with discontinuous swelling. *Journal of Polymer Science Part B-Polymer Letters*, 1965. 3(12PB): 1083-&.
188. Thomas N.L. and Windle A.H., A theory of case-II diffusion. *Polymer*, 1982. 23(4): 529-542.
189. Thomas N.L. and Windle A.H., A deformation model for case-II diffusion. *Polymer*, 1980. 21(6): 613-619.
190. Ware R.A. and Cohen C., Strain effects in the mass flux of methanol in poly(methyl methacrylate). *Journal of Applied Polymer Science*, 1980. 25(5): 717-729.
191. Zhao Y., et al., Patterning atop shape memory polymers and their characterization, in *EPD Congress 2010*. 2010, TMS2010: Washington, USA. p. 167-174.
192. Zhao Y., Huang W.M., and Fu Y.Q., Formation of micro/nano-scale wrinkling patterns atop shape memory polymers. *Journal of Micromechanics and Microengineering*, 2011. 21(6): 067007.
193. Zhao Y., Huang W.M., and Purnawali H., Three Dimensional Surface Patterning Atop Poly(methyl methacrylate) (PMMA). *App. Mechan. Mater.*, 2012. 161: 292-295.
194. Liu N., Huang W.M., and Phee S.J., A secret garden of micro butterflies: Phenomenon and mechanism. *Surface Review and Letters*, 2007. 14(6): 1187-1190.
195. Groenewold J., Wrinkling of plates coupled with soft elastic media. *Physica A*, 2001. 298(1-2): 32-45.
196. Huang R. and Suo Z., Wrinkling of a compressed elastic film on a viscous layer. *Journal of Applied Physics*, 2002. 91(3): 1135-1142.
197. Chen X. and Hutchinson J.W., A family of herringbone patterns in thin films. *Scripta Materialia*, 2004. 50(6): 797-801.
198. Chan E.P. and Crosby A.J., Fabricating microlens arrays by surface wrinkling. *Advanced Materials*, 2006. 18(24): 3238-3242.
199. Cao G.X., et al., Self-assembled triangular and labyrinth buckling patterns of thin films on spherical substrates. *Phys. Rev. Lett.*, 2008. 100(3): 036102.
200. Volynskii A.L., et al., Mechanical buckling instability of thin coatings deposited on soft polymer substrates. *Journal of Materials Science*, 2000. 35(3): 547-554.
201. Volynskii A.L., et al., Buckling instability of a solid coating under the plane compression of a polymer substrate. *Polymer Science Series A*, 2001. 43(2): 124-128.
202. Allen H.G., Analysis and design of structural sandwich panels. 1969, New York: Pergamon Press.

203. Li B., Huang S.Q., and Feng X.Q., Buckling and postbuckling of a compressed thin film bonded on a soft elastic layer: a three-dimensional analysis. *Archive of Applied Mechanics*, 2010. 80(2): 175-188.
204. Hutchinson J.W. and Neale K.W., eds. *Wrinkling of curved thin sheet metal*. Plastic Instability, ed. J. Salencon. 1985, Presses Ponts et Chausees. 71-78.
205. Vandeparre H., et al., Slippery or sticky boundary conditions: Control of wrinkling in metal-capped thin polymer films by selective adhesion to substrates. *Physical Review Letters*, 2007. 99(18): 188302.
206. Zhao Y., et al., Formation of micro protrusive lens arrays atop poly(methyl methacrylate). *Optics Express*, 2011. 19(27): 26000-26005.
207. Huang W.M., et al., Pile-up and sink-in in micro-indentation of a NiTi shape-memory alloy. *Scripta Materialia*, 2005. 53(9): 1055-1057.
208. Park J., Fujita H., and Kim B., Fabrication of metallic microstructure on curved substrate by optical soft lithography and copper electroplating. *Sensors and Actuators a-Physical*, 2011. 168(1): 105-111.
209. Khan A., et al., Parallel near-field optical micro/nanopatterning on curved surfaces by transported micro-particle lens arrays. *Journal of Physics D-Applied Physics*, 2010. 43(30).
210. Engel L., et al., Freestanding smooth micron-scale polydimethylsiloxane (PDMS) membranes by thermal imprinting. *Journal of Micromechanics and Microengineering*, 2012. 22(4).
211. Knuesel R.J., et al., Self-Assembly and Self-Tiling: Integrating Active Dies Across Length Scales on Flexible Substrates. *Journal of Microelectromechanical Systems*, 2012. 21(1): 85-99.

List of Publications

1. Zhao Y., Huang W. M., Wang C. C., Thermo/chemo-responsive shape memory effect for micro/nano patterning atop polymers, *Nanoscience and Nanotechnology Letters*, 2012, 4 (9): 862-878.
2. Zhao Y., Wang C. C., Huang W. M., Purnawali H., An L., Formation of micro protrusive lens arrays atop poly(methyl methacrylate), *Optics Express*, 2011, 19 (27): 26000-26005
3. Zhao Y., Wang C. C., Huang W. M., Purnawali H., Buckling of poly(methyl methacrylate) in stimulus-responsive shape recovery, *Applied Physics Letters*, 2011, 99: 131911
4. Zhao Y., Huang W. M. and Fu Y. Q., Formation of micro/nano-scale wrinkling patterns atop shape memory polymers, *Journal of Micromechanics and Microengineering*, 2011, 21: 067007
5. Zhao Y., Huang W. M., Purnawali H., Three dimensional surface pattering atop poly(methyl methacrylate) (PMMA), *Applied Mechanics and Materials*, 2012, 161: 292-295
6. Zhao Y, Huang W. M., Micron sized polyurethane shape-memory polymer beads, *Advanced Materials Research*, 2011, 239-242: 2675-2678
7. Zhao Y., Cai M., Huang W. M. and Tong T. H., Patterning atop shape memory polymers and their characterization, EPD Congress 2010, Washington, USA, TMS2010: 167-174
8. Huang W. M., Zhao Y., Wang C. C., Ding Z., Purnawali H., Tang C., Zhang J. L., Thermo/chemo-responsive shape memory effect in polymers: a sketch of working mechanisms, fundamentals and optimization, *Journal of Polymer Research*, 2012, 19: 9952
9. Sun L., Zhao Y., Huang W. M., Purnawali H., Fu Y. Q., Wrinkling atop shape memory materials, *Surface Review and Letters*, 2012, 19 (2): 1250010
10. Wang C. C., Zhao Y., Purnawali H., Huang W. M., Sun L., Chemically induced morphing in polyurethane shape memory polymer micro fibers/springs, *Reactive and Functional Polymers*, 2012, 72: 757-764
11. Sun L., Zhao Y., Huang W. M. and Tong T. H., Formation of combined surface features of protrusion array and wrinkles atop shape-memory polymer, *Surface Review and Letters*, 2009, 16 (6): 929-933

12. Huang, W. M., Zhao, Y., Sun, L., Ei, N. N. and Tong, T. H., Wrinkling atop shape memory polymer with patterned surface, 2nd international conference on smart materials and nanotechnology in engineering, Weihai, P.R. China, *Proc. of SPIE*. 2009, 7493**:** 749337.
13. Huang W. M., Song C. L., Fu Y. Q., Wang C. C., Zhao Y., Purnawali H., Lu H. B., Tang C., Ding Z., Zhang J. L., Shaping tissue with shape memory materials, *Advanced Drug Delivery Reviews*, accepted
14. Sun L., Huang W. M., Ding Z., Zhao Y., Wang C. C., Purnawali H., Tang C., Stimulus-responsive shape memory materials: a review, *Materials and Design*, 2012, 33: 577-640
15. Purnawali H., Xu W. W., Zhao Y., Ding D., Wang C. C., Huang W. M. and Fan H., Poly(methyl methacrylate) (PMMA) for active disassembly, *Smart Materials and Structures*, 2012, 21: 075006
16. Wang C. C., Huang W. M., Ding Z., Zhao Y., Purnawali H., Cooling-/water-responsive shape memory hybrids, *Composites Science and Technology*, 2012, 72: 1178-1182
17. Sun L., Huang W. M., Wang C. C., Zhao Y., Ding Z., Purnawali H., Optimization of the shape memory effect in shape memory polymers, *Journal of Polymer Science Part A: Polymer Chemistry*, 2011, 46 (16): 3582-3587
18. Fan K., Huang W. M., Wang C. C., Ding Z., Zhao Y., Purnawali H., Liew K. C. and Zheng L. X., Water-responsive shape memory hybrid: design concept and demonstration, *eXPRESS Polymer Letters*, 2011, 5 (5): 409-416
19. Huang W. M., Ding Z., Wang C. C., Wei J., Zhao Y. and Purnawali H., Shape memory materials, *Materials Today*, 2010, 13: 54-61
20. Huang W. M., Yang B., Zhao Y. and Ding Z., Thermo-moisture responsive polyurethane shape-memory polymer and composites: a review, *Journal of Materials Chemistry*, 2010, 20: 3367-3381
21. Huang W. M., Fu Y. Q. and Zhao Y., High performance polyurethane shape memory polymer and composites, *RFP-Rubber Fibres Plastics*, 2010, 5 (6): 281-285
22. Huang W. M., Zhao Y. and Fu Y. Q., Polyurethan-Formgedächtnis-polymere, *PU Magazin*, 2010, 11: 704-708
23. 黄为民，傅永庆，赵勇，高性能聚氨酯形状记忆聚合物及其复合材料，*PU 杂志*，2010, (1): 49-54